Diss. ETH No. 24066

In-situ High-Resolution X-ray Spectroscopy of Light Rare-Earth Compounds

A thesis submitted to attain the degree of

DOCTOR OF SCIENCES of ETH ZURICH

(Dr. sc. ETH Zurich)

presented by
Ofer Hirsch
Dipl.-Ing. Materials Science, TU Darmstadt
born on 17.05.1987
citizen of Germany

accepted on the recommendation of
Prof. Dr. Markus Niederberger
Dr. Dorota Koziej
Prof. Dr. Jan-Dierk Grunwaldt
Prof. Dr. Marcin Sikora

Zurich, 2017

Abstract

The rare-earth (RE) materials are relevant for different fields of materials science ranging from superconductors, magnetic materials, catalysts, to gas sensors. The physical and chemical properties result from the unique f-electron configuration in the partially filled $4f$ valence shell. To date the f-states of the trivalent rare-earth ions are thought of as purely localized atomic orbitals, whereas the f-states of the tetravalent configuration show a degree of hybridization and delocalization. Recent experiments question this description and covalent, ionic, and mixed bonding was observed. The nature of the $4f$ states in a RE material and their implication on the bond, the materials properties, and the crystal structure are still unclear and difficult to predict with theoretical approaches.

The latest developments in hard X-ray synchrotron-based spectroscopy, namely high-energy resolution fluorescence detected (HERFD) X-ray absorption spectroscopy (XAS) and resonant inelastic X-ray scattering (RIXS), allow to record spectra with high signal-to-noise ratio, no background scattering, and high-energy resolution. The photon-in/photon-out process probes the $4f$ states through an element selective excitation of a $2p$ core-electron and records the emission due to electronic relaxation of the $3d/4d$ state into the empty $2p$ state. Additionally, the excitation of $2p$ electrons into empty $5d$-states, which constitute the unoccupied density of states, provides information on the formal valence and local coordination.

Within this thesis, the local coordination and f-electron occupancy of La and Pr materials are investigated by means of photon-in/photon-out spectroscopy.

Chapter 1 provides an experimental and theoretical overview on HERFD XAS, RIXS and valence-to-core (vtc) X-ray emission spectroscopy (XES) with a focus on the RE elements.

Chapter 2 highlights the selective interaction of CO_2 with La in $La_2O_2CO_3$ leading to the strong changes in electrical resistance. A combination of *in-situ* HERFD XAS and vtc XES reveals a change in the local La coordination, pointing to an additional oxygen neighbor, which results from bidentate carbonate formation upon CO_2 adsorption.

Chapter 3 focuses on the structural and valence changes in the phase transformation of $Pr(OH)_3$ to Pr_6O_{11}. Here, formation of the n-type semiconductor material Pr_6O_{11} is observed with HERFD XAS. The surprising behavior of the different spectral features during repeated heating show the temperature induced population of delocalized f-states.

Chapter 4 describes the unique behavior of f-electrons of Pr in the solid solution with $La(OH)_3$. The HERFD XAS pre-edge transitions probe the localized $4f$ valence shell, which are used as a fingerprint for the number of f-electrons and thus the valence state. Here, the pre-edge features of low concentrated Pr in $Pr_xLa_{1-x}(OH)_3$

exhibit the shape of a $4f^0$ configuration known for La instead of the expected $4f^2$ Pr configuration. This is the first direct experimental proof of delocalization of f-electrons.

Chapter 5 provides a conclusion and further possible applications of hard X-ray spectroscopy to address open questions related to RE materials.

Chapter 6 is an appendix to this thesis, in which, with the help of extended X-ray absorption fine structure (EXAFS), the local coordination of a Ni dopant in molybdenum dioxide matrix and the formation of cobalt, cobalt oxide, and zinc ferrite nanoparticles is investigated. It underlines efforts that were undertaken during the PhD to perform various kinds of spectroscopic investigations.

Zusammenfassung

Die Materialklasse der Verbindungen mit Seltenen Erden ist relevant für die Materialwissenschaft in Anwendungen wie Supraleiter und magnetische Materialien, als Katalysatoren und als Gassensoren. Die besonderen physikalischen und chemischen Eigenschaften basieren auf der einzigartigen f-Elektronenkonfiguration der teilweise gefüllten $4f$ Valenzschale. Heutzutage wird angenommen, dass die f-Elektronen der dreifach ionisierten Seltenen-Erd Atome vollständig lokalisierte Atomorbitale sind. Dagegen zeigen die vierfach geladenen Ionen einen gewissen Grad an Hybridisierung und Delokalisierung der f-Zustände. Neuere Experimente stellen diese Annahmen in Frage, da kovalente, ionische und gemischte Atombindungen beobachtet wurden. Die genaue Art der $4f$ Zustände in den Seltenen-Erd Verbindungen und ihre Einflüsse auf die Bindungen, die Materialeigenschaften und die Kristallstruktur sind noch nicht untersucht und schwer mit theoretischen Methoden vorherzusagen.

Die jüngsten Entwicklungen der Spektroskopie mit harter Röntgenstrahlung, allen voran die hoch-Energieauflösende Fluoreszenz detektierende (aus dem englischen HERFD) Röntgenabsorptionsspektroskopie (XAS) und die resonante inelastische Röntgenstreuung (RIXS), ermöglichen Spektren mit hohem Signal-Rausch-Verhältnis, ohne Hintergrundstreuung und mit hoher Auflösung zu messen. Dieser Photon-in/Photon-out Vorgang probt die $4f$ Zustände direkt durch eine elementspezifische Anregung von einem $2p$ Kernelektron und misst die Emission von einem $3d/4d$ in den leeren $2p$ Zustand. Zusätzlich erlaubt die Anregung der $2p$ Elektronen in leere $5d$ Zustände, welche die unbesetzte Zustandsdichte ausmachen, Informationen über die Oxidationszahl und örtliche Koordination des Absorberatoms zu erlangen.

Kapitel 1 gibt eine Übersicht zu HERFD XAS, RIXS und valence-to-core (vtc) Röntgenemissionsspektroskopie (XES) an Seltenen Erden mit experimentellem und theoretischem Schwerpunkt.

Kapitel 2 behandelt die selektive Wechselwirkung zwischen CO_2 und La in $La_2O_2CO_3$, welches als chemoresistiver Gassensor für Kohlendioxid benutzt wird. Die Kombination von *in-situ* HERFD XAS und vtc XES zeigt eine Änderungen in der lokalen La Koordination. Dies lässt auf einen zusätzlichen Sauerstoffnachbarn schliessen, welcher auf eine Karbonatgruppe in Bidentatform zurückgeführt werden kann.

In Kapitel 3 liegt der Schwerpunkt auf Änderungen in der Struktur und Valenz während der Phasenänderung von $Pr(OH)_3$ zu Pr_6O_{11}. Mit HERFD XAS wird die Bildung von Pr_6O_{11}, einem n-dotiertem Halbleiter, verfolgt. Die besonderen Merkmale in den Spektren zeigen überraschende Besonderheiten beim mehrmaligen Heizen der Proben auf. Dieses Verhalten beruht auf der höheren Besetzung von delokalisierten f Zuständen bei erhöhten Temperaturen. Elektrische Wider-

standsmessungen unterstützen diese Interpretation.

Kapitel 4 behandelt die Hybridisierung von Pr f-Elektronen in der Festkörpermischung mit $La(OH)_3$. HERFD XAS probt am Pre-Peak des Absorptionsspektrums die lokalisierten f-Zustände, welche sich auch die Oxidationszahl des Absorberatoms widerspiegeln. Im Mischkristall $Pr_xLa_{1-x}(OH)_3$ mit geringer Pr Konzentration, nimmt der Pr Pre-Peak die Form eines $4f^0$ Zustandes ein, der typisch für La ist. Dies ist die erste experimentelle Beobachtung von Hybridisierung von f-Zuständen.

Kapitel 5 gibt eine Zusammenfassung und zeigt weitere offene Fragen in Seltenen-Erd Verbindungen, die mit HERFD XAS beantwortet werden können.

Kapitel 6 kann als Anhang zu dieser Arbeit verstanden werden. Mit EXAFS (aus dem Englischen: extended X-ray absorption fine structure) wird die direkte Nachbarschaft von einem Ni Dotieratom in MoO_2 und die Bildung von Kobalt, Kobaltoxid und Zinkferrit Nanopartikeln untersucht. Es unterstreicht Bestrebungen über verschiedene spektroskopische Untersuchungen, welche im Rahmen des Doktorats durchgeführt wurden.

Contents

1 Introduction

Materials containing rare-earth (RE) elements are recently of bigger interest due to their applications in electromechanical materials, [1] in superconductors, [2] in magnetic materials, [3] multiferroics, [4] and as catalyst. [5–7] The physical and chemical properties are related to the partially filled $4f$ shell of the RE ions. In the oxide form, most of the RE atoms are purely trivalent and the f-electrons are assumed to be of pure atomic character with a strong localization on the atom itself. [8] Thus, they do not participate in the bond formation. Cerium, praseodymium, and terbium are the exemption and they can form a tetravalent ion, most noticeably in the oxides. Ce forms under ambient conditions CeO_2 with Ce^{4+} ions, Pr and Tb mixed valent materials, Pr_6O_{11} and Tb_4O_7. The f-shell of the tetravalent ions shows an ability to hybridize with the orbitals of the oxygen ligand, resulting in a delocalization and non-integer value of the f-electron occupancy. [8, 9]

X-ray absorption spectroscopy (XAS) is an ideal tool to directly and selectively probe the f-states of the rare-earth ions. Generally, an incident X-ray photon excites a core-electron into an empty state. Utilizing X-rays in the energy range of 0.1 keV to 1.5 keV, a $3d$ or $4d$ electron gets excited into empty $4f$ states. [10–13] The latest developments in hard X-ray absorption spectroscopy lead to opportunities of probing the $4f$-states with incident photon energies larger than 4.5 keV. [14] The incident photons excite a deep core-hole such as the $2p$ state into the empty $4f$ state via a quadrupole transition. The subsequent fluorescence decay of a $3d$ or $4d$ state into the $2p$ core-hole is recorded as a function of incident energy in high-energy resolution fluorescence detected (HERFD) XAS. A detailed description of this photon-in/photon-out process is given in section 1.1.

The localized f-states of different RE materials, such CeO_2, $Ce_2(CO)_3$, and Yb_2O_3, were probed and evaluated with HERFD XAS and resonant inelastic X-ray scattering (RIXS). [15] The recorded features can be directly related to the number of localized f-electrons and used equivalently to the main edge as a determination of the formal valence. CeO_2 is the most studied RE oxide of the lanthanide series due to its ability to reversibly store and release oxygen and catalytic activitiy. [16, 17] The Ce ions occur in the tri- and tetravalent state resulting in an oxygen release or uptake. Exposing CeO_2 nanoparticles of different shapes to CO and O_2 reduces and oxidizes the Ce sites in the material. [6] Clear indications of a localized $4f$-state were found with HERFD XAS and related to surface and surface-near Ce^{3+}. A similar behavior is reported for ceria thin films. [18] Contradicting results were observed in the *in-situ* investigation of the catalytic activity of CeO_2 nanoparticles towards H_2O_2. [5] The changes in the spectral features were not caused by reduction of Ce^{4+} to Ce^{3+} and thus a change in the f-electron configuration from $4f^0$ to $4f^1$, but rather the average f-electron occupancy changed during the catalytic

reactions. The f-electrons are delocalized in a Ce $4f$-O $2p$ band and the occupancy of this band is the determining factor for catalytic activity. The high resolution of the spectral features also allows for a nanoparticle size determination. [7] HERFD XAS of differently sized ceria nanoparticles was measured. The larger surface-to-volume ratio of the small nanoparticles changes the local coordination and allows for a distinction between the small and large nanoparticles.

HERFD XAS studies on Pr are scarce. [2, 19] It occurs, like Ce, in the tri- and tetravalent configuration with one $4f$ electron more than the corresponding Ce ion. The stable Pr oxide is of mixed valence and exhibits good electrical conductivity at room temperature. La on the other hand, is always trivalent and thus a good material to study effects on the local coordination. Therefore, the high-resolution X-ray spectroscopy of La and Pr materials is the focal point of this thesis.

1.1 Hard X-ray spectroscopy

To study the electronic structure of materials, X-rays with high intensity, flux, and incident photon energies in the range of 4.5 keV to 25 keV are needed. Current synchrotron sources fullfill these requirements and provide X-rays with a flux of up to 10^{13} photons/s. The incident photon energy is selected with a double crystal monochromator with a broadening of 1 eV.

The following sections describe fundamentals of hard X-ray photon-in/photon-out spectroscopy of rare-earth materials.

In the last years several reviews and books were written about the experimental setups, the information that can be obtained with such experiments and the theoretical background with options to evaluate the recorded spectra. [20–27]

1.1.1 X-ray Absorption Spectroscopy (XAS)

X-ray absorption spectroscopy utilizes the interaction between X-ray photons and matter in the hard X-ray regime ($E \geq 4.5$ keV). The energy of the incoming photon is of the same order of magnitude as the binding energies of core-electrons. As a result, the incident photons excite element selective core-electrons into empty states. Recording this absorption process as a function of incident photon energy provides information about the oxidation state and the direct neighborhood of the absorbing atom. The subsequent relaxation of a core-hole emits a X-ray photon, which is recorded in the fluorescence detected spectroscopy. Even though absorption and fluorescence spectra result from different processes, they give access to similar information.

Fig. 1.1 shows a typical XAS measurement in total fluorescence yield (TFY) mode (red line) and HERFD XAS mode (black line, see section 1.1.3). The spectrum shows two regions, the pre-edge (gray) and the edge and post-edge (white). The edge, also called white line, is the minimum energy to excite a core-electron into empty states. In the case of the RE L_3 edge this corresponds to a $2p$ electron excitation in empty $5d$ states. The pre-edge region gives information about the local symmetry and, in

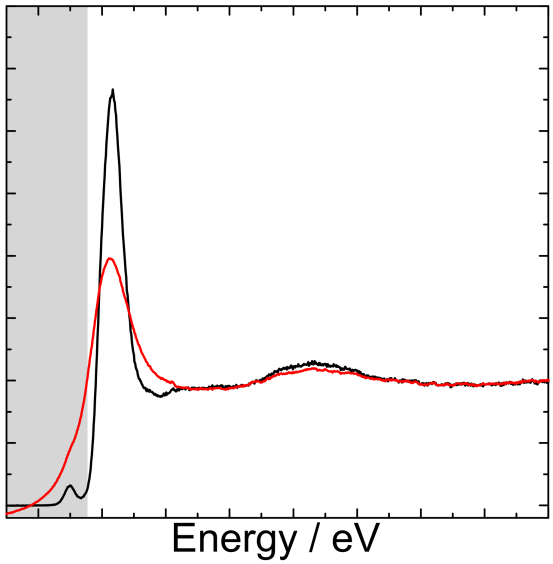

Figure 1.1: A typical HERFD XAS spectra on the La edge shown in black and the total fluorescence yield shown in red. The gray region describes the pre-edge region, whereas the white part shows the white line and post edge region. The local symmetry and the f-electrons determine the pre-edge shape and intensity. The formal valence of the absorbing ion shifts the white line. The neighboring atoms shape the post-edge region. The increased resolution of HERFD XAS is able to resolve the pre-edge region and provide a better description of the white line.

the RE ions, about the f-electron state. The position of the white line corresponds to formal valence and the post edge region allows to draw conclusions about to the coordination and type of the neighboring atoms.

1.1.2 Total Energy Diagram

The total energy diagram in Fig. 1.2 illustrates the process of photon-in/photon-out spectroscopy such as fluorescence detected absorption spectroscopy for the RE atoms. [20, 21, 24] The incoming photon Ω excites at the L_3-edge a $2p$ electron into the empty states of the $5d$ band or, in case of the pre-edge, into localized $4f$ states. The resolution of this absorption process is defined by the $2p$ core-hole lifetime broadening which is in the range of 3 eV to 7 eV. [28] Measuring a final state with a smaller core-hole lifetime broadening enables to resolve the pre-edge and additional main-edge structures. Relaxation of the excited $2p^5 5d^1$ state leads to the emission of an X-ray photon ω. Fig. 1.2 shows the two strongest fluorescence processes for the RE atoms, namely the $L\alpha$ ($3d \rightarrow 2p$) and $L\beta$ ($4d \rightarrow 2p$) process. The final core-hole in the $3d/4d$ orbitals is the resolution determining state and the lifetime broadening is in the range of 1 eV.

The final state in the pre-edge photon-in/photon-out spectroscopy has the same configuration as XAS at the RE M- and N-edges, where the photon energy in the soft X-ray regime is needed. With this two photon process the same final state and

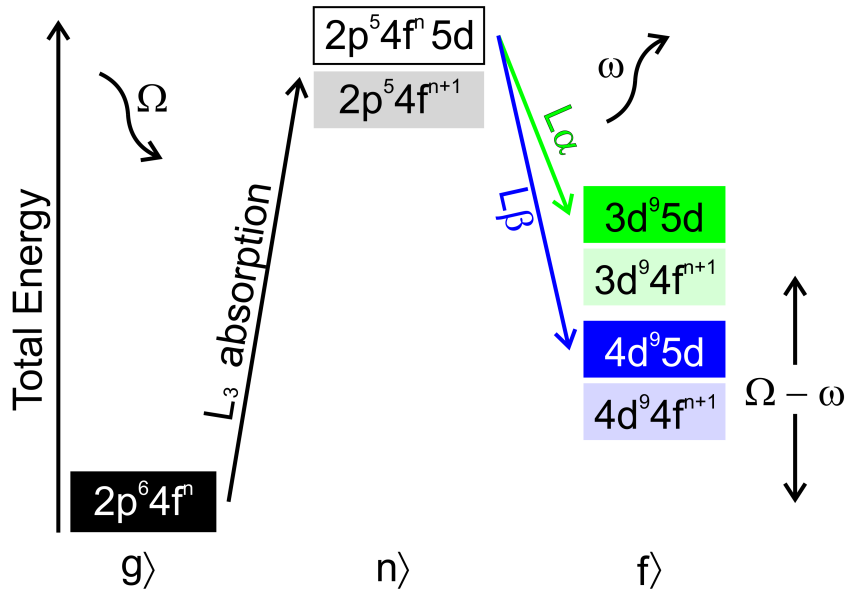

Figure 1.2: Total energy diagram for a rare-earth atom in the HERFD XAS and RIXS process. The incident X-rays, Ω, excite a $2p$ core-electron in the L_3 absorption process from the $2p^6 4f^n$ ground state. The excited intermediate state has a $2p^5 4f^n 5d^1$ state for the main edge and a $2p^5 4f^{n+1}$ configuration at the pre-edge. A $3d \rightarrow 2p$ or $4d \rightarrow 2p$ emission, ω, is recorded in the $L\alpha$ or $L\beta$ line, respectively. The difference between incident and emission photon energy $\Omega - \omega$ equals the energy transfer from the ground to the final state.

thus the same information is reached with hard X-rays. The high penetration depth of those photons allows not only the use different experimental conditions but also ensures that the bulk of the sample is probed and not only the surface.

1.1.3 High-Energy Resolution Fluorescence Detected XAS

The lifetime of the final state core-hole governs the experimental broadening of the measured spectra. In high-energy resolution fluorescence detected XAS a spectrometer setup, shown in Fig. 1.3, allows to choose one specific emission line, such as the RE $L\alpha$ line. The spectrometer consists of several spherically bent crystals and is positioned to selectively choose the emission of one specific fluorescent decay. HERFD XAS is, additionally to the element selective absorption line, element selective in the emission line. The reduced broadening and the double element selectivity makes HERFD XAS an ideal tool for studying the RE materials. This setup resolves not only additional features but also gives the opportunity to measure mixed RE materials, where the absorption and emission energies lie within several 100 eV. In a typical experiment the emission energy is tuned to the maximum of the emission line and the incident energy varies in a range of about 100 eV around the chosen absorption line.

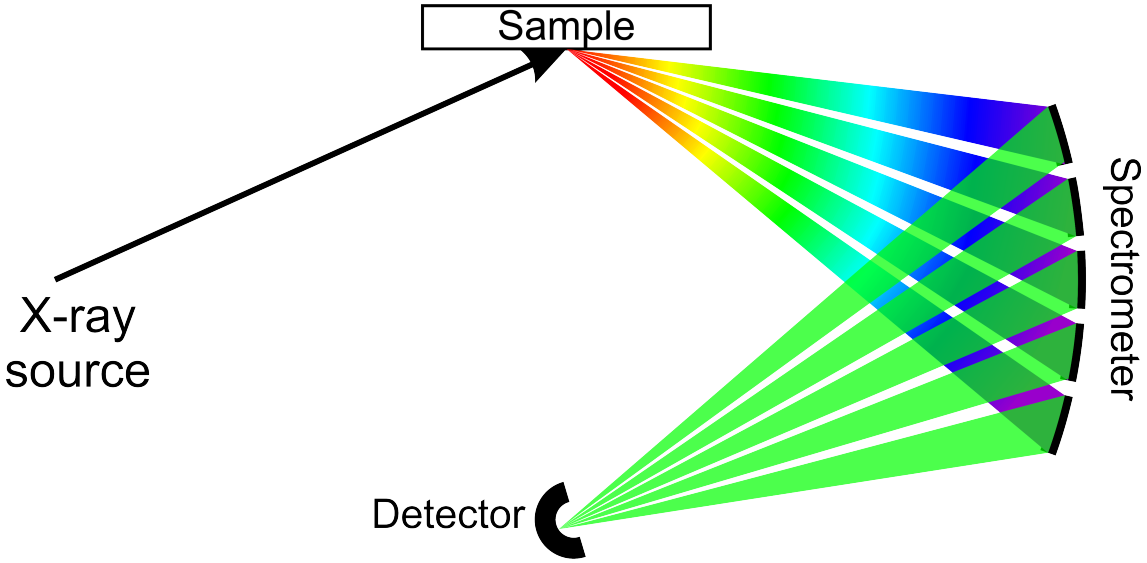

Figure 1.3: Experimental setup for HERFD XAS and valence-to-core XES. The synchrotron X-rays irradiate the sample and upon relaxation of a core-hole the sample emits X-rays with defined energies. The Johann-type spectrometer, [29, 30] consisting of up to five spherically bent Si or Ge crystals, can select one specific emission line, which is recorded with an avalanche photo diode.

The comparison between the total and a selective recorded fluorescence is shown in Fig. 1.1 for a La compound, measured at the La L_3 absorption line. The red line shows the TFY while the black line shows the spectra of the same sample recorded in the HERFD XAS mode, where the spectrometer was tuned to the La $L\alpha$ emission line. The final state core-hole in the TFY spectra is a $2p$ core-hole, which is the intermediate HERFD XAS state (see Fig. 1.2), whereas a $3d$ core-hole is present in the HERFD XAS final state. The final state core-hole lifetime broadening is now reduced from 3.4 eV for the $2p$ state to 0.7 eV of the $3d$ state. [28] The broadening of the incident monochromator and the spectrometer is 1 eV, thus in the same range as the final state core-hole lifetime broadening.

1.1.4 Resonant Inelastic X-ray Scattering

The spectrometer setup from HERFD XAS provides a high freedom in choosing emission lines. Furthermore, it provides the opportunity to measure $2D$ maps of the XAS region by varying the incident (Ω) and emitted (ω) photon energy at the same time. This process is called resonant inelastic X-ray scattering (RIXS). A diagonal cut through the $2D$ RIXS plane results in the HERFD XAS spectrum. The RIXS maps of the pre-edge of transition- and RE-metal ions helped strongly in the theoretical explanation of the observed HERFD XAS spectra. As mentioned in section 1.1.2, the final state of the pre-edge RIXS process is the same as the final state in soft X-ray absorption spectroscopy, where the TM d- and RE f-states are probed. Those states are highly sensitive to the local geometry and formal

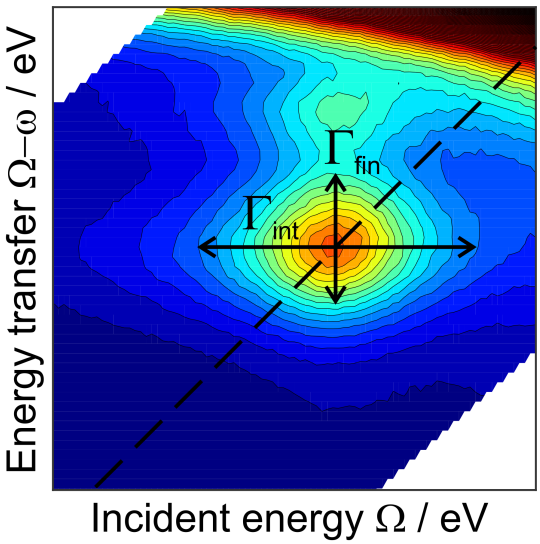

Figure 1.4: A typical pre-edge RIXS measurement on a La compound. The energy transfer, $\Omega - \omega$, is recorded in a pre-defined energy, while the incident energy Ω scans over the pre-edge region. The top-right corner shows the upcoming white line. The diagonal cut through the map, highlighted by the dashed line, results in a HERFD XAS spectrum. Γ_{int} and Γ_{fin} are the lifetime broadening of the intermediate and final state, respectively.

valence. [31, 32] Additionally, those states are responsible for magnetic properties of the materials. [33]

Fig. 1.4 shows a typical pre-edge RIXS map for a La compound. A diagonal cut through this map results in a HERFD XAS spectrum. The incident energy Ω is scanned over the La L_3 absorption line at 5483 eV and the emission energy ω is scanned over the La $L\alpha$ emission line, resulting from a $3d \rightarrow 2p$ transition with an energy of 4647 eV. The energy transfer of 836 eV at the maxima of the absorption and emission line is the exact energy of the La M_5 absorption line. The RIXS maps probe the same final states, $3d^9 4f^1$, with a two photon process, as the M_5 absorption spectroscopy. The horizontal and vertical arrows in Fig. 1.4 show the intermediate and final state core-hole lifetime broadening, respectively. Taking a diagonal cut at the dashed line results in a HERFD XAS scan as shown in Fig. 1.1. Section 1.2 focusses on the theoretical interpretation of HERFD XAS and RIXS spectra.

1.1.5 X-ray Emission Spectroscopy

In HERFD XAS the spectrometer is tuned to the maximum of one specific emission line and the incident energy varies over an absorption line of the specific element, and probes the element projected unoccupied states. Information about the occupied states are obtained by fixing the incident energy to the maximum of the white line and the spectrometer setup records the emission at different energies. This technique is called valence-to-core (vtc) X-ray emission spectroscopy (XES). The

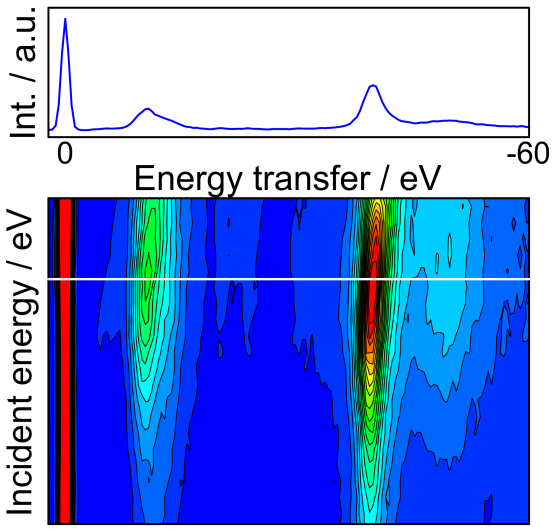

Figure 1.5: Valence-to-core XES of $La(OH)_3$ is shown as a line scan (top) extracted from the full map (bottom) at the horizontal white line. The measured energy transfer is between 0 eV to −60 eV. Thus, the states at the top of the valence band are probed. The feature at 0 eV energy transfer results from direct scattering. The other features are caused by occupied electronic states.

energy transfer is usually in the range of 0 eV to −60 eV. Such a measurement is shown in the top panel of Fig. 1.5. The first feature at 0 eV rises from elastic scattering, in which the incident and emitted photons have the same energy. The other features relate to states at the top of the valence band and thus occupied states. The excitations of those valence band states are dependent of the incident energy as the 2D map in the lower panel of Fig. 1.5 shows.

The combination of HERFD XAS and vtc XES allows to determine the electronic band gap of the investigated materials. [34] The such obtained values are not directly comparable with the band gap measured with UV/VIS spectroscopy. Different selection rules in optical spectroscopy result in differently projected DOS. The differences in momentum between the photon and the electron stimulate direct transitions more than the indirect ones.

Recently, extensive studies on transition metal compounds prove high chemical sensitivity of XES to metal ligands like carbon, oxygen, and nitrogen being not accessible by XAS. [20–22, 31] Such experiments on f-electron systems are scarce and the theoretical description of the partially filled f-shell demanding. [35–38]

1.2 Theoretical description of X-ray spectroscopy

The description of photon-in/photon-out process starts with Fermi's Golden Rule in equation (1.1), [24, 25] which describes the absorption of an incoming photon by the initial state $|g\rangle$ to reach the absorption final state $|n\rangle$ by the transition operator

$\hat{T}$,

$$I_{XAS} \propto |\langle n|\hat{T}|g\rangle|\delta_{E_f - E_i - \hbar\Omega}. \tag{1.1}$$

The δ function ensures the energy conservation of the system. In a second order process such as HERFD XAS the intensity follows the Kramers-Heisenberg formula in equation (1.2):

$$I_{KH} \propto \sum_f \left| \sum_n \frac{\langle f|\hat{D}|n\rangle \langle n|\hat{Q}|g\rangle}{E_n - E_g - \hbar\omega - i\Gamma_n} \right|^2 \cdot \frac{\Gamma_f/\pi}{\left(E_f - E_g - \hbar(\Omega - \omega)\right)^2 + \Gamma_f^2}, \tag{1.2}$$

where $\hat{D}$ and $\hat{Q}$ are the dipole and quadrupole transition operators, respectively, $|g\rangle$, $|n\rangle$, and $|f\rangle$, the ground, intermediate, and final state of the system with the corresponding energies E_g, E_n, and E_f and core-hole lifetime broadening Γ_n and Γ_f. The incident photon has the frequency Ω and the emitted photon ω. Fig. 1.2 describes this process for a RE atom in a L_3 absorption and $L\alpha$ or $L\beta$ emission process.

The pre-edge region of RE-atoms is described by the $2p \rightarrow 4f$ quadrupole transition. The partially filled f-states have a rich structure governed by multiplet effects, which can be accurately calculated with present computer programs. [39–42]

The program calculates within the multiplet formalism the energy of a given configuration by applying the Hamiltonian shown in equation 1.3.

$$\hat{H} = \sum_N \frac{p_i^2}{2m} + \sum_N \frac{-Ze^2}{r_i} + \sum_{pairs} \frac{e^2}{r_{ij}} + \sum_N \zeta(r_i)\, l_i \cdot s_i \tag{1.3}$$

The first and second part of equation (1.3) are the kinetic energy and electrostatic interaction between the electrons and the nucleus and are treated as average energy of an atom in this certain electronic configuration. The third term describes the electron-electron repulsion and the last term the spin-orbit coupling. Additional terms arising from the crystal- or ligand-field have a strong influence on the pre-edge XAS spectral shape in transition metal ions but are negligible in f-electron systems since the crystal field acting on the RE pre-edge is much smaller than the experimental resolution.

With this Hamiltonian the energies of all possible configurations in the $|g\rangle$ and $|n\rangle$-states are calculated. The quadrupole transition operator is applied and the result is a number of allowed final states with defined intensities. Continuing with the dipolar radiative process of a fluorescence the RE pre-edge RIXS maps can be calculated as a function of incident and emitted energy with the Kramers-Heisenberg formalism in equation (1.2). For the RE pre-edges the number of $|g\rangle$ states is dependent of the number of f-electrons, n_f, and is calculated with equation (1.4):

$$n_g = \binom{14}{n_f}, \tag{1.4}$$

in the excited state $|n\rangle$ the number of possible states is $n_n = 6n_g$, and in the final state $|f\rangle$ $n_f = 10n_g$.

On the example of a La^{3+} ion with a $4f^0$ configuration there is one ground state configuration and 84 intermediate state configuration due to the coupling of the $2p^5 4f^1$ states. The final state with $4d^9 4f^1$ has 140 possible states. Even though there is such a high number of possible configurations, there are only three intermediate states allowed by the quadrupole transition operator. This in addition with the dipole operator limits the number of allowed final state configurations. Finally, at the La L_3 absorption and $L\alpha$ emission line, Fig. 1.4, two main features are observed, seperated by $4f - 3d$ interactions in the final state. [15]

This approach works very well for the pre-edge quadrupole transitions of the RE ions. [15] However, the main and post edge region of XAS spectra are dominated by dipole transitions and mulitple scattering and a different theoretical approach is desired. Density functional theory (DFT) codes such as Wien2k, [43, 44] FDMNES, [45, 46] QuantumEspresso, [47–49] and Orca [50, 51] proved their functionalities in describing XAS and XES spectra of transition metal compounds.

A widely applied program package for XAS calculations is the FEFF code, which is based on a single particle approach. [52,53] This program calculates self-consistently the potentials of a given cluster of atoms, which enables a good estimate of the Fermi energy. The implementation of full multiple scattering improves the calculation results. The program determines the DOS of the system and with a implementation of a core-hole relaxation if needed.

Bibliography

[1] Y. Li, O. Kraynis, J. Kas, T.-C. Weng, D. Sokaras, R. Zacharowicz, I. Lubomirsky, and A. I. Frenkel. *AIP Adv.* (2016), **6**, 055320.

[2] H. Yamaoka, H. Oohashi, I. Jarrige, T. Terashima, Y. Zou, H. Mizota, S. Sakakura, T. Tochio, Y. Ito, E. Y. Sherman, and A. Kotani. *Phys. Rev. B* (2008), **77**, 045135.

[3] M. Coey, K. Ackland, M. Venkatesan, and S. Sen. *Nat. Phys.* (2016), **12**, 694 – 699.

[4] M. Fiebig, T. Lottermoser, D. Meier, and M. Trassin. *Nat. Rev. Mater.* (2016), **1**, 16046.

[5] J.-D. Cafun, K. O. Kvashnina, E. Casals, V. F. Puntes, and P. Glatzel. *ACS Nano* (2013), **7**, 10726–10732.

[6] O. V. Safonova, A. A. Guda, C. Paun, N. Smolentsev, P. M. Abdala, G. Smolentsev, M. Nachtegaal, J. Szlachetko, M. A. Soldatov, A. V. Soldatov, and J. A. van Bokhoven. *J. Phys. Chem. C* (2014), **118**, 1974–1982.

[7] C. Paun, O. V. Safonova, J. Szlachetko, P. M. Abdala, M. Nachtegaal, J. Sa, E. Kleymenov, A. Cervellino, F. Krumeich, and J. A. van Bokhoven. *J. Phys. Chem. C* (2012), **116**, 7312–7317.

[8] C. Bonnelle and N. Spector. *Rare-Earths and Actinides in High Energy Spectroscopy.* Progress in Theoretical Chemistry and Physics. Springer Netherlands, Dordrecht, Netherlands (2015).

[9] L. Petit, A. Svane, Z. Szotek, and W. M. Temmerman. *Phys. Rev. B* (2005), **72**, 205118.

[10] R. C. Karnatak, J. M. Esteva, H. Dexpert, M. Gasgnier, P. E. Caro, and L. Albert. *Phys. Rev. B* (1987), **36**, 1745–1749.

[11] B. T. Thole, G. van der Laan, J. C. Fuggle, G. A. Sawatzky, R. C. Karnatak, and J. M. Esteva. *Phys. Rev. B* (1985), **32**, 5107–5118.

[12] S. Tanaka, H. Ogasawara, K. Okada, and A. Kotani. *J. Phys. Soc. Jpn.* (1995), **64**, 2225–2232.

[13] A. Bianconi, A. Kotani, K. Okada, R. Giorgi, A. Gargano, A. Marcelli, and T. Miyahara. *Phys. Rev. B* (1988), **38**, 3433–3437.

[14] K. Hämäläinen, D. P. Siddons, J. B. Hastings, and L. E. Berman. *Phys. Rev. Lett.* (1991), **67**, 2850–2853.

[15] K. O. Kvashnina, S. M. Butorin, and P. Glatzel. *J. Anal. At. Spectrom.* (2011), **26**, 1265–1272.

[16] J. M. Christensen, D. Deiana, J.-D. Grunwaldt, and A. D. Jensen. *Cata. Lett.* (2014), **144**, 1661–1666.

[17] M. J. Beier, T. W. Hansen, and J.-D. Grunwaldt. *J. Catal.* (2009), **266**, 320 – 330.

[18] G. Gasperi, L. Amidani, F. Benedetti, F. Boscherini, P. Glatzel, S. Valeri, and P. Luches. *Phys. Chem. Chem. Phys.* (2016), **18**, 20511–20517.

[19] H. Yamaoka, H. Sugiyama, Y. Kubozono, A. Kotani, R. Nouchi, A. M. Vlaicu, H. Oohashi, T. Tochio, Y. Ito, and H. Yoshikawa. *Phys. Rev. B* (2009), **80**, 205403.

[20] M. Rovezzi and P. Glatzel. *Semicond. Sci. Technol.* (2014), **29**, 023002.

[21] E. Gallo and P. Glatzel. *Adv. Mater.* (2014), **26**, 7730–7746.

[22] M. Bauer. *Phys. Chem. Chem. Phys.* (2014), **16**, 13827–13837.

[23] D. Koziej. *Chem. Mater.* (2016), **28**, 2478–2490.

[24] P. Glatzel and A. Juhin. *X-ray Absorption and Emission Spectroscopy*, pages 89–171. John Wiley & Sons, Ltd (2013).

[25] F. de Groot and A. Kotani. *Core Level Spectroscopy of Solids*. Advances in Condensed Matter Science. CRC Press (2008). doi:10.1201/9781420008425.fmatt.

[26] F. de Groot. *Chem. Rev.* (2001), **101**, 1779–1808.

[27] G. van der Laan. *Hitchhiker's Guide to Multiplet Calculations*, pages 143–199. Springer Berlin Heidelberg (2006).

[28] M. O. Krause and J. H. Oliver. *J. Phys. Chem. Ref. Data* (1979), **8**, 329–338.

[29] H. H. Johann. *Z. Phys.* (1931), **69**, 185–206.

[30] S. Huotari, F. Albergamo, G. Vankó, R. Verbeni, and G. Monaco. *Rev. Sci. Instrum.* (2006), **77**, 053102.

[31] A. Boubnov, H. W. P. Carvalho, D. E. Doronkin, T. Gïter, E. Gallo, A. J. Atkins, C. R. Jacob, and J.-D. Grunwaldt. *J. Am. Chem. Soc.* (2014), **136**, 13006–13015.

[32] P. Glatzel and U. Bergmann. *Coord. Chem. Rev.* (2005), **249**, 65–95.

[33] M. Sikora, A. Juhin, T.-C. Weng, P. Sainctavit, C. Detlefs, F. de Groot, and P. Glatzel. *Phys. Rev. Lett.* (2010), **105**, 037202.

[34] J. Szlachetko, M. Pichler, D. Pergolesi, J. Sa, and T. Lippert. *RSC Adv.* (2014), **4**, 11420–11422.

[35] A. Kotani, K. O. Kvashnina, P. Glatzel, J. C. Parlebas, and G. Schmerber. *Phys. Rev. Lett.* (2012), **108**, 036403.

[36] A. Kotani, K. O. Kvashnina, S. M. Butorin, and P. Glatzel. *Eur. Phys. J. B* (2012), **85**, 1–13.

[37] K. Kvashnina, Y. Kvashnin, and S. Butorin. *J. Electron Spectrosc. Relat. Phenom.* (2014), **194**, 27 – 36.

[38] K. O. Kvashnina, Y. O. Kvashnin, J. R. Vegelius, A. Bosak, P. M. Martin, and S. M. Butorin. *Anal. Chem.* (2015), **87**, 8772 – 8780.

[39] E. Stavitski and F. M. de Groot. *Micron* (2010), **41**, 687 – 694.

[40] H. Ikeno, F. M. F. de Groot, E. Stavitski, and I. Tanaka. *J. Phys.: Condens. Matter* (2009), **21**, 104208.

[41] R. D. Cowan. *The Theory of Atomic Structure and Spectra*. Los Alamos Series in Basic and Applied Sciences. University of California Press, Berkeley, California (1981).

[42] P. H. Butler. *Point Group Symmetry and Applications - Methods and Tables*. Plenum Press, New York (1981).

[43] K. Schwarz and P. Blaha. *Comput. Mater. Sci.* (2003), **28**, 259 – 273.

[44] L. Pardini, V. Bellini, F. Manghi, and C. Ambrosch-Draxl. *Comput. Phys. Commun.* (2012), **183**, 628 – 636.

[45] Y. Joly. *Phys. Rev. B* (2001), **63**, 125120.

[46] O. Bunču and Y. Joly. *J. Phys.: Condens. Matter* (2009), **21**, 345501.

[47] P. Giannozzi, S. Baroni, N. Bonini, M. Calandra, R. Car, C. Cavazzoni, D. Ceresoli, G. L. Chiarotti, M. Cococcioni, I. Dabo, A. D. Corso, S. de Gironcoli, S. Fabris, G. Fratesi, R. Gebauer, U. Gerstmann, C. Gougoussis, A. Kokalj, M. Lazzeri, L. Martin-Samos, N. Marzari, F. Mauri, R. Mazzarello, S. Paolini, A. Pasquarello, L. Paulatto, C. Sbraccia, S. Scandolo, G. Sclauzero, A. P. Seitsonen, A. Smogunov, P. Umari, and R. M. Wentzcovitch. *J. Phys.: Condens. Matter* (2009), **21**, 395502.

[48] C. Gougoussis, M. Calandra, A. P. Seitsonen, and F. Mauri. *Phys. Rev. B* (2009), **80**, 075102.

[49] O. Bunău and M. Calandra. *Phys. Rev. B* (2013), **87**, 205105.

[50] F. Neese. *Wiley Interdiscip. Rev.: Comput. Mol. Sci.* (2012), **2**, 73–78.

[51] S. DeBeer George and F. Neese. *Inorg. Chem.* (2010), **49**, 1849–1853.

[52] J. Rehr and R. Albers. *Rev. Mod. Phys.* (2000), **72**, 621–654.

[53] J. J. Rehr, J. J. Kas, F. D. Vila, M. P. Prange, and K. Jorissen. *Phys. Chem. Chem. Phys.* (2010), **12**, 5503–5513.

2 High-Energy Resolution XAS/XES Reveals Insight into Unique Selectivity of La-based Nanoparticles for CO_2

The content of this chapter was published in the Proceeding of the National Academy of Sciences of the United States of America 2015, 112, 15803 - 15808 by Ofer Hirsch, Kristina O. Kvashnina, Li Luo, Martin J. Süess, Pieter Glatzel, and Dorota Koziej as corresponding author.

2.1 Abstract

The lanthanum-based materials, due to their layered structure and f-electron configuration are relevant for electrochemical application. Particularly, $La_2O_2CO_3$ shows a prominent chemoresistive response to CO_2. However, surprisingly less is known about its atomic and electronic structure, and electrochemically significant sites and therefore, its structure-functions relationships have yet to be established. Here we determine the position of the different constituents within the unit cell of monoclinic $La_2O_2CO_3$ and use this information to interpret *in-situ* high-energy resolution fluorescence detected (HERFD) X-ray adsorption near edge structure (XAS) and valence to core X-ray emission spectroscopy (vtc XES). Compared with $La(OH)_3$ or previously known hexagonal $La_2O_2CO_3$ structures, La in the monoclinic unit cell has much lower number of neighboring oxygen atoms, which is manifested in the whiteline broadening in XAS spectra. Such a superior sensitivity to subtle changes is given by HERFD method, which is essential for *in-situ* studying of the interaction with CO_2. Here, we study $La_2O_2CO_3$-based sensors in real operando conditions, at 250 °C in the presence of oxygen and water vapors. We identify that the distribution of unoccupied La d-states and occupied O p- and La d-states changes during CO_2 chemoresistive sensing of $La_2O_2CO_3$. The correlation between these spectroscopic findings with electrical resistance measurements leads to a more comprehensive understanding of the selective adsorption at La-site and may enable the design of new materials for CO_2 electrochemical applications.

2.2 Introduction

CO_2 became a challenge for our society and we have to develop new materials for its photo/electro-catalysis, chemoresistive sensing and storage. [1–8] Particularly, for the variety of electrochemical applications the selective interaction of CO_2 and charge transfer with solids is in the foreground. At the same time, the interaction of CO_2 with solids in the electrochemical cell or sensing device, are rather complex, thus it remains challenging to experimentally identify the key elements determining their selectivity and efficiency. X-ray absorption (XAS) and X-ray emission (XES) spectroscopies provide complementary information on the electronic structure of materials [9, 10] and on the orbitals participating in the interaction with absorbing molecule. [11] High-energy resolution fluorescence detected (HERFD) XAS probes unoccupied states with a spectral resolution higher than regular XAS. Furthermore, with the same experimental setup XES can be measured, which allows to probe the occupied states within the valence band. [12] *In-situ* HERFD XAS or XES experiments have been previously carried out to study the catalytic reaction at the surface of noble metals, [11, 13–16] zeolites, [17] and metal organic frameworks. [18] Thus far, no such *in-situ* experiments have been performed to directly track the changes of the electronic structure of a solid and its electrochemical activity towards CO_2. The rare-earth-based materials like perovskites and oxycarbonates owing to their unique f-electron configuration of Ln (Ln = rare earth) and layered crystal structure, emerge as the most interesting for future photo- and electro-chemical applications. [3–8] Among rare-earth oxycarbonates, [19, 20] particularly lanthanum strongly responds to CO_2 and shows up to 16-fold conductivity changes, not seen before for any metal oxides. [21] This is very surprising because a direct injection of an electron into CO_2 molecule requires the activation energy of nearly 2 eV. [22] To assess the origins of the unique CO_2 sensitivity of rare-earth oxycarbonate it is essential to *in-situ* study the interplay between the changes of the electronic structure of La-based nanoparticles upon CO_2 adsorption and changes of the macroscopic conductivity of a device.

Here, to elucidate the underlying mechanism we first determine the structure and atomic positions of the lanthanum oxycarbonate. Using HERFD XAS and valence-to-core (vtc) XES results, we gain information about the electronic structure and band gap. Moreover, we combine *in-situ* HERFD XAS and XES measurements with sensing performance tests to obtain the structure-function relationship. Finally, with all the obtained information we discuss a mechanism of CO_2 adsorption on the $La_2O_2CO_3$ surface.

2.3 Results and Discussion

The synthesis and characterization of $La_2O_2CO_3$ nanoparticles is described in the supporting information (SI), section 2.7, Experimental Methods, section Synthesis and characterization including SI Fig. 2.5-2.7. The crystallite size is between 11 nm to 14 nm as shown in the TEM images in Fig. 2.1A-B and in SI Fig. 2.5A. Three

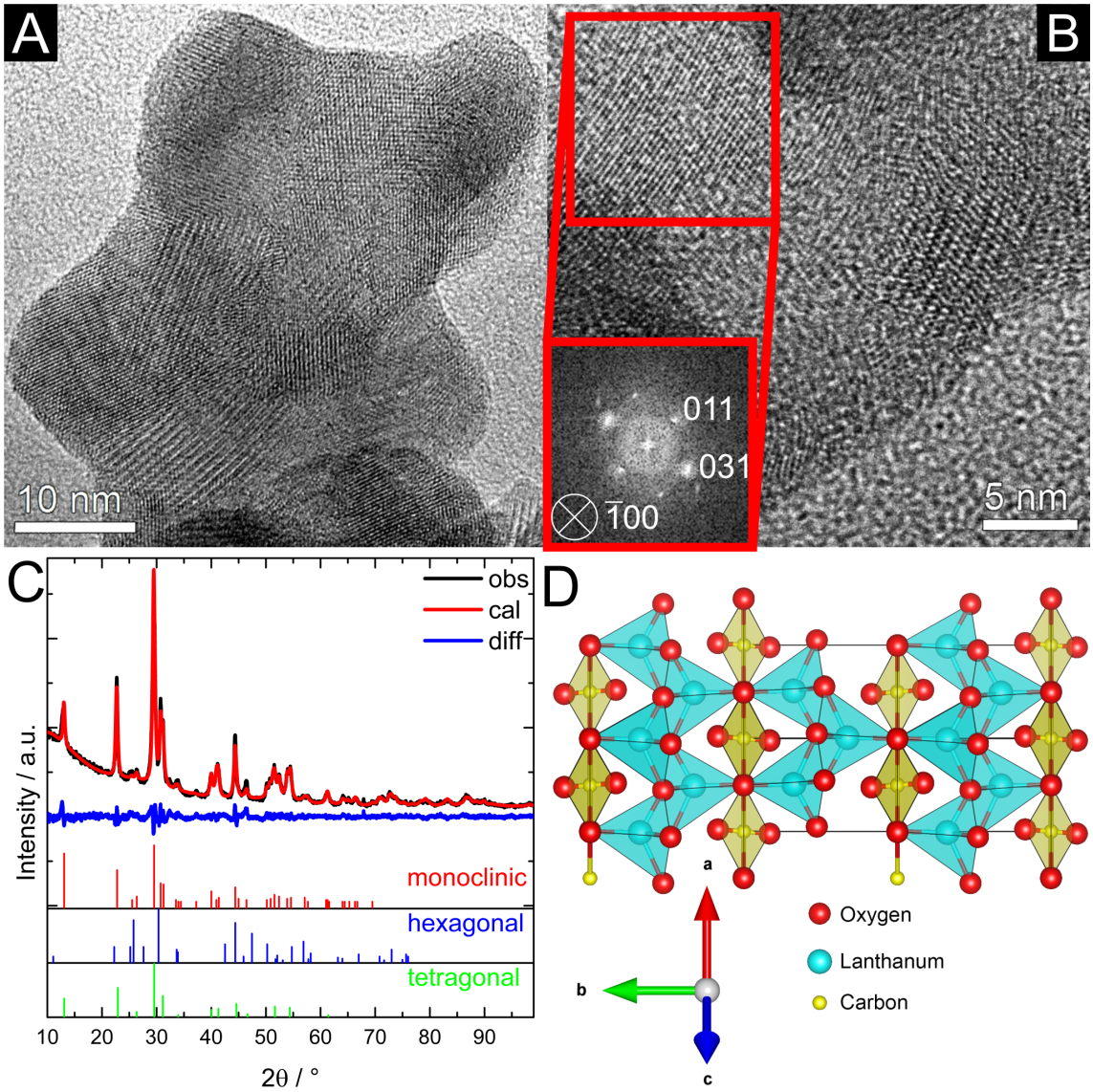

Figure 2.1: Structure and morphology of the $La_2O_2CO_3$ nanoparticles. (A-B) HR-TEM images of $La_2O_2CO_3$ nanoparticles at different magnifications. The inset in (B) Fourier Transform of the region highlighted in red including the zonal axis and indexed reflections. (C) Recorded PXRD pattern of monoclinic $La_2O_2CO_3$ (black line), the calculated (red line), and the difference (blue line) resulting from the Rietveld analysis. Reference patterns of the three polymorphs are shown (monoclinic, hexagonal (ICSD: 37-0804), tetragonal (ICSD: 23-0320)). (D) A model of the refined $La_2O_2CO_3$. The lanthanum atoms are cyan, oxygen red and carbon yellow. The polyhedrons denote the local La surrounded by pyramidal oriented O atoms.

different polymorphs of rare-earth oxycarbonates are known: a tetragonal type I, the monoclinic type Ia and the hexagonal type II. All these types share a layered structure with alternating $Ln_2O_2^{2+}$ and CO_3^{2-} layers. [23, 24] In the hexagonal type this layer consists of distorted LnO_8 coordinated rhombohedra. [19] While the local

coordination around the Ln atom of type II polymorph is known, [25] the atomic positions within the type Ia unit cell are not resolved yet. Here, we assign the PXRD peaks solely to the Ia polymorph of $La_2O_2CO_3$ as shown in Fig. 2.1C. The $La_2O_2CO_3$ nanoparticles crystallize in the space group $P2_1/c$ with the refined lattice parameters a = 4.0756 Å, b = 13.4890 Å, c = 5.8034 Å, $\alpha = \gamma = 90°, \beta = 135.37°$, as deduced from the Rietveld analysis of the PXRD. [26–35] The lattice parameters and the atomic positions of La, C and O in the $La_2O_2CO_3$ lattice and a detailed refinement procedure is given in the SI Experimental Method, section Structure Determination, Table 2.1. The analysis of the atomic positions within the structure helps us to identify local structural commonalities and differences between the monoclinic and the hexagonal polymorph. The $Ln_2O_2^{2+}$ layer in the hexagonal type II consists of distorted LnO_8 coordinated rhombohedra [19] whereas the same layer in the type Ia polymorph contains pyramidal oriented oxygen with a Ln atom in the middle as shown in Fig. 2.1D. The pyramids are pointing in positive or negative b direction and alternate along the c direction (SI Fig. 2.8). Within a distance (R) of 3 Å the lanthanum atom has six oxygen neighbors in type Ia, while La has eight oxygen neighbors in type II. Both crystal structure, and the coordination of the metal cations and the oxygen anions are in general known to have strong impact on the chemical reactivity of rare-earth based nanoparticles. [36] However, reports correlating the structure of $La_2O_2CO_3$ with chemical reactivity are relatively sparse. For example, the crystal structure of intermediate $La_2O_2CO_3$ determines the efficiency of methane reforming to produce hydrogen. [37, 38] Additionally, it was previously shown a $La_2O_2CO_3$-based sensor shows a higher sensor signal than $Nd_2O_2CO_3$. [19, 21] No further information was given about the origin of these differences, but remarkably Nd oxycarbonate crystallizes in the hexagonal type II, whereas La oxycarbonate crystallizes in monoclinic type Ia structure. The formation of $Ln_2O_2CO_3$ from $Ln(OH)_3$ is a sequential process involving compositional and structural modifications. The heating rate, temperature, and CO_2 concentration determine the free energy of transformations and thus the occurrence of the individual polymorphs.

We measured HERFD XAS (Fig. 2.2A) to obtain information about the unoccupied states and valence to core XES to retrieve information about the occupied states (Fig. 2.2B) of $La_2O_2CO_3$. The large life time broadening at the $2p$ level ($\sim$3.4 eV [39]) renders the XAS technique at the La L_3 edge rather insensitive to the electronic structure. Especially, the pre-edge structure of the La L_3 XAS spectrum is very difficult to resolve with conventional XAS experiment. During the HERFD measurements, the X-ray emission spectrometer is tuned to the maximum of the $L\alpha_1$ ($3d_{5/2} - 2p_{3/2}$) transition and the absorption is recorded by monitoring the maximum of the $L\alpha_1$ intensity as a function of the incident energy. The advantage of such a setup is that the width of the spectral features is no longer limited by the $2p_{3/2}$ core hole lifetime but by the sharper $3d_{5/2}$ core hole width in the final state $\sim$0.7 eV, [40] which is on the same order of magnitude as the experimental broadening. To test the sensitivity of the HERFD XAS method for the oxygen coordination of La, we compare the spectrum of lanthanum oxycarbonates (six oxygen neighbors) with lanthanum hydroxide (nine oxygen neighbors) as shown in Fig. 2.2A. The experi-

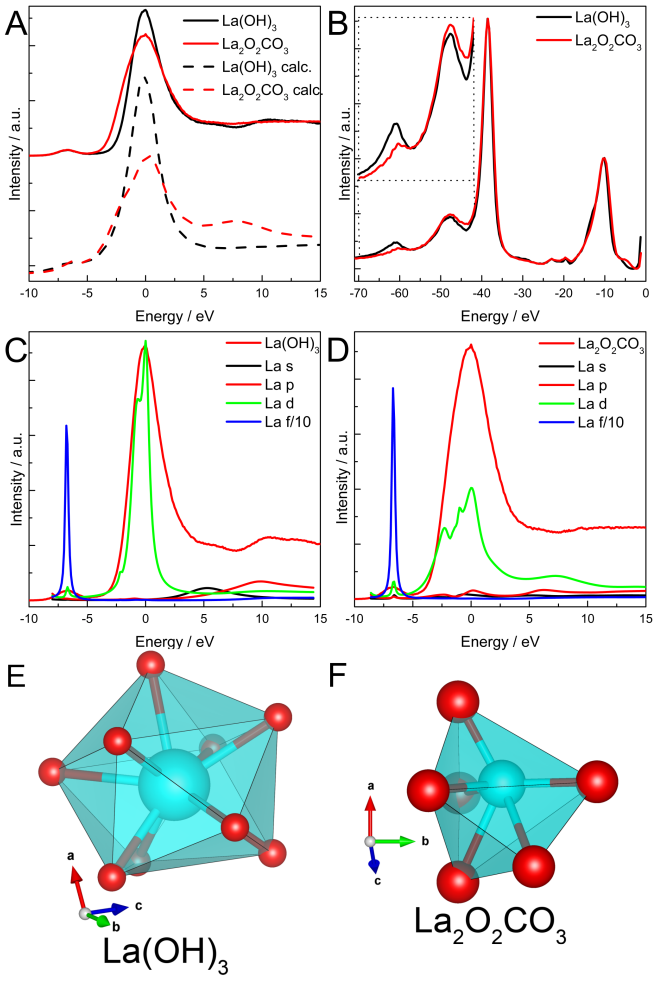

Figure 2.2: *Ex-situ* HERFD XAS and vtc XES experiments along with FEFF calculations and coordination of La-atom for $La(OH)_3$ and $La_2O_2CO_3$. (A) A comparison of the experimental HERFD XAS spectra (solid lines) with the FEFF calculated spectra (dashed lines): $La(OH)_3$ (black) and $La_2O_2CO_3$ (red). (B) Comparison of measured valence-to-core XES spectra of $La(OH)_3$ and $La_2O_2CO_3$. We observe differences at the feature at $-10\,\mathrm{eV}$ and at the features at $-50\,\mathrm{eV}$ and $-60\,\mathrm{eV}$, which are magnified in the inset. We assume the first feature is caused by La *d*- and O *p*-states, the second feature by La *p*- and O *s*-states, and the feature at $-40\,\mathrm{eV}$ by La *s*-states. (C) $La(OH)_3$ and (D) $La_2O_2CO_3$ DOS of the La absorber atom. The width of *d*-DOS width and therefore the whiteline width relates to the amount of oxygen neighbors of the La-atom, which are shown in (E, F) as cluster of LaO_x bonds in lanthanum hydroxide and oxycarbonate. The cutoff length of the sphere around the La atom (R) was set to 3 Å. The lower coordinated La-atom in $La_2O_2CO_3$ exhibits a broader distribution of unoccupied *d*-states than the nine-fold coordinated $La(OH)_3$.

mental data shows the maximum absorption intensity located at the same energy, which corresponds to a La^{3+} ion as it is expected from the stoichiometric formula. There are two important discrepancies between the spectra of these two compounds; $La_2O_2CO_3$ exhibits a wider whiteline, whereas $La(OH)_3$ exhibits a higher whiteline intensity. These observations imply that the charge distribution is more localized around the La ion in the hydroxide than in oxycarbonate, while the formal charge stays three plus. The spectra at energies above the absorption edge reveal more structural features for the hydroxide than for the oxycarbonate. To understand the differences in the experimental data, we calculate XAS spectra with the FEFF program package as shown in Fig. 2.2A, dashed lines. The shape of the whiteline as well as the pre-edge structure are reproduced for both compounds, while the post-edge features are not well modelled in the calculations. Furthermore, the calculation reproduces the differences in the whiteline width and intensity well. The atomic orbital angular momentum projected density of states of both compounds reveal the electronic states that give rise to the pre-edge and the whiteline excitations and are plotted in Fig. 2.2C and 2.2D for $La(OH)_3$ and $La_2O_2CO_3$, respectively. The width of the whiteline and therefore the width of the unoccupied *d*-states reflects the number of oxygen neighbors within the first shell around the La absorber. [41, 42] The higher the coordination number of La, the narrower is the whiteline. Also the crystal structure may induce similar changes of the spectral features. Fig. 2.2E-F shows atoms within a sphere of 3 Å for $La(OH)_3$ and $La_2O_2CO_3$, respectively. We count nine nearest oxygen neighbors for $La(OH)_3$ while La in $La_2O_2CO_3$ has only six nearest oxygen neighbors. Band structure calculations of the electronic states of La_2O_3 with its seven La-O pairs within the sphere of 3 Å show also a wide distribution of empty *d*-states. [43, 44] In the spectra of $La(OH)_3$ and $La_2O_2CO_3$ we observe a pre-edge feature at 6.7 eV below the maximum of the La L_3 absorption edge, which is generally attributed to the mixed dipole and quadrupole transitions. [40, 45, 46] Only systems with inversion symmetry at the absorbing atom can have a pre-edge structure of pure quadrupole contribution but if the inversion symmetry is broken the quadrupole and dipole transitions contribute to the pre-edge intensity. [47] The compounds are not having an inversion center at La atom and thus we observe mixed *d*- and *f*-states in the pre-edge structure. The analysis of the pre-edge DOS reveals a small contribution of dipole transitions of *d*-state character and strong contribution of quadrupole transition of *f*-state character. However, the intensity of quadrupole transitions are considerably smaller than the intensity of dipole transitions, thus the measured pre-edge feature is very small. [45]

To obtain information about the occupied states we perform resonantly excited X-ray emission spectroscopy measurements. We therefore tune the incident photon energy to the maximum of the absorption edge and detect emission spectra with energy differences from 0 eV to −70 eV with respect to the incident energy and probe therefore the highest occupied states. Fig. 2.2B shows the experimental XES spectra of $La(OH)_3$ and $La_2O_2CO_3$. The main features for both compounds are very similar and located at energies at −10 eV and at −40 eV. Interestingly, even at lower transfer energies, 50 eV and 60 eV below the whiteline maximum some features are detectable, which show some small differences in relative intensity between the hy-

droxide and the oxycarbonate. The most pronounced differences are visible in the features, which correspond to the highest occupied levels. Furthermore, the shape of the structure at $-10\,\mathrm{eV}$ also differs. For spectral features at energies close to the Fermi-level at $-10\,\mathrm{eV}$ we assume, based on earlier calculations of $La(OH)_3$ and La_2O_3, a mixing of La *d*-states and O *p*-states. [43,44,48–50] We observe a feature at $-25\,\mathrm{eV}$, which we can assign to a mixing of La *p*- and O *s*-states on the basis of calculations on $La_2Ti_2O_7$. [51] The feature at $-40\,\mathrm{eV}$ was previously observed in X-ray Photoelectron Spectroscopy (XPS) spectra of $La(OH)_3$ and La_2O_3, and was assigned to La $5s$ states. This feature is showing an additional shoulder, which is assigned to a difference in charge transfer from the ligand in $La(OH)_3$ and La_2O_3. In XES spectra of $La(OH)_3$ and $La_2O_2CO_3$ these differences are also clearly visible as shown in the inset of Fig. 2.2B. Within $La(OH)_3$ and $La_2O_2CO_3$ the formal valence of lanthanum ions is La^{3+} and the *d*-states are empty in the ground state. In both cases occupied La *d*-states exist and they form together with O *p*-states the valence band. The La *d*-states are only partly occupied and the empty fraction of the La *d*-states forms the conduction band. The valence and conduction band are separated by an electronic band gap E_g. Combining XAS and XES provides a gap in the *d*-DOS integrated over all directions of momentum transfer and over a range of modulus over momentum transfer that is given by the experimental geometry. [51–53] Here we determine electronic *d*-DOS band gap energies of 5.1 eV and 3.7 eV for $La(OH)_3$ and $La_2O_2CO_3$ nanoparticles, respectively. These values are lower with respect to the optical band gap values derived from UV-VIS spectroscopy with the assumption of an indirect band gap; 5.4 eV to 5.6 eV and 4.35 eV for micrometer large $La(OH)_3$ and $La_2O_2CO_3$ particles, respectively. [54, 55] However, the direct comparison is not straightforward because UV-VIS probes the DOS that is projected according to selection rules for the optical transition. At this wavelength the momentum of a photon is very small compared to the wave vector of the electrons and thus most of the UV-VIS signal arises from direct transitions between valence and conduction band, whereas the indirect transitions are less pronounced.

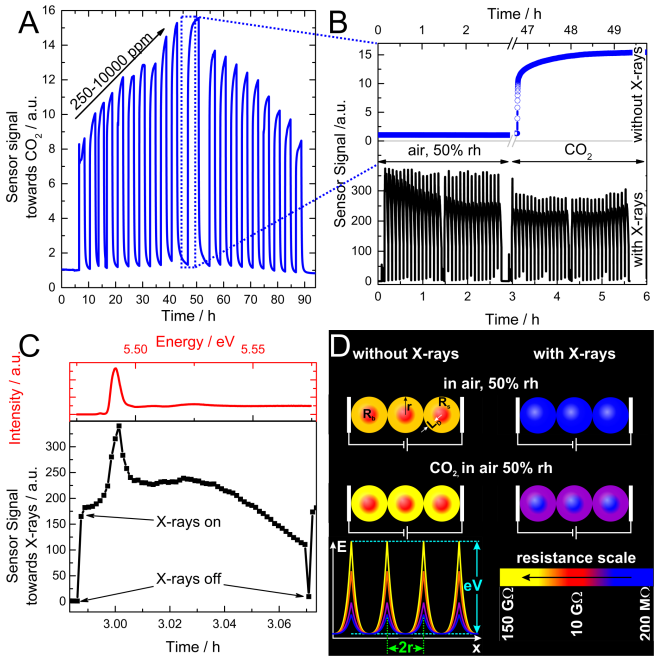

Figure 2.3: An overview on the CO_2 sensing performance of $La_2O_2CO_3$-based sensor with and without X-ray irradiation. (A) Sensing performance upon exposure to CO_2 from 250 ppm to 10 000 ppm in 50 % rh at 250 °C without X-ray irradiation. (B) Comparison of the sensor signal upon exposure to 10 000 ppm of CO_2 without (blue) and with X-rays irradiation (black). The sensor signal is defined as R_{CO_2}/R_{air}, where R_{air} and R_{CO_2} are the resistance of the sensor in air and under CO_2 exposure, respectively. Resistance under X-ray irradiation is energy dependent, thus we use as Rair the initial value before the X-ray irradiation. During 0-3 h under air, we first measure two sets of 15 XANES scans each. Between the individual scans the fast X-rays shutter is closed (X-rays off) and open (X-rays on), which is visible as a spike in the sensor signal. Finally, we measure for 20 minutes only the resistance. We repeat the same data acquisition protocol for the measurements under CO_2. (C). Comparison of the simultaneously recorded XANES spectra (red) and the sensor signal (black) illustrates the dependence of resistance of the sensor on the incident energy. XANES and the sensor signal measurements were measured with different temporal resolution. One measurement point of the sensor signal corresponds to 17 points at the energy scale of XANES scan (1.7 eV). (D) The simplified model for the resistance of the sensor at different experimental conditions shown in (C). We assume that: at 250 °C the Debye length (L_D) is smaller than the radius (r) of $La_2O_2CO_3$ nanoparticles. Gases adsorbing at the surface create a depletion/accumulation layer with the thickness of L_D. The resistance of this layer (R_s) is different than the resistance of bulk of nanoparticles (R_b). The charge carriers have to overcome an energy barrier (eV_s) to reach the neighboring nanoparticle. Dependent on the conditions the height of the barrier is changing as schematically shown; [56] the escape depth of photoelectrons emitted from the absorbing atom is larger than the size of nanoparticles, [57] which means that X-rays equally change the resistance at the surface as well as in the bulk of $La_2O_2CO_3$ nanoparticles. The colors represent the measured resistance.

The chemoresistive sensing principle involves interaction of CO_2 molecules with sensing materials, which then leads to conductivity changes. In real applications, the interaction is not an isolated CO_2 reaction but it is altered by the presence of oxygen and humidity. For example *in-situ* diffuse reflectance infrared Fourier transformed spectroscopy (DRIFTS) studies revealed for $Nd_2O_2CO_3$ – based sensor a correlation between the amount of surface carbonates groups and adsorbed hydroxyl groups; the higher the amount of adsorbed carbonates the lower the amount of water related species on the surface. However, it was suggested that the two gases CO_2 and H_2O do not compete for the same adsorption sites. [19] A similar reaction mechanism has been postulated for $La_2O_2CO_3$-based sensors, but so far the sites for CO_2 adsorption have not been identified. [21] Therefore, we are particularly interested in determining the reaction, which induces the charge transfer between $La_2O_2CO_3$ and CO_2 in humid air, and as a result decreases the overall conductivity of the $La_2O_2CO_3$-based sensor. Before we discuss the *in-situ* spectroscopic data we briefly summarize the sensing characteristic of $La_2O_2CO_3$-based sensors and the impact the incident X-rays thereof. The resistance of the $La_2O_2CO_3$-based sensor decreases, and upon exposure to CO_2 or CO increases as shown in Fig. 2.3A, and SI Fig. 2.9A-B. Moreover, we observe the positive cross-sensitivity to CO_2 and humidity: the baseline resistance of $La_2O_2CO_3$-based sensor at 250 °C is decreasing with increasing humidity and exposure of CO_2 in humid conditions results in higher relative resistance changes than in dry air as shown in SI Fig. 2.9C. We define the sensor signal according to the definition for p-type semiconductors as the resistance of the sensor upon exposure to reducing gas (R_{CO} or R_{CO_2}) over the baseline resistance of the sensor before exposure (R_0). [56]

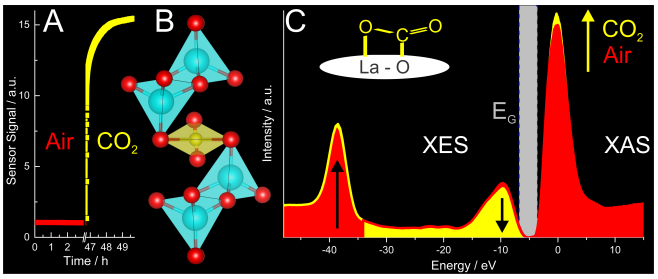

Figure 2.4: *In-situ* studies of structure-functions relationship. (A) The sensor signal upon exposure for 3 h to 10 000 ppm of CO_2. (B) The schematic of unit cell of $La_2O_2CO_3$ illustrating the layered structure and the 6-fold coordination of La-atoms. La, O and C atoms are labeled cyan, red and yellow, respectively. (C) *In-situ* XAS and XES spectra before (red) and after exposure to 10 000 ppm of CO_2 (yellow) in 50 % rh at 250 °C. To underline the changes the area under the experimental curves was colored. We observe a whiteline sharpening, a decrease of the feature at −10 eV and at the same time an increase at the feature at −50 eV. This points at the oxidative character of CO_2 and additional oxygen in the La neighborhood. The inset shows a schematic of possible carbonate species forming at the surface of $La_2O_2CO_3$.

For the *in-situ* XAS and XES experiments we used conditions resulting in the highest sensor signal, which is a pulse of 10 000 ppm of CO_2 in synthetic air with 50 % rh and at operating temperature of 250 °C. The corresponding changes in the sensor signal during *in-situ* HERFD XAS measurements under air and CO_2 pulse are shown in Fig. 2.3B-C. At a given condition two sets of fifteen spectra each were recorded. The labels "X-rays on / off" indicate that the shutter was open or closed, respectively. The incident beam even at energies below the edge causes a rapid decrease of the sensor's resistance of about two orders of magnitude, which results in sensor signal of more than 150 as shown in Fig. 2.3C. During a XAS scan the resistance shows a dependence on the incident X-rays, which indicates that electrons are escaping from the $La_2O_2CO_3$ layer as a result of absorption of an X-ray photon. At an energy corresponding to the maximum of whiteline intensity the sensor signal increases even further to almost 400. The X-ray induced changes of resistance have been previously used to record the Total Electron Yield-XAS (TEY-XAS) spectra. [57] However, for the wide band semiconductors and insulating materials, the charging of the sample has to be experimentally or mathematically compensated by taking into the account the effective penetration depths of secondary electrons as a function of incident X-rays energy, [57–60] and thus we will not discuss it any further. Instead, we analyze the impact of the incident X-rays on the reactivity of $La_2O_2CO_3$ towards CO_2. We observe that between the XAS scans, when the X-ray shutter is shortly closed, the resistance/sensor signal only partially recovers as shown in Fig. 2.3B-C; but if enough time is allowed, it fully recovers to the initial value as shown in SI Fig. 2.10. In summary, the resistance of the sensor increases 16-fold upon exposure to 10 000 ppm of CO_2; the resistance of the sensor decreases almost 400-fold upon irradiation with X-rays and depends on the energy of incident beam as shown in Fig. 2.3B-C. The overall resistance of the sensor exposed to CO_2 under X-ray irradiation is clearly higher than in air as shown in SI Fig. 2.10. The direct quantitative comparison of sensor signal towards CO_2 with and without X ray irradiation is not possible. We assume that the mechanism underlying the chemical reactivity of $La_2O_2CO_3$ towards CO_2 is not affected by incident X-rays, but only the transduction of the chemical reaction into the electrical signal and thus we can qualitatively compare resistivity changes as a function of gas environment under exposure to X-rays. Additionally, the simplified model for the resistance of the sensor at different experimental conditions is given in Fig. 2.3D.

The XAS and XES spectra of films at 250 °C show identical features as spectra of pellets at RT as shown in Fig. 2.2A-B and 4, respectively. Even though the sensor's resistance upon exposure from dry air to 50 % rh decreases 50-fold, the XAS spectra of the sensor measured in dry and 50 % rh air are identical as shown in SI Fig. 2.11A. Thus, we conclude that the La is not an adsorption site for water. Upon exposure to 10 000 ppm of CO_2 in 50 % rh, we notice in the XAS spectra an increase of the intensity and sharpening of the whiteline, whereas other pre- and post-edge features do not change, as shown in SI Fig. 2.11B. These, by analogy to previous HERFD XAS studies [61] point to the oxidative character of CO_2 adsorption on $La_2O_2CO_3$ namely CO_2 molecules are acting as electron acceptors. We ascribe the changes of the whiteline to the presence of additional oxygen in the direct vicinity of La.

The *in-situ* vtc XES measurements further confirm that CO_2 interacts directly with La-sites and the electronic structure is rearranged because of an additional ligand, SI Fig. 2.11C. We observe an increase of the states at $-40\,\text{eV}$ and a decrease of the feature at $-10\,\text{eV}$, which we assume to consist of La *d*- and O *p*-states. We conclude that CO_2 adsorbed at $La_2O_2CO_3$ as surface carbonates as schematically depicted in Fig. 2.4. Remarkably, the XAS studies reveal an oxidative character, whereas the resistance measurements point at reducing character of CO_2 adsorption at $La_2O_2CO_3$ in humid conditions. We note that XAS selectively probes the adsorption at La-site, whereas the resistance of the sensor is not selective to particular reaction or site, but instead probe the net charge transfer between molecules (O_2, CO_2, H_2O) and surface of a solid. [56] This further underlines the advantage of *in-situ* XAS/XES studies for investigating the reactions mechanism in real conditions.

2.4 Conclusion

Here, we present complementary X-ray diffraction, absorption and emission studies of lanthanum oxycarbonate nanoparticles. To calculate the accurate XAS spectra with FEFF code a precise determination of atomic positions is required. Using the PXRD pattern we determine the atomic structure of monoclinic Ia type $La_2O_2CO_3$. Eventually, this information is the foundation for the FEFF calculations, which turn to reproduce very well the measured XAS spectrum. Moreover, we experimentally verify that the La *d*-states are partially occupied and thereof empty fraction forms the conduction band, the occupied fraction forms together with O *p*-states the valence bands, and the electronic *d*-DOS band gap between them is 3.7 eV. To further elucidate the role of the oxycarbonate ligands an advanced DFT calculation of XES spectrum is needed. [12] Herein the combination of HERFD XAS and vtc XES techniques allows us to *in-situ* visualize the charge transfer between relatively inert carbon dioxide and $La_2O_2CO_3$. It reveals changes of both occupied (La *d* and O *p*) and unoccupied states (La *d*) upon the interaction with CO_2; this information is not accessible with other techniques. The CO_2 sensing mechanism in humid air is highly complex; nevertheless, our *in-situ* results show that La is the adsorption site for carbon dioxide but not for water. In the future, the soft–range XAS/XES studies at O and C edges could possibly answer the question concerning sites for water and oxygen adsorption, [62, 63] however such an experiment would be very challenging because both elements are present in $La_2O_2CO_3$ as well as in the ambient atmosphere.

2.5 Experimental Methods

Synthesis. All reagents were used without further purification. $La(OH)_3$ nanoparticles were synthesized in a microwave reactor through heating lanthanum isopropoxide in acetophenone at 200 °C for 20 min. Afterwards the samples were washed and dried in air. $La_2O_2CO_3$ was prepared by heating this sample at 500 °C for two hours

under air.
Structure Determination. The PXRD of Type Ia $La_2O_2CO_3$ was indexed using TREOR implemented in CMPR. [26, 27] The space group was adjusted [35] and the structure solved with the EXPO2013 software. [28] The lattice parameters were refined with GSAS. [29–34]
X-ray spectroscopy. HERFD XAS and vtc XES experiments were carried out at ID26 at the European Synchrotron Radiation Facility (ESRF), which is equipped with an X-ray emission spectrometer. [64,65] For the HERFD XAS experiments the incident energy was scanned over the La L_3 edge and the La $L\alpha_1$ fluorescence line was recorded. In the vtc XES experiments the incident energy was fixed to the maximum of the white line energy and the spectrometer recorded emission just below this incident energy. Powders were pressed in pellets or deposited on the alumina substrate, equipped with Pt electrodes were measured. The sensors were measured under working conditions in humid air at 250 °C with pulses of 10 000 ppm CO_2 in an *in-situ* cell. [16].
FEFF calculations. The spectra were calculated with the FEFF9 program package. [66,67] The calculations for the self-consisting potential were performed including atoms within a sphere of 4 Å. For the full multiple scattering calculations atoms within a sphere of 4 Å and 4.5 Å for $La(OH)_3$ and for $La_2O_2CO_3$, respectively, were included.
Characterization techniques. Phase composition and phase purity were investigated with PXRD on a Panalytical diffractometer and FTIR on a Bruker ATR IR spectrometer. HRTEM micrographs were recorded with a Phillips Tecnai F30 electron microscope.
Detailed information about the synthesis, gas-sensing conditions, the X-ray spectroscopy measurements, the FEFF calculations, and sample characterization techniques are described in SI Experimental Methods.

2.6 Acknowledgements

We thank the ETH Zürich (ETH 2813-1) and the Swiss National Science Foundation (200021_137637 and 200021_1400581) for financial support and the ESRF for the beamtime allocation.

2.7 Supporting Information

Synthesis and characterization
Chemicals. All chemicals were used without further purification. Lanthanum isopropoxide ($La(O^iPr)$) (99 %) was purchased from Strem Chemicals and acetophenone from Fluka Analytical.
Synthesis. The synthesis was prepared in an oxygen and water-free atmosphere in a glovebox (O_2 and $H_2O < 0.1$ ppm). The synthesis of $La(OH)_3$ nanoparticles is adopted from a previously published synthesis route. [19,21] An amount of 158.08 mg

of La(O^iPr) (0.5 mmol) was added to 4.68 ml of acetophenone (40 mmol) in a reaction vessel containing a stirring magnet. The vessel was sealed with a Teflon cap, taken out of the glovebox and heated at 200 °C for 20 min in a CEM Discover microwave reactor with high stirring rate. The synthesized particles were separated from the reaction liquid by centrifugation and later washed with ethanol and acetone. The powder was finally dried in air at 60 °C. Lanthanum oxycarbonate was prepared by heating the synthesized sample for two hours at 500 °C in a furnace under air with a heating ramp of 5 °C/min. The final product was cooled down to room temperature at ambient conditions. Both compounds were characterized by PXRD and HR-TEM, additionally, $La_2O_2CO_3$ was characterized with ATR-IR, as shown in Fig. 2.5 and Fig. 2.6. Information about the characterization measurements can be found below.

Discussion on the occurrence of different polymorphs fo La- an Nd- oxycarbonates. While the starting material is in both cases the corresponding hydroxide, the heat treatment is crucially different. $Nd(OH)_3$ is heated in air to form an amorphous compound, which is later on transformed to hexagonal $Nd_2O_2CO_3$ through exposure of 5000 ppm CO_2 in humid air at elevated temperatures. [19] Here, we anneal $La(OH)_3$ for 2 h at 500 °C in air, which contains about 400 ppm CO_2, and we obtain phase pure type Ia $La_2O_2CO_3$, which is considered as metastable. [24] The heating rate, final temperature and CO_2 concentration determine the free energy of transformations and thus the occurrence of the individual polymorphs.

Powder X-ray diffraction (PXRD). The PXRD data for structure refinement was collected with a Panalytical X'Pert-Pro diffractometer equipped with X'Celerator detector using Cu Kα radiation. The step size was set to 0.0334° and the counting time was 280 s per point. The powder sample was mounted in an AP HTK-1200 oven and the incident anti-scatter and divergence slit were set to 1/2° and 1/4°, respectively; on the diffracted side a 5 mm anti-scatter slit was used together with a β-Ni filter. On both sides 0.04 rad Soller slits were installed.

Attenuated total reflection infrared spectroscopy (ATR IR). Infrared analysis was performed with a Bruker ALPHA-P FT-IR spectrometer with a resolution of 4 cm^{-1} and averaged over 128 scans.

Transmission electron microscopy (TEM). TEM measurements were conducted on a Philips Tecnai F30 operated at 300 kV. A Gatan 1k CCD chip was used for image acquisition via the software Digital Micrograph.

Sensor fabrication. About 10 mg of the washed, but still wet $La(OH)_3$ powder was dispersed in 4 ml of ethanol and dip-coated on an alumina substrate. The substrate equipped with the interdigitated platinum electrodes for the resistance readout on the front side and on the back side with the platinum heaters. This substrate was dip-coated 60 times into the prepared dispersion, with a holding time of 5 s within the dispersion, 20 s for drying in air and a moving velocity of 300 mm/min. The sensor was afterwards heated under the above-mentioned conditions to obtain highly porous $La_2O_2CO_3$ films as shown in Fig. 2.7.

Structure Determination.

Structure solution. The PXRD pattern is indexed on a primitive monoclinic unit cell (a = 4.0803 Å, b = 13.5090 Å, c = 4.0720 Å, β = 90.97°, ICSD: 48-1113), using

the program TREOR [26] implemented in the software CMPR. [27] A careful examination of the diffraction pattern indicates that $h0l$ reflections with $h + l = 2n + 1$, and $0k0$ reflections with $k = 2n + 1$ are systematically absent, so the most probable space group is expected to be $P2_1/n$. As $P2_1/n$ is not a standard space group, we thus convert it to the corresponding standard space group $P2_1/c$ (a = 4.0803 Å, b = 13.5090 Å, c = 5.8131 Å, $\beta = 135.54°$) using cctbx. [35] We perform structure solution using modified direct method implemented in the software package EXPO2013. [28] After subtraction of the background using polynomial functions in selected angular intervals, the intensity of each individual reflection is extracted by using Pearson profile functions. Several initial structure models are generated, but all of them exhibit some structural similarities. Therefore, we select the best solution proposed by the program for further analysis.

Rietveld refinement. We use an initial structure model as a starting point for Rietveld refinement [29] using the program GSAS. [30, 31] We use the shifted Chebyschev function to fit the background and the peak shape function to fit the patterns is the pseudo-Voigt function. [32] We apply the surface roughness correction suggested by Suortti to minimize the intensity error introduced in Bragg-Brentano geometry. [33] The preferred orientation correction was performed using Spherical Harmonics. [34] The structure model was finally converged with Rwp = 6.039 (Rexp =3.186).

The results are presented in Table 2.1.

Gas-sensing measurements. The gas-sensing measurements were performed in a test chamber made out of Teflon, equipped with the electrodes for resistance measurements and heating of sensing layer. The atmosphere within the chamber was adjusted by a gas-mixing system. Different CO_2 pulses ranging from 250 ppm to 10 000 ppm were added to humid air (50 % relative humidity (rh)) and the resistance of the active material was measured with a Keithley Model EMM 617 electrometer.

X-ray spectroscopy. The HERFD XAS and vtc XES experiments were carried out at the European Synchrotron Radiation Facility (ESRF) in Grenoble, France, at the beamline ID26. The incident energy was selected using the (311) reflection of a double Si crystal monochromator. The incident beam had a flux on the order of 10^{13} photons/s at the sample position. The emission lines were selected with an X-ray emission spectrometer [64,65] and detected with an avalanche photodiode. In the HERFD XAS experiments the energy of the incident beam was scanned over the La L_3 edge from 5475.0 eV to 5575.0 eV with a step size of 0.1 eV and the emission spectrometer was tuned to the maximum of La $L\alpha_1$ fluorescence line at 4649.9 eV selected by the (400) reflection of one spherically bent Ge crystal analyzer. In vtc XES the incident beam energy was fixed to 5490.8 eV and the emission was recorded between 5415.0 and 5492.0 eV with a step size of 0.4 eV with five spherically bent Ge crystal analyzers using the (422) Bragg reflection.

***Ex-situ* experiments.** During the *ex-situ* experiments pellets pressed out of pure $La(OH)_3$ and $La_2O_2CO_3$ nanoparticles were measured by means of HERFD XAS and vtc XES.

***In-situ* experiments.** The sensor was placed in a gas-sensing chamber equipped with: pair of contacts for the electrical resistance measurements, pair of contacts

for applying voltages to the heater, Kapton window for XAS measurements in fluorescence mode, gas inlet, and gas outlet; further technical details are described elsewhere. [16] In a typical HERFD XAS experiment we acquired 30 scans for 3 hours at a given conditions. The sensor temperature was kept at 250 °C.

FEFF simulations. For the calculation of the HERFD XAS and vtc XES spectra the full multiple scattering calculation program package FEFF9 was used. [66, 67] The absorption and emission spectra were calculated using the COREHOLE card and dipole and quadrupole transitions were included in the calculations with the MULTIPOLE card. The core-hole lifetime broadening was reduced by 1 eV with the EXCHANGE card and the Hedin-Lundquist potential was employed. In the $La_2O_2CO_3$ calculations the Fermi energy was upshifted by 1 eV. The UNFREEZEF card was activated in order to include the f-electrons into the self-consistent potential calculations. A cluster radius of 4 Å for the self-consisting potential was employed for both materials. The full multiple scattering (FMS) sphere was set to 4 Å and to 4.5 Å for $La(OH)_3$ and for $La_2O_2CO_3$, respectively.

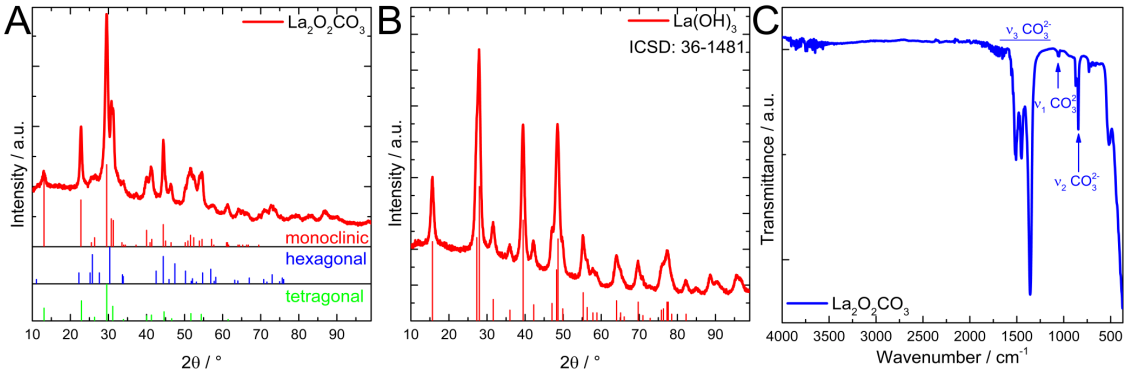

Figure 2.5: Additional PXRD and ATR-IR measurements of $La_2O_2CO_3$ and $La(OH)_3$ nanoparticles. (A) The PXRD pattern of $La_2O_2CO_3$ after two hours of heat treatment at 500 °C in air. The red vertical lines represent the reference pattern for monoclinic type Ia $La_2O_2CO_3$, the blue and green lines show the reference pattern for the hexagonal (type II, ICSD: 37-0804)) and tetragonal (type I, ICSD: 23-0320) polymorph. The formation of $Ln_2O_2CO_3$ from $Ln(OH)_3$ is a sequential process involving compositional and structural modifications. The heating rate, final temperature and CO_2 concentration determine the free energy of transformations and thus the occurrence of the individual polymorphs. (B) The PXRD patterns of the as synthesized $La(OH)_3$ nanoparticles. (C) The ATR IR spectrum of $La_2O_2CO_3$ with the characteristic absorption bands.

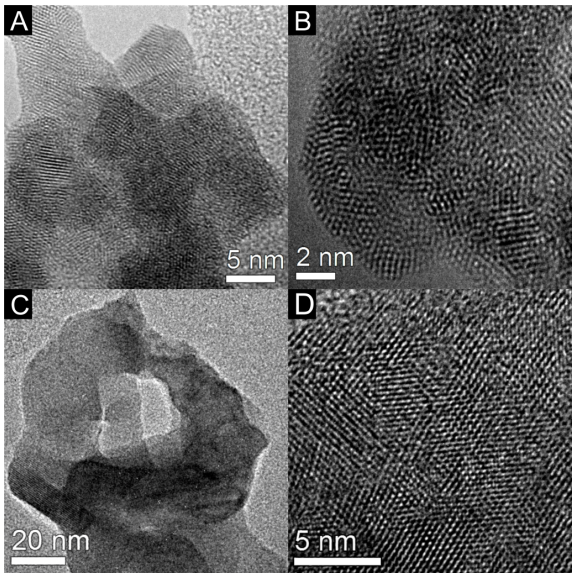

Figure 2.6: TEM images of the different nanoparticles. (A) Overview and (B) high-resolution TEM images of the as prepared $La(OH)_3$ nanoparticles. The average crystallite size is 8 nm. (C) Overview and (D) high-resolution TEM images of $La_2O_2CO_3$ nanoparticles, which were annealed for 60 hours at 250 °C in order to perform Rietveld refinement.

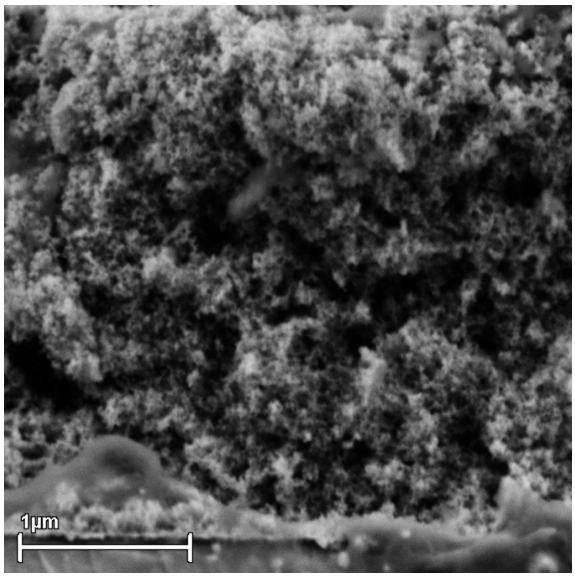

Figure 2.7: A cross section view of a $La_2O_2CO_3$ layer.

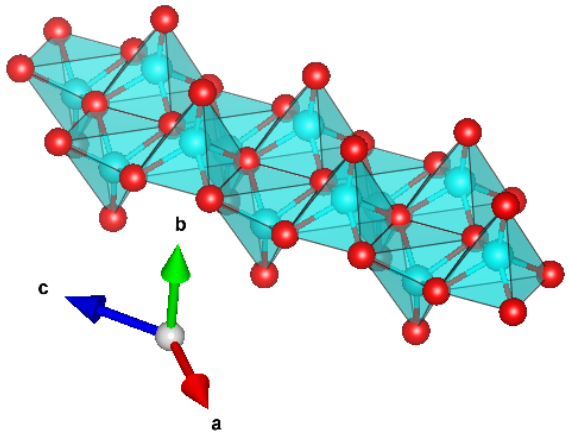

Figure 2.8: The local structure of La atoms in the $La_2O_2CO_3$ is shown. The La atoms are surrounded in a pyramidal configuration. The pyramids point in positive or negative b direction and this pointing direction changes alternately in *c* direction.

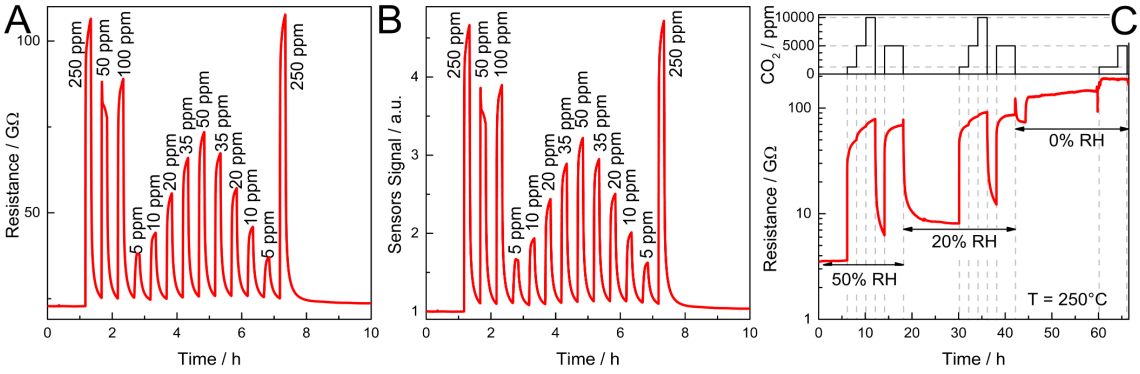

Figure 2.9: The dependence of the sensor resistance towards different gases is shown. The resistance (A) and the sensor signal (B) changes upon CO exposure gives additional information of the sensing behavior. The experiment was conducted at 250 °C and 50 % relative humidity. The increase of resistance upon CO exposure shows the p-type semiconductor behavior of the $La_2O_2CO_3$ layer. (C) The resistance changes with the relative humidity in air. The lower the relative humidity the higher the baseline resistance rises. Additionally, the sensor signal to CO_2 decreases with decreasing humidity.

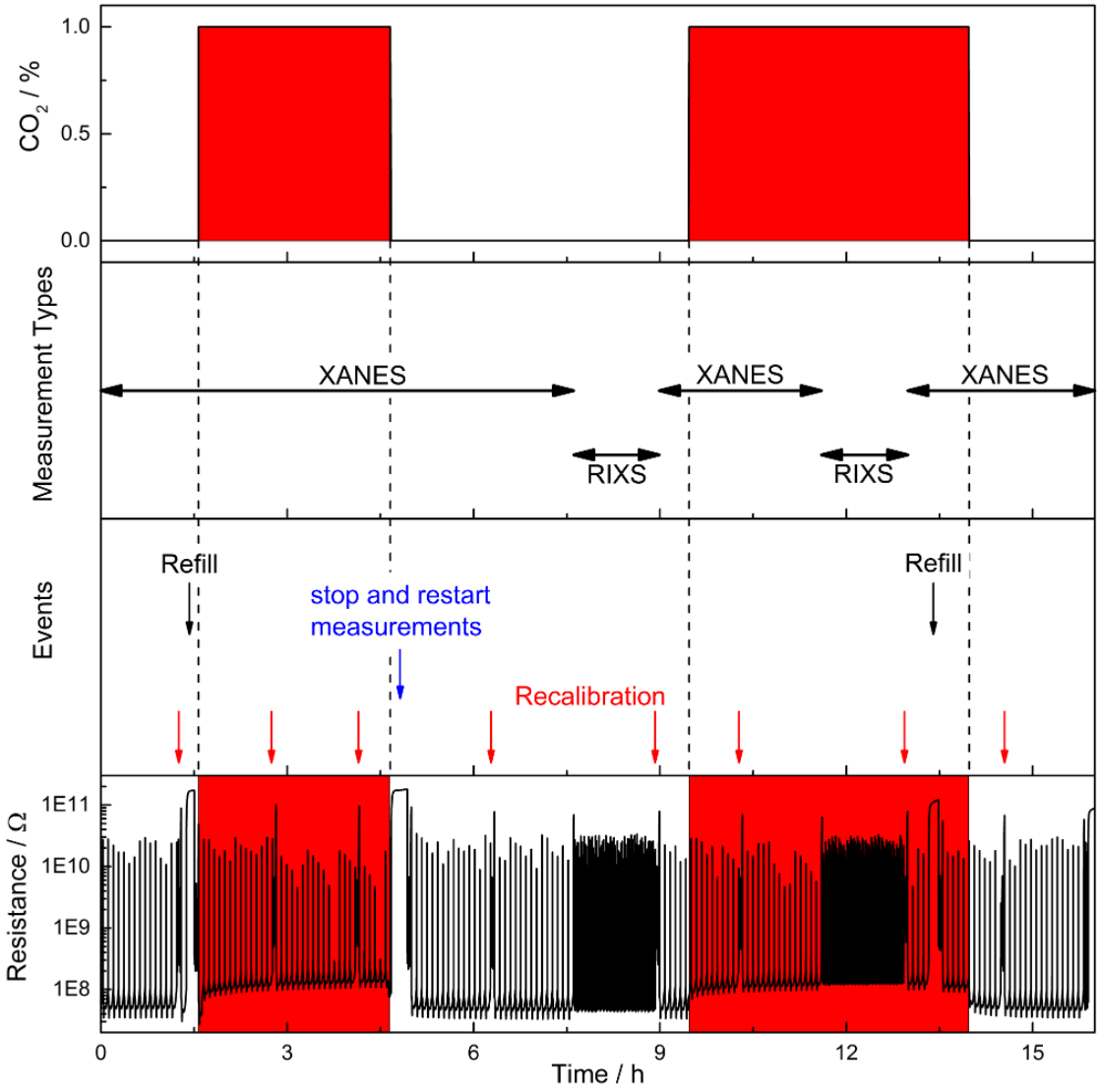

Figure 2.10: The resistance measurement of the $La_2O_2CO_3$-based sensor during acquisition of series of *in-situ* XAS and XES scans. For the sake of completeness the concentration of CO_2, scan type, recalibration of the beam and refill are indicated.

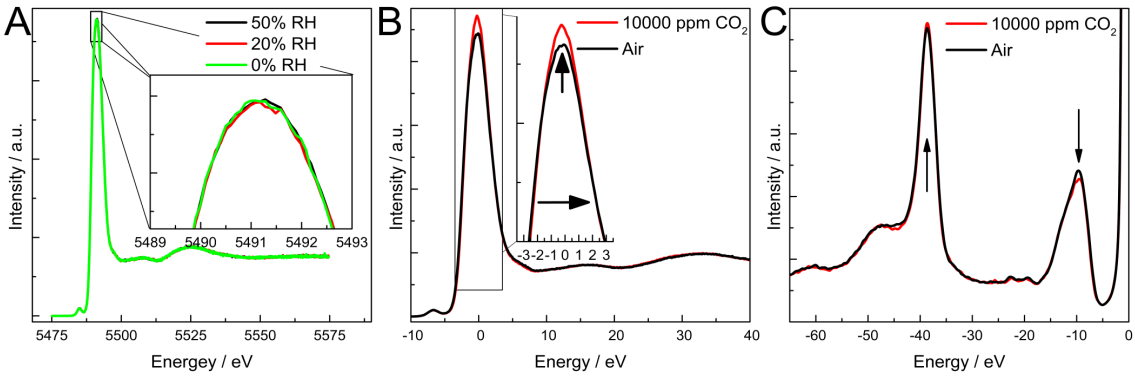

Figure 2.11: *In-situ* spectra of $La_2O_2CO_3$ under various conditions. (A) The dependence of the HERFD XAS signal to the relative humidity. Each spectrum is an average of 9 spectra. (Inset) the whiteline maximum. The relative humidity changes from 0 % (green line) over 20 % (red line) to 50 % (black line) and no difference is observable. (B) A comparison of the HERFD XAS spectra in air with 50 % rh (black line) and additional 10 000 ppm CO_2 (red line). (C) Valence-to-core XES spectra in air with 50 % rh (black line) and additional 10 000 ppm CO_2 (red line).

Table 2.1: **The atomic and refinement parameters of $La_2O_2CO_3$.** The procedure to obtain the values involved a transformation from a non-standard to a standard space group, structure determination, and Rietveld refinement. The unit cell dimension are 4.0755 Å in a, 13.489 Å in b, and 5.8033 Å in c-direction with an angle $\beta = 135.374°$ leading to a total volume of $V = 224.115\,Å^3$.

	Atomic Parameters				
Atom	x/a	y/b	z/c	Occ	Refine. para.
C	0	0	0	1	$R_{wp} = 6.039$
La	0.9872(20)	0.8370(3)	0.4762(14)	1	$R_{exp} = 3.186$
O1	0	0	0.5	1	$\chi^2 = 3.593$
O2	0.5310(13)	0.7376(33)	0.9750(79)	1	
O3	0.9200(13)	0.9161(31)	0.9435(82)	1	

Bibliography

[1] H. Furukawa, N. Ko, Y. B. Go, N. Aratani, S. B. Choi, E. Choi, A. O. Yazaydin, R. Q. Snurr, M. OKeeffe, J. Kim, and O. M. Yaghi. *Science* (2010), **329**, 424–428.

[2] A. R. Millward and O. M. Yaghi. *J. Am. Chem. Soc.* (2005), **127**, 17998–17999.

[3] M. R. Goldwasser, M. E. Rivas, E. Pietri, M. J. Pérez-Zurita, M. L. Cubeiro, L. Gingembre, L. Leclercq, and G. Leclercq. *Appl. Catal., A* (2003), **255**, 45–57.

[4] D.-X. Xue, A. J. Cairns, Y. Belmabkhout, L. Wojtas, Y. Liu, M. H. Alkordi, and M. Eddaoudi. *J. Am. Chem. Soc.* (2013), **135**, 7660–7667.

[5] D. Alezi, A. M. P. Peedikakkal, L. J. Weseliński, V. Guillerm, Y. Belmabkhout, A. J. Cairns, Z. Chen, L. Wojtas, and M. Eddaoudi. *J. Am. Chem. Soc.* (2015), **137**, 5421–5430.

[6] A. G. Bhavani, W. Y. Kim, and J. S. Lee. *ACS Catal.* (2013), **3**, 1537–1544.

[7] M. Machida, J.-i. Yabunaka, and T. Kijima. *Chem. Mater.* (2000), **12**, 812–817.

[8] M. Nyman, M. A. Rodriguez, L. E. S. Rohwer, J. E. Martin, M. Waller, and F. E. Osterloh. *Chem. Mater.* (2009), **21**, 4731–4737.

[9] R. Alonso-Mori, J. Kern, R. J. Gildea, D. Sokaras, T.-C. Weng, B. Lassalle-Kaiser, R. Tran, J. Hattne, H. Laksmono, J. Hellmich, C. Glöckner, N. Echols, R. G. Sierra, D. W. Schafer, J. Sellberg, C. Kenney, R. Herbst, J. Pines, P. Hart, S. Herrmann, R. W. Grosse-Kunstleve, M. J. Latimer, A. R. Fry, M. M. Messerschmidt, A. Miahnahri, M. M. Seibert, P. H. Zwart, W. E. White, P. D. Adams, M. J. Bogan, S. Boutet, G. J. Williams, A. Zouni, J. Messinger, P. Glatzel, N. K. Sauter, V. K. Yachandra, J. Yano, and U. Bergmann. *Proc. Natl. Acad. Sci.* (2012), **109**, 19103–19107.

[10] T. Schmitt, F. M. F. de Groot, and J.-E. Rubensson. *J. Synchrotron Radiat.* (2014), **21**, 1065–1076.

[11] P. Glatzel, J. Singh, K. O. Kvashnina, and J. A. van Bokhoven. *J. Am. Chem. Soc.* (2010), **132**, 2555–2557.

[12] N. Smolentsev, M. Sikora, A. V. Soldatov, K. O. Kvashnina, and P. Glatzel. *Phys. Rev. B* (2011), **84**, 235113.

[13] J. Singh, C. Lamberti, and J. A. van Bokhoven. *Chem. Soc. Rev.* (2010), **39**, 4754–4766.

[14] L. R. Merte, F. Behafarid, D. J. Miller, D. Friebel, S. Cho, F. Mbuga, D. Sokaras, R. Alonso-Mori, T.-C. Weng, D. Nordlund, A. Nilsson, and B. Roldan Cuenya. *ACS Catal.* (2012), **2**, 2371–2376.

[15] O. V. Safonova, T. Neisius, A. Ryzhikov, B. Chenevier, A. M. Gaskov, and M. Labeau. *Chemi. Comm.* (2005), **41**, 5202–5204.

[16] D. Koziej, M. Hübner, N. Barsan, U. Weimar, M. Sikora, and J.-D. Grunwaldt. *Phys. Chem. Chem. Phys.* (2009), **11**, 8620–8625.

[17] A. Boubnov, H. W. P. Carvalho, D. E. Doronkin, T. Günter, E. Gallo, A. J. Atkins, C. R. Jacob, and J.-D. Grunwaldt. *J. Am. Chem. Soc.* (2014), **136**, 13006–13015.

[18] D. Radu, P. Glatzel, A. Gloter, O. Stephan, B. M. Weckhuysen, and F. M. F. de Groot. *J. Phys. Chem. C* (2008), **112**, 12409–12416.

[19] I. Djerdj, A. Haensch, D. Koziej, S. Pokhrel, N. Barsan, U. Weimar, and M. Niederberger. *Chem. Mater.* (2009), **21**, 5375–5381.

[20] C. Willa, J. Yuan, M. Niederberger, and D. Koziej. *Adv. Funct. Mater.* (2015), **25**, 2537–2542.

[21] A. Haensch, D. Koziej, M. Niederberger, N. Barsan, and U. Weimar. *Procedia Eng.* (2010), **5**, 139–142.

[22] J. Schneider, H. Jia, J. T. Muckerman, and E. Fujita. *Chem. Soc. Rev.* (2012), **41**, 2036–2051.

[23] R. P. Turcotte, J. O. Sawyer, and L. Eyring. *Inorg. Chem.* (1969), **8**, 238–246.

[24] A. Olafsen and H. Fjellvag. *J. Mater. Chem.* (1999), **9**, 2697–2702.

[25] A. N. Christensen. *Acta Chem. Scand.* (1970), **24**, 2440 – 2446.

[26] P.-E. Werner, L. Eriksson, and M. Westdahl. *J. Appl. Crystallogr.* (1985), **18**, 367–370.

[27] B. Toby. *J. Appl. Crystallogr.* (2005), **38**, 1040–1041.

[28] A. Altomare, C. Cuocci, C. Giacovazzo, A. Moliterni, R. Rizzi, N. Corriero, and A. Falcicchio. *J. Appl. Crystallogr.* (2013), **46**, 1231–1235.

[29] H. Rietveld. *J. Appl. Crystallogr.* (1969), **2**, 65–71.

[30] A. C. Larson and R. B. Von Dreele. *Los Alamos Natl. Lab. Report LAUR 86-748* (1994).

[31] B. Toby. *J. Appl. Crystallogr.* (2001), **34**, 210–213.

[32] R. A. Young. *The Rietveld Method.* Oxford University Press (1993).

[33] P. Suortti. *J. Appl. Crystallogr.* (1972), **5**, 325–331.

[34] R. Von Dreele. *J. Appl. Crystallogr.* (1997), **30**, 517–525.

[35] cctbx - change space group setting.

[36] H. Li, D. Gao, P. Gao, F. Wang, N. Zhao, F. Xiao, W. Wei, and Y. Sun. *Catal. Sci. Technol.* (2013), **3**, 2801–2809.

[37] L. M. Cornaglia, J. Múnera, S. Irusta, and E. A. Lombardo. *Appl. Catal., A* (2004), **263**, 91–101.

[38] J. F. Múnera, S. Irusta, L. M. Cornaglia, E. A. Lombardo, D. Vargas Cesar, and M. Schmal. *J. Catal.* (2007), **245**, 25–34.

[39] M. O. Krause and J. H. Oliver. *J. Phys. Chem. Ref. Data* (1979), **8**, 329–338.

[40] L. Journel, J. M. Mariot, J. P. Rueff, C. F. Hague, G. Krill, M. Nakazawa, A. Kotani, A. Rogalev, F. Wilhelm, J. P. Kappler, and G. Schmerber. *Phys. Rev. B* (2002), **66**, 045106.

[41] H. Aritani, H. Yamada, T. Yamamoto, T. Tanaka, and S. Imamura. *J. Synchrotron Radiat.* (2001), **8**, 593–595.

[42] H. Asakura, T. Shishido, K. Teramura, and T. Tanaka. *Inorg. Chem.* (2014), **53**, 6048–6053.

[43] P. W. Peacock and J. Robertson. *J. Appl. Phys.* (2002), **92**, 4712–4721.

[44] N. Singh, S. M. Saini, T. Nautiyal, and S. Auluck. *J. Appl. Phys.* (2006), **100**, –.

[45] K. O. Kvashnina, S. M. Butorin, and P. Glatzel. *J. Anal. At. Spectrom.* (2011), **26**, 1265–1272.

[46] P. Glatzel, F. M. F. de Groot, O. Manoilova, D. Grandjean, B. M. Weckhuysen, U. Bergmann, and R. Barrea. *Phys. Rev. B* (2005), **72**, 014117.

[47] F. M. F. de Groot, G. Vankó, and P. Glatzel. *J. Phys.: Condens. Matter* (2009), **21**, 104207.

[48] M. F. Sunding, K. Hadidi, S. Diplas, O. M. Løvvik, T. E. Norby, and A. E. Gunnæs. *J. Electron Spectrosc. Relat. Phenom.* (2011), **184**, 399–409.

[49] M. Mikami and S. Nakamura. *J. Alloys Compd.* (2006), **408–412**, 687–692.

[50] H. Jiang, R. I. Gomez-Abal, P. Rinke, and M. Scheffler. *Phys. Rev. Lett.* (2009), **102**, 126403.

[51] J. Szlachetko, M. Pichler, D. Pergolesi, J. Sa, and T. Lippert. *RSC Adv.* (2014), **4**, 11420–11422.

[52] J. W. Chiou, H. M. Tsai, C. W. Pao, F. Z. Chien, W. F. Pong, C. W. Chen, M.-H. Tsai, J. J. Wu, C. H. Ko, H. H. Chiang, H.-J. Lin, J. F. Lee, and J.-H. Guo. *J. Appl. Phys.* (2008), **104**, 013709.

[53] M. Bär, S. Nishiwaki, L. Weinhardt, S. Pookpanratana, O. Fuchs, M. Blum, W. Yang, J. D. Denlinger, W. N. Shafarman, and C. Heske. *Appl. Phys. Lett.* (2008), **93**, 244103.

[54] Q. Mu and Y. Wang. *J. Alloys Compd.* (2011), **509**, 2060–2065.

[55] Q. Mu and Y. Wang. *J. Alloys Compd.* (2011), **509**, 396–401.

[56] N. Barsan, C. Simion, T. Heine, S. Pokhrel, and U. Weimar. *J. Electroceram.* (2010), **25**, 11–19.

[57] A. Erbil, G. S. Cargill Iii, R. Frahm, and R. F. Boehme. *Phys. Rev. B* (1988), **37**, 2450–2464.

[58] D. Vlachos, A. J. Craven, and D. W. McComb. *J. Synchrotron Radiat.* (2005), **12**, 224–233.

[59] K. J. Carroll, D. Qian, C. Fell, S. Calvin, G. M. Veith, M. Chi, L. Baggetto, and Y. S. Meng. *Phys. Chem. Chem. Phys.* (2013), **15**, 11128–11138.

[60] S. Schroeder, G. Moggridge, R. Lambert, and T. Rayment. *Spectroscopy for Surface Science*, volume 26 of *Advances in Spectroscopy*. Wiley (1998).

[61] O. V. Safonova, A. A. Guda, C. Paun, N. Smolentsev, P. M. Abdala, G. Smolentsev, M. Nachtegaal, J. Szlachetko, M. A. Soldatov, A. V. Soldatov, and J. A. van Bokhoven. *J. Phys. Chem. C* (2014), **118**, 1974–1982.

[62] P. M. Albrecht, D.-E. Jiang, and D. R. Mullins. *J. Phys. Chem. C* (2014), **118**, 9042–9050.

[63] M. Dell'Angela, T. Anniyev, M. Beye, R. Coffee, A. Fohlisch, J. Gladh, T. Katayama, S. Kaya, O. Krupin, J. LaRue, A. Mogelhoj, D. Nordlund, J. K. Norskov, H. Oberg, H. Ogasawara, H. Ostrom, L. G. M. Pettersson, W. F. Schlotter, J. A. Sellberg, F. Sorgenfrei, J. J. Turner, M. Wolf, W. Wurth, and A. Nilsson. *Science* (2013), **339**, 1302–1305.

[64] P. Glatzel and U. Bergmann. *Coord. Chem. Rev.* (2005), **249**, 65–95.

[65] P. Glatzel, M. Sikora, G. Smolentsev, and M. Fernández-García. *Catal. Today* (2009), **145**, 294–299.

[66] J. Rehr and R. Albers. *Rev. Mod. Phys.* (2000), **72**, 621–654.

[67] J. J. Rehr, J. J. Kas, F. D. Vila, M. P. Prange, and K. Jorissen. *Phys. Chem. Chem. Phys.* (2010), **12**, 5503–5513.

3 HERFD–XANES Spectroscopy as a Probe of Electron Conductivity – a Showcase for Temperature-Induced Delocalization of f-Electrons

The content of this chapter was submitted in November 2016 authored by Ofer Hirsch, Kristina O. Kvashnina, Christoph Willa, and Dorota Koziej as corresponding author.

3.1 Abstract

High energy resolution fluorescence detected (HERFD) X-ray absorption near edge structure (XANES) spectroscopy has so far mainly been applied to investigate fundamental physical phenomena in superconductors [1] and chemical reactivity of bio inorganic, photocatalytic and catalytic materials. [2–4] Even though the HERFD detection mode has been shown to be sensitive to changes of the density of unoccupied states during chemical reactions, [5, 6] it has never been used as a probe of the occupancy of semiconductor bands with delocalized electrons. Here, we show on the example of monoclinic Pr_6O_{11} nanoparticles, an n-type semiconductor with an electronic band gap of approximately 2 eV, how *in-situ* HERFD-XANES can be used as a contactless method to track the changes in occupancy of a partially filled band. We observe that the intensity variations of the HERFD-XANES features related to the tetravalent Pr ions are reversible upon heating and cooling, whereas structural and chemical transformations can be excluded. We assign these changes to the occupancy of the O $2p$-Pr $4f$-band and prove that they directly relate to changes in the electrical conductance. Our results demonstrate how HERFD-XANES can be used to particularly study *in-situ* the electronic properties of f-electrons in a semiconductor. We believe that this method can be extended to other classes of semiconducting nanomaterials. For example, for studying the electrical behavior of 2D transitional metal dichalcogenides like Cu_2S and MoS_2, [7,8] which are promising materials for electronic devices. [9, 10] Moreover, the ability to contactless monitor the change of the electronic properties of a selected component is crucial for many complex devices such as thermoelectric elements. [11]

3.2 Introduction

Although many contact techniques allow characterizing the changes of conductivity of semiconducting nanomaterials, most of them impose very strict requirements for the sample preparation, for example, the geometry and the properties of the electrical contacts. Here, we demonstrate that HERFD-XANES can be used as a contactless probe of the delocalized electrons which are taking part in the electrical conductivity. We have chosen to study mixed valence Pr_6O_{11} nanoparticles exhibiting n-type semiconductor properties and a band gap of about 2 eV. For our 7 nm large Pr_6O_{11} particles, the electronic band gap determined from valence-to-core X-ray emission spectroscopy (vtc-XES) and HERFD-XANES is 2.04 eV as shown in Supplementary Fig. 3.4. The conduction mechanism is described with the small polaron model, where the dimensions of the polarons are of the same size as the distance between two sites in the lattice. [12] We focus particularly on Pr because of the richness of spectroscopic features in the Pr L_3-edge spectrum related to f-electrons. The f-states of Pr and the O $2p$-states overlap, hybridize, and form a band. [13] The local coordination and hence the crystal structure determines the degree of hybridization and the filling level of this band. The pre-edge region probes the f-states directly via $2p \rightarrow 4f$ quadrupole transitions and a full resonant inelastic X-ray scattering (RIXS) map of this region gives further insights into the exact nature of those states. Whereas, in the HERFD-XANES spectrum, shape and position of edge and number, position and intensity of the features in the post-edge resolve the correlation between Pr valence and f-electron occupancy.

3.3 Results

The challenge in studying the mixed valence Pr_6O_{11} is to unequivocally assign the spectral features related to 3+ and 4+ valence of Pr. Thus, we study $Pr(OH)_3$ as a trivalent reference and compare its spectral features with Pr_6O_{11} as shown in Fig. 3.1. We perform the experiments at the Pr L_3 edge ($2p \rightarrow 5d$) absorption line and record the Pr $L\beta_{2,5}$ emission line ($4d \rightarrow 2p$). The spectrometer setup in HERFD-XANES reduces the core-hole lifetime broadening from 3.6 eV ($2p$) [14] to the 0.7 eV ($4d$) [15–17], which is in the range of the experimental resolution of 1 eV. In the $Pr(OH)_3$ spectrum, we assign the single feature to the $4f^2 5d^1$ state as shown in Fig. 3.1a. The $4f^3\underline{L}5d^1$, state, where $\underline{L}$ denotes a hole in the ligand O $2p$ orbital, is not visible due to broadening of Pr $5d$ states related to oxygen as neighboring atoms. [18] In the spectrum of Pr_6O_{11}, additionally to the $4f^2 5d^1$ final state characteristic for Pr^{3+}, we observe three more features, which manifest the presence of Pr^{4+} as shown in Fig. 3.1b. The quasi-cubic like surrounding of the Pr ions in the monoclinic Pr_6O_{11} results in a cubic crystal field splitting of the states into an e_g and t_{2g} state with an energy difference of 2.8 eV. [19] Thus, by analogy to CeO_2 and PrO_2, we assign the features at 5978.2 eV (blue) and 5980.9 eV (orange) to the $4f^1 5d^1$ final state. [20–23] The t_{2g} final state of $4f^2\underline{L}5d^1$ appears at 5971.0 eV, [22] whereas the e_g peak overlaps with $4f^2 5d^1$ of Pr^{3+}.

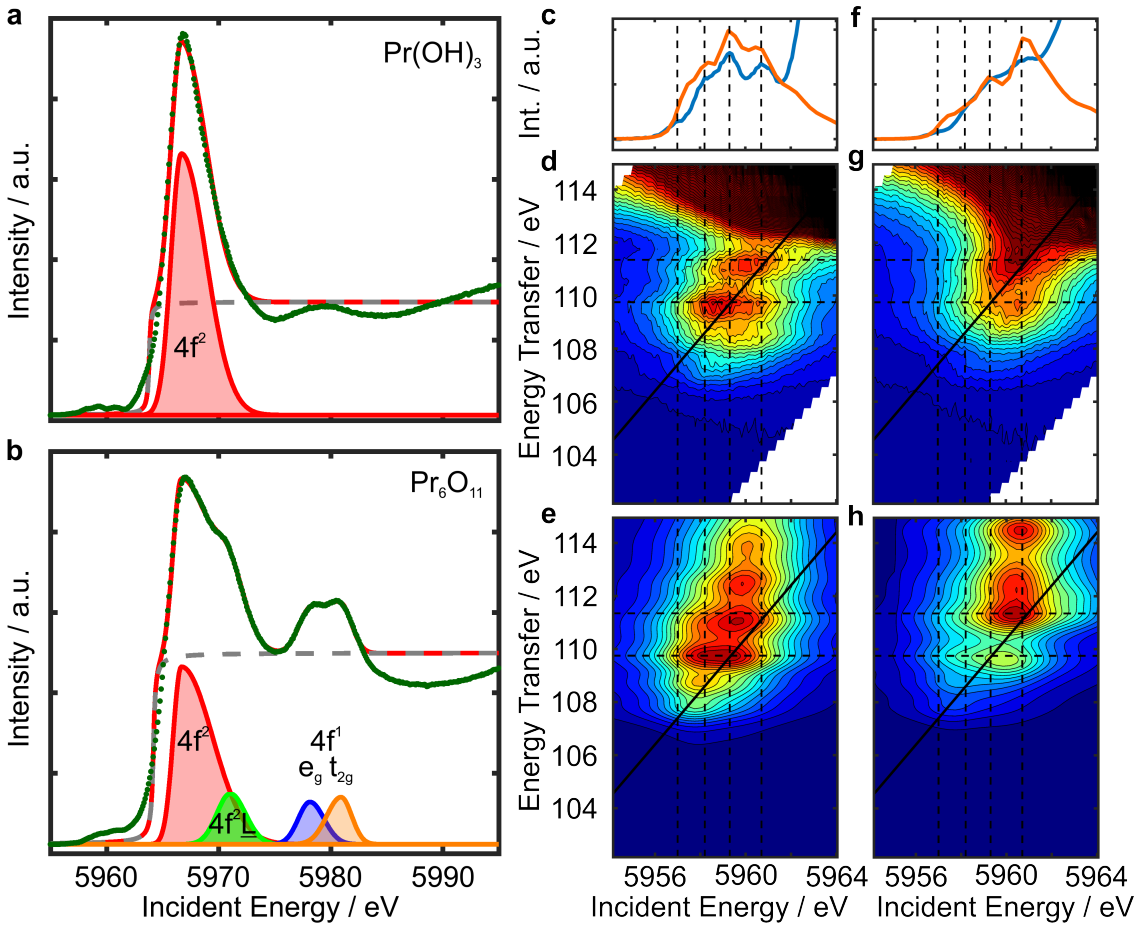

Figure 3.1: The experimental HERFD-XANES spectra (**a-b**) and experimental and calculated RIXS maps (**c-h**) of trivalent and mixed-valence praseodymium reference compounds. **a**, **b**. De-convolution of the HERFD-XANES spectra of the $Pr(OH)_3$ and Pr_6O_{11} nanoparticles, respectively. The $4f^2$ (red), $4f^2\underline{L}$ (green), and the two $4f^1$ features split by the crystal field (blue, orange) are fitted with SplitGaussians. The edge jump, fitted with an arctangent function, is shown as gray dashed line. **c-e**. The measured (**d**) and calculated (**e**) RIXS map for trivalent $Pr(OH)_3$ shows four distinct features. **f-h**. The measured (**g**) and calculated (**h**) RIXS maps of the mixed valence oxide Pr_6O_{11}. The pre-edge RIXS was calculated as a linear combination of Pr^{3+} and Pr^{4+}. The dashed lines are guidelines for the eyes. The diagonal, bold, dashed line indicates the fixed emission energy of 5849.63 eV, and the corresponding pre-edge spectra at this energy are extracted from the calculated maps (orange curve) and compared with the measured pre-edge spectra of $Pr(OH)_3$ and Pr_6O_{11} (blue curve) in (**c**) and (**f**).

From a theoretical point of view, it is challenging to treat the partly filled $4f$ orbitals of the rare-earth (RE) ions. In the sesquioxides RE_2O_3, the RE donates three electrons from the outer shells to the bond and the remaining $4f$ electrons stay strongly localized at the trivalent metal ion. [13] For Ce, Tb, and Pr also

tetravalent ions exist and due to the hybridization with the O $2p$ states the f-electron occupancy takes a non-integer value, which results in a certain degree of delocalization. Here, Pr^{3+} represents a $4f^2$ configuration and Pr^{4+} a $4f^1$ and $4f^2\underline{L}$ configuration, which includes a delocalization of the $4f$ states. The relation between those well-resolved features allows determining the f-electron occupancy (n_f) and the formal valence (v) with high accuracy. Here, the Pr^{4+}/Pr^{3+} ratio is 0.53 ± 0.13, valence $v = 3.53 \pm 0.13$, [24] which is close to the expected value of 3.66 for Pr_6O_{11}. The n_f of Pr_6O_{11} is 1.79 ± 0.04, which is as expected higher than 1.65 determined with conventional XANES for the stoichiometric PrO_2. [25]

Furthermore, in the pre-edge region we observe strong differences between $Pr(OH)_3$ and Pr_6O_{11}. We record the RIXS maps because the quadrupole transitions from $2p \rightarrow 4f$ states are differently spread out in the incident beam and energy transfer directions depending on the number of localized f-electrons, shown in Fig. 3.1c̃-h. [26] In the RIXS map calculations, we do not take into account dipole $2p \rightarrow 5d$ transitions and mixing of the $5d$ states with the $4f^2$ states, but instead solely focus on the process $2p \rightarrow 4f$ and $4d \rightarrow 2p$. For $Pr(OH)_3$, the calculated RIXS maps reproduce very well all four features with the correct broadening in incident energy and energy transfer (Fig. 3.1c-e). In the Pr_6O_{11} RIXS maps, the four features distinguished in the $Pr(OH)_3$ sample are clearly visible, but have different relative intensities due to the presence of tetravalent Pr ions (Fig. 3.1f-h). We calculate the Pr_6O_{11} maps as a linear combination of Pr^{3+} (Fig. 3.1e) and Pr^{4+} (Supplementary Fig. 3.6) maps and take two trivalent and four tetravalent ions into account. The relative intensities of the features in the calculations and the measured intensities are in the right order of magnitude, while the calcluation underestimates the broadening.

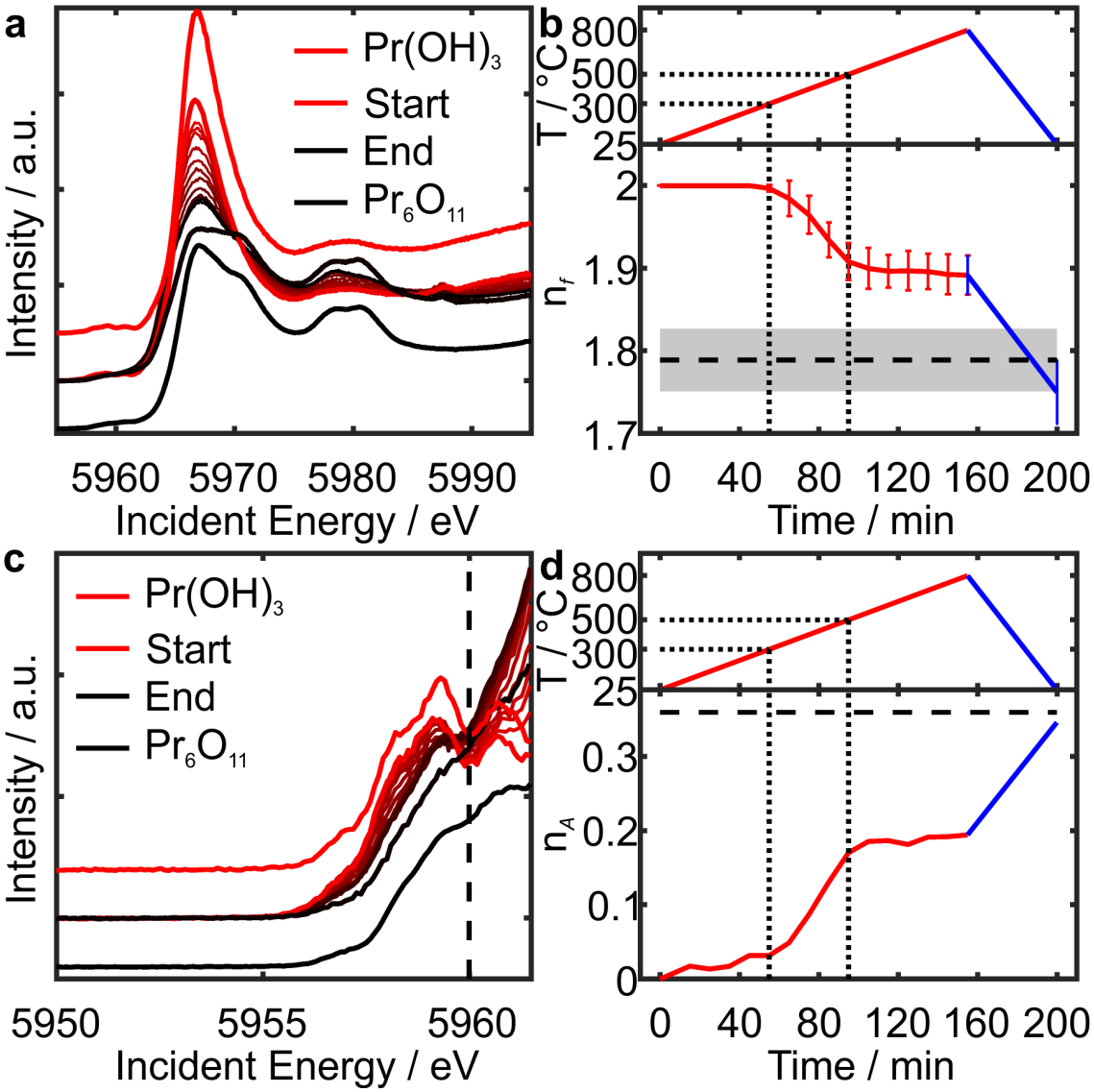

Figure 3.2: *In-situ* HERFD-XANES studies of the temperature-induced phase transition from $Pr(OH)_3$ to Pr_6O_{11}. The reference spectra of $Pr(OH)_3$ and Pr_6O_{11} measured at RT are down-/up-shifted, respectively. **a**, **b**. HERFD-XANES spectra measured at RT and then every 50 °C from 50 °C to 800 °C and the corresponding f-electron occupancy n_f as a function of time and temperature. As expected, the formation of Pr^{4+} ions at 300 °C leads to the decrease of the f-electron occupancy. Additionally, the n_f strongly decreases towards RT and reaches the *ex-situ* determined value of 1.79 ± 0.04 (gray area). This demonstrates the changing occupancy of the O $2p$-Pr $4f$ band with temperature. **c, d** Pre-edge spectra and the corresponding normalized pre-edge area, n_A, confirm the formation of Pr_6O_{11}. The increase of n_A together with the shape conservation of the pre-edge at RT after cooling down supports the higher delocalization at high temperatures rather than an oxidation of Pr^{3+} to Pr^{4+} upon cooling.

We study the emergence of Pr^{4+} by monitoring the f-electron occupancy (n_f) and

the normalized area below the pre-edge (n_A) during the temperature-induced phase transformation from $Pr(OH)_3$ to Pr_6O_{11}, as shown in Fig. 3.2 and Supplementary Fig. 3.7. At 300 °C, a decrease of n_f and an increase of n_A sets in and reaches a plateau above 500 °C. We assign these changes to the formation of Pr^{4+}, which is in line with the phase transformation from $Pr(OH)_3$ to Pr_6O_{11} observed in PXRD and TGA studies. Surprisingly, upon cooling from 800 °C to room temperature (RT) n_f and n_A further strongly change to finally reach the values measured for the reference compound at RT. The possible explanation for the sharp decrease of the n_f and increase of n_A upon cooling can be either a further oxidation of Pr^{3+} to Pr^{4+} or temperature-induced changes of the occupancy of the O $2p$-Pr $4f$ band. As shown in Supplementary Fig. 3.5, the mass loss between 800 °C and 50 °C is only 0.5 % and thus we can discard the hypothesis of oxidation of Pr^{3+} to Pr^{4+}. An inspection of the spectra measured at 800 °C and RT reveal that in both cases we observe all the post-edge features of Pr_6O_{11}, but at RT the white line maximum is flat. In the pre-edge, the two features at 5958.2 eV and 5959.3 eV are characteristic for the $4f^2$ state (Fig. 3.1c-e). For the measurements at 800 °C and RT, the relative intensities of those shoulders are very similar. However, at RT all the pre-edge features are generally shifted to higher energies. This finding supports the assumption of a higher delocalization at elevated temperatures rather than a shift from $4f^1$ to $4f^2$ or vice versa. The shift of the pre-edge to lower energies with a higher degree of f-state delocalization was observed for CeO_2 nanoparticles. [5] Furthermore, for the transition metals a temperature dependency of the quadrupole transitions due to the additional vibrational modes was reported. [27, 28]

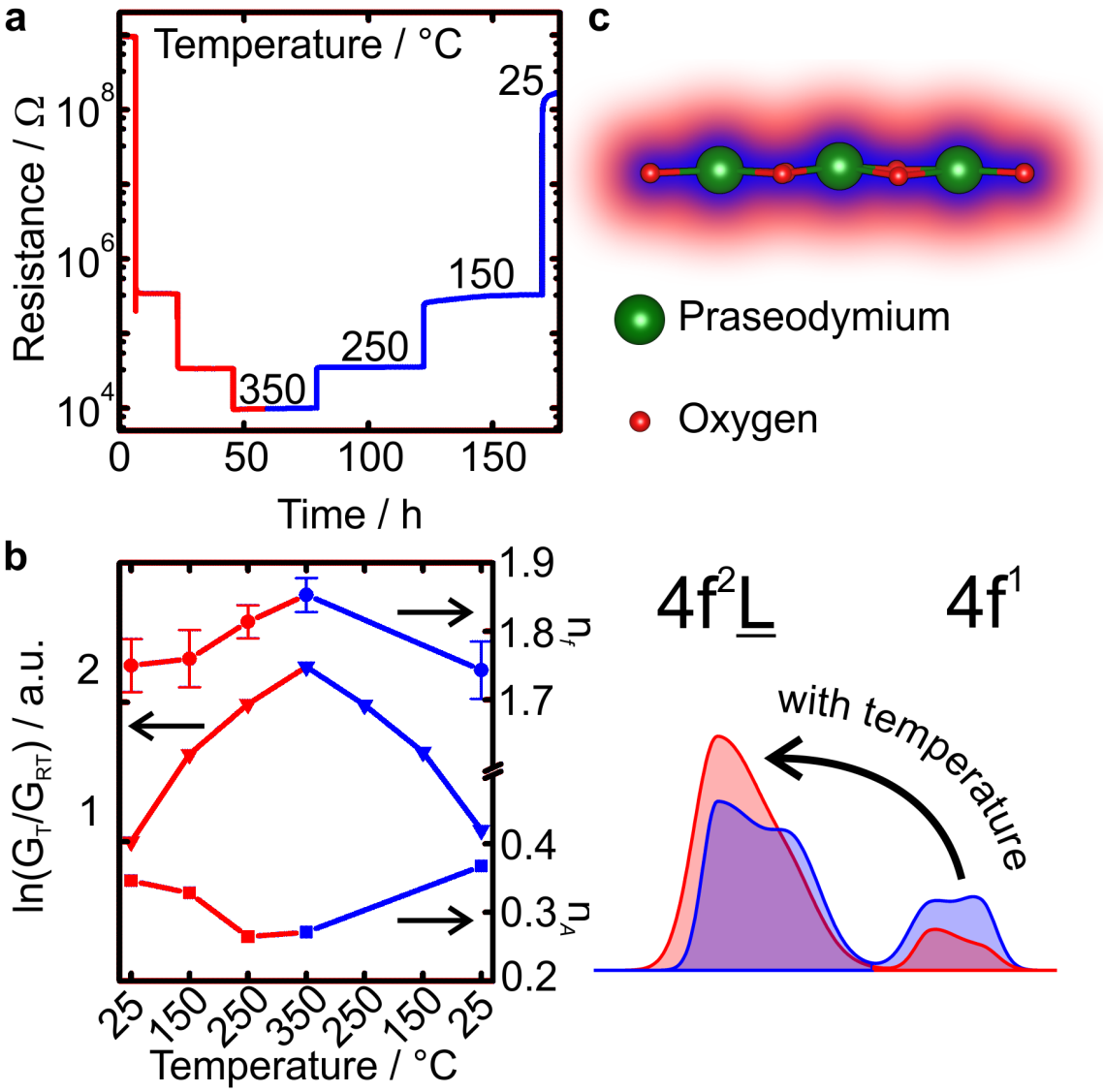

Figure 3.3: Reversible changes of the f-electron occupancy in Pr_6O_{11} upon heating and their correlation with the electrical conductance. **a**. The temperature-induced changes of resistance of Pr_6O_{11} films **b**. The dependence of the conductance, $ln(G_n/G_{RT})$, to the temperature during heating and cooling (left axis). The reversible changes of the conductance with temperature illustrate the effect of the electron delocalization on this macroscopic property. Both the analysis of the f-electron occupancy, n_f (top right axis), and the normalized pre-edge area, n_A (bottom right axis), show the higher occupancy of the O $2p$-Pr $4f$ band at higher temperature. **c**. A model of O $2p$-Pr $4f$ hybridization is shown. The $4f^2\underline{L}$ feature increases with temperature resulting in higher f-electron occupancy. (top) The artistic view on the delocalized of electrons at different temperatures and (bottom) the corresponding HERFD-XANES spectra. The blue and red colors refer to the low and high temperature, respectively.

To further test our hypothesis we heat Pr_6O_{11} nano-powders again from RT to

350 °C and compare the spectroscopic changes (n_f, n_A) with the resistance measurements of the Pr_6O_{11} films ($ln(G/G_{RT})$) as shown in Fig. 3.3a-b and Supplementary Fig. 3.8a-b. As expected for an n-type semiconductor, the resistance Rn of the Pr_6O_{11} film decreases by five orders of magnitude upon heating to 350 °C, and recovers to the almost initial value after cooling. This can be explained by the dependency of the delocalized charge carrier concentration on temperature, which is proportional to exp(-E/k_BT), where E is the energy needed to excite electrons into the conduction band. In this temperature range, we can exclude any phase transition (see Supplementary Fig. 3.8c-d) , but we still observe reversible changes of n_f and n_A upon cooling and heating. We compile all the information extracted from the HERFD-XANES studies and resistance measurements to visualize how the temperature-induced delocalization of f-electrons affects the spectral features as shown in Fig. 3.3c.

In summary, the electrical measurements are in line with the findings based on X-ray spectroscopy. Upon heating, we observe higher degree of delocalization of the f-electrons and therefore a higher electrical conductivity. We could show that the analysis of HERFD-XANES spectra and RIXS maps allows us to unambiguously distinguish between the temperature-induced changes of the Pr valence state from the changes exclusively related to delocalization of the f-electrons. Therefore, the photon-in photon-out method can be used as a contactless probe of the delocalized electrons in the conduction band of semiconductors. As worldwide high brilliance sources and emission spectrometers are under rapid development, we anticipate that this technique will find a broad application to monitor the electrical properties of semiconducting nanomaterials in operando conditions, and will be particularly interesting in the field of thermo-electrics.

3.4 Experimental and Calculational Methods

Nanoparticle synthesis. The synthesis of $Pr(OH)_3$ nanoparticles is based on the synthesis of $La(OH)_3$. [6] The chemicals were stored and handled in an oxygen- and water-free atmosphere in a glovebox and used as purchased without further purification. Acetophenone (4.68 ml, 40 mmol, 99.0 % Fluka) was added to $Pr(O^iPr)$ (159.09 mg, 0.5 mmol, 99.9 % Strem Chemicals) in a reaction vessel containing a stirring magnet. The vessel was sealed with a Teflon cap and the reaction was carried out in a CEM Discovery microwave reactor at 200 °C for 20 min. The synthesized particles were separated from the reaction liquid by centrifugation and washed twice with ethanol and once with acetone. The particles were dried at 60 °C overnight. To determine the temperature at which the phase transformation from $Pr(OH)_3$ to Pr_6O_{11} is fully completed, we measured *in-situ* PXRD (Supplementary Fig. 3.7). Finally, Pr_6O_{11} nanoparticles, used here as a reference, were obtained by heating the $Pr(OH)_3$ powder to 500 °C for 2 h with a heating rate of 5 °C/min.

X-ray spectroscopy. HERFD XANES experiments were carried out at ID26 at the European Synchrotron Research Facility (ESRF) in Grenoble, France. The incident beam energy was set to the Pr L_3 edge at 5964 eV selected with a double

Si (111) monochromator. The spectrometer in Rowland geometry was tuned to the maximum of Pr $L\beta_2$ emission line at 5849.63 eV with three spherically bent Ge (333) crystals at a Bragg angle of 77°. The total energy resolution was 0.85 eV. A typical HERFD XANES scan was measured from 5945 eV to 6050 eV with a step size of 0.1 eV and 3.5 s per step. The RIXS maps were measured from 5954 eV to 5964 eV in the incident energy range and from 5840 eV to 5857 eV in the emission energy range with a step size of 0.1 eV and 0.4 eV, respectively. The *ex-situ* measured reference samples were pressed into pellets of 2.5 mg of $Pr(OH)_3$ or Pr_6O_{11} nanoparticles and 20 mg BN. For the *in-situ* heating experiments, a capillary was filled with $Pr(OH)_3$ and placed in a custom made furnace from the ESRF sample environmental pool and heated to 800 °C with a heating rate of 5 °C/min. HERFD XANES was continuously recorded, 300 s per scan.
Valence-to-core (vtc) X-ray emission spectroscopy (XES) was measured on the same spectrometer equipped with four spherically bent Ge (333) crystals at a Bragg angle of 73°. The incident beam energy was fixed at 5976.5 eV and the emission was measured from 5890 eV to 5971.5 eV with a step size of 0.3 eV.
Multiplet Calculations. The multiplet calculations were performed with the Missing Code program [29, 30] for Pr^{3+} and Pr^{4+} ions. Firstly, the absorption process of $2p \rightarrow 4f$ quadrupole transitions were calculated, followed by the emission resulting from a $4d \rightarrow 2p$ dipole transition. The considered electron configurations were $2p^6 4d^{10} 4f^N \rightarrow 2p^5 4d^{10} 4f^{N+1} \rightarrow 2p^6 4d^9 4f^{N+1}$. The intensities of the different final states were calculated with the Kramers-Heisenberg equation, [26,31] including a core-hole lifetime broadening of the $2p$ of 3 eV and of the $4d$ hole of 0.5 eV with an instrumental broadening of 0.3 eV for the incident beam and 0.6 eV for the analyzer crystals. The calculations took $4f$-$4f$, $2p$-$4f$, and $4d$-$4f$ interactions as well as the spin-orbit coupling of the open shells into account. The values of those Slater integrals were taken from the Cowan code and were scaled to 80 % for the different interactions. The spin-orbit coupling was not scaled. The values of the reduced Slater-integrals are listed in Table 3.1.

Table 3.1: Scaled Slater Integrals for Pr^{3+} and Pr^{4+} in eV taken from the Missing-Code. Only the unfilled orbitals are shown in the header.

	$\mathbf{Pr^{3+}}$			$\mathbf{Pr^{4+}}$		
	$4f^2$	$2p^5 4f^3$	$4d^9 4f^3$	$4f^1$	$2p^5 4f^2$	$4d^9 4f^2$
$F^2\,(4f,4f)$	10.136	10.642	10.351		11.451	11.138
$F^4\,(4f,4f)$	6.366	6.689	6.511		7.239	7.046
$F^6\,(4f,4f)$	4.581	4.815	4.688		5.223	5.086
$\xi\,(4f)$	0.112	0.132	0.115	0.125	0.146	0.128
$\xi\,(2p)$		284.752			284.682	
$\xi\,(4d)$			1.397			1.424
$F^2\,(2p,4f)$		1.336			1.460	
$G^2\,(2p,4f)$		0.133			0.148	
$G^4\,(2p,4f)$		0.086			0.096	
$F^2\,(4d,4f)$			11.542			12.119
$F^4\,(4d,4f)$			7.380			7.791
$G^1\,(4d,4f)$			13.621			14.286
$G^3\,(4d,4f)$			8.557			9.033
$G^5\,(4d,4f)$			6.051			6.405

The *in-situ* HERFD-XANES data were treated with the fityk program (Version 0.9.8). [32] All normalized spectra were first fitted with an arctangent step function and the spectral features were fitted with SplitGaussians. Four such functions were fitted into the Pr_6O_{11} HERFD XANES spectra and the energy positions of the maxima were saved. Afterwards, the *in-situ* spectra were fitted with two, three, or four SplitGaussians (see text) with their maxima fixed to the *ex-situ* determined values. The areas of the fitted Gaussians were used to determine the f-electron occupancy, n_f, [5, 22, 23] with equation (3.1).

$$n_f = 1 + \frac{A(f^2) + A(f^2\underline{L})}{A_{eg}(f^1) + A_{t2g}(f^1) + A(f^2) + A(f^2\underline{L})}, \tag{3.1}$$

where, $A(f^n)$, corresponds to the area of the fitted SplitGaussians of the respective feature.

The *in-situ* pre-edge analyses were carried out with Matlab's trapz-function to obtain the area under the pre-edge up to an energy of 5960 eV (dashed line in Fig. 3.2c). We normalized the area by the area of the spectra measured at 25 °C,

$$n_A = 1 - \frac{A}{A(25\,^\circ\mathrm{C})}, \tag{3.2}$$

where A is the area below the pre-edge at a given temperature and $A(25\,^\circ\mathrm{C})$ the pre-edge area for the first *in-situ* measurement of $Pr(OH)_3$ at 25 °C.

PXRD. *In-situ* PXRD data were collected on a Panalytical Empyrean diffractometer equipped with a PIXCEL1D detector using Cu $K\alpha$ radiation (45 kV, 40 mA). The $Pr(OH)_3$ powder was prepared on a Al_2O_3 sample holder and mounted in a AP HTK-1200N oven. The incident beam optics consisted of 0.04 Soller slits, a divergence slit of 1/4°, and an antiscatter slit of 1/2°. On the diffracted beam side 0.04 Soller slits, a Ni-filter, and 1/4° divergence slit were used.
HR PXRD. Synchrotron PXRD data were collected at the Swiss-Norwegian Beamline at the ESRF with a Detrics Pilatus2M detector and an incident energy of 17.780 61 keV corresponding to a wavelength of 0.697 30 Å. The nanoparticles were filled into a quartz capillary, which was mounted on a goniometer head and rotated. The acquisition time was 60 s per sample. The analysis of the Pr_6O_{11} pattern recorded with high resolution further confirms the monoclinic Pr_6O_{11} phase (Supplementary Fig. 3.7 and 3.9).
TGA. Thermogravimetric analysis (TGA) was measured with a Mettler Toledo TGA/SDTA851^e machine. 7.71 mg of $Pr(OH)_3$ powder were put into a clean alumina crucible and heated to 800 °C with 10 °C/min heating rate in air. After cooling down to 50 °C the powder was reheated to 350 °C with 10 °C/min rate. The phase transformation is divided into three steps: removal of surface hydroxyl groups and residual organics, bulk hydroxyl groups, and the final oxide phase, as shown in Supplementary Fig. 3.4b.
Resistance Measurements. The Pr_6O_{11} film was prepared on a Al_2O_3 substrate, which was equipped with interdigitated platinum electrodes for the resistance measurements on the top side and with platinum heating electrodes on the back side. A dispersion of 200 mg of washed, but still wet, $Pr(OH)_3$ nanoparticles mixed with 5 ml of ethanol was prepared. The substrate was heated to 75 °C and 10 µl of the dispersion was drop casted ten times on the substrate. Finally, the substrate with the film was heated to 500 °C for two hours with a heating rate of 5 °C/min. The resistance was measured in a Teflon chamber, equipped appropriate electrodes for the alumina substrate. The atmosphere within the chamber was controlled with a gas mixing system and consisted of dry, synthetic air. The resistance of the film was measured with a Keithley model EMM 617 electrometer and the temperature was adjusted with a DC power supply.

3.5 Acknowledgement

We thank the Eidgenössische Technische Hochschule Zürich (ETH 2813-1) for financial support and the European Synchrotron Radiation Facility for beamtime allocation at ID26 and Swiss-Norwegian Beamlines BM01A. We thank Hugo Vittoux for the assistance with the furnace and Dr. Dmitry Chernyshov for the help with the interpretation of high-resolution PXRD data.

3.6 Supporting Information

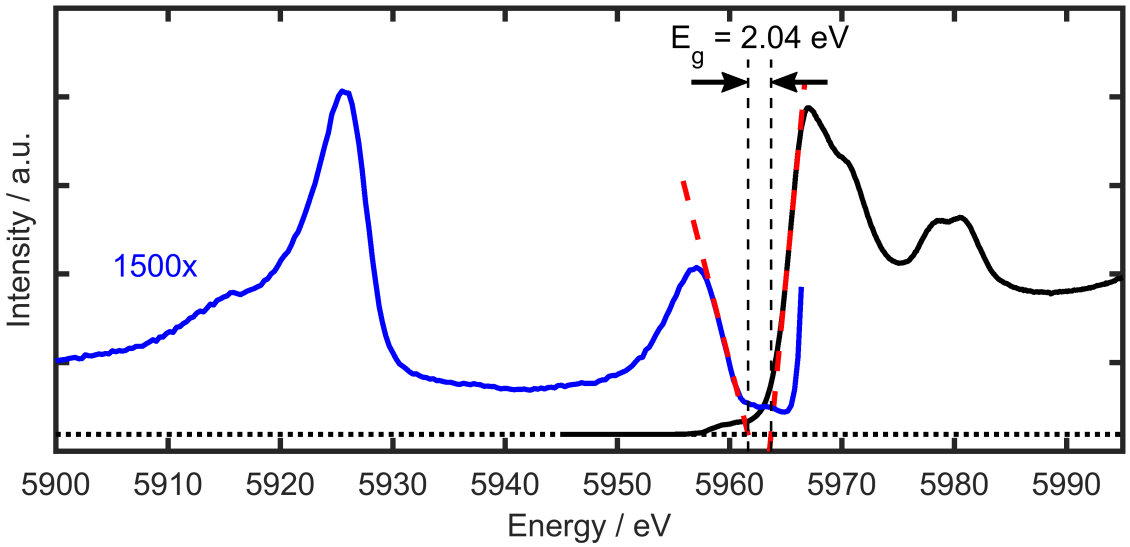

Figure 3.4: Determination of the electronic band gap based on the vtc-XES and HERFD-XANES spectra. From the combination of HERFD-XANES (black line) and vtc-XES (blue line) the electronic band gap of Pr_6O_{11} is determined. For clarity, the XES data where magnified, but the band gap determination was performed with the original data. To estimate the electronic band gap a linear fit of the absorption and emission edges (red lines) were performed. [6, 33–35]

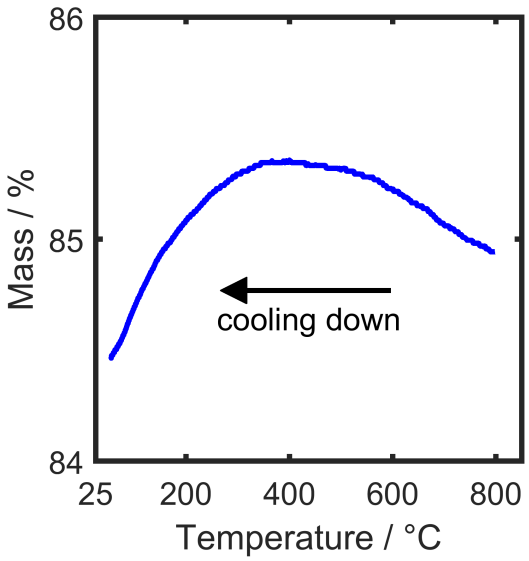

Figure 3.5: TGA measurement during cooling down of the Pr_6O_{11} powder after phase transformation. The sample gains 0.5 % of mass until 500 °C and loses about 1 % during cooling from 800 °C to room temperatures.

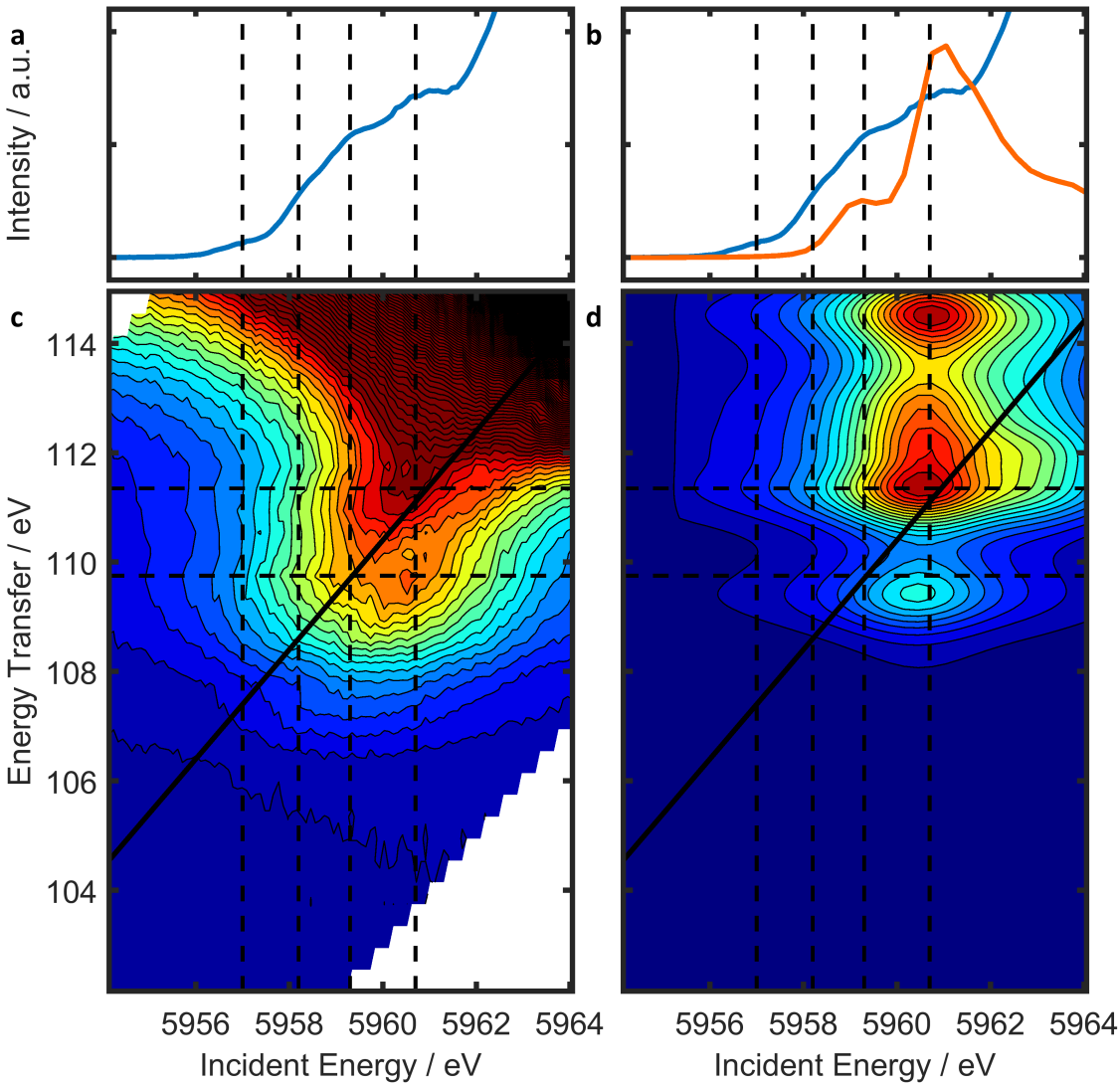

Figure 3.6: RIXS of the pre-edge of Pr_6O_{11} compared with the calculation for Pr^{4+} ions. Comparison of the measured RIXS map of praseodymium oxide (**a**, **c**) and multiplet calculations for the Pr^{4+} ion (**b**, **d**). This map was used for the linear combination to calculate the RIXS map of Pr_6O_{11}. The blue and orange curve (**a**, **b**) are extract from the measured and calculated map, respectively.

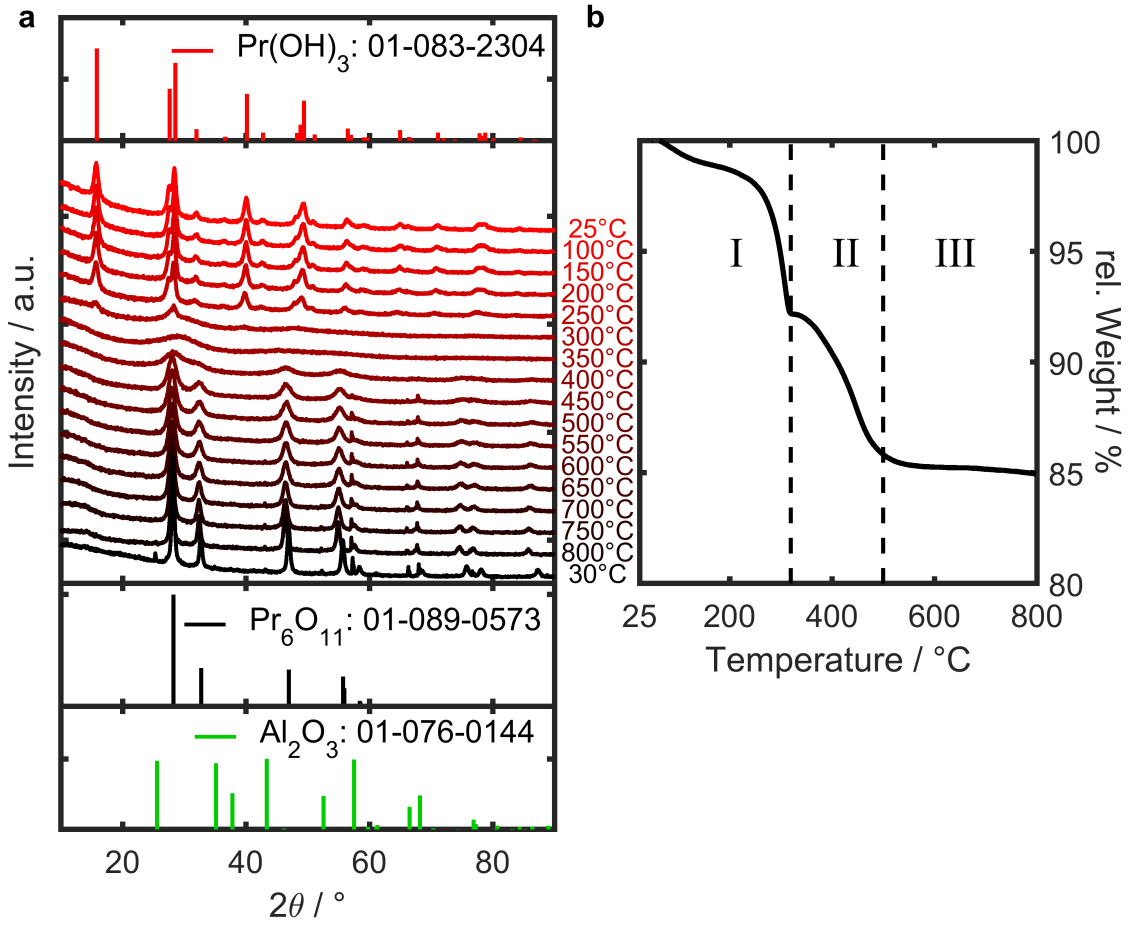

Figure 3.7: Transformation of $Pr(OH)_3$ to Pr_6O_{11} upon heating. **a**. *In-situ* PXRD studies. The initial $Pr(OH)_3$ and final Pr_6O_{11} pattern are shown on top and on the bottom, respectively, together with the peaks from the alumina sample holder. The last pattern is recorded after the sample was cooled down to RT. **b**. TGA study of $Pr(OH)_3$. Three stages are identified, (I) mass loss due to removal of surface OH-groups and residual organic species, (II) bulk OH-species leaving, and (III) stable Pr_6O_{11} nanoparticles. [36] Both PXRD and TGA measurements show the appearance of an intermediate phase between 250 °C to 450 °C.

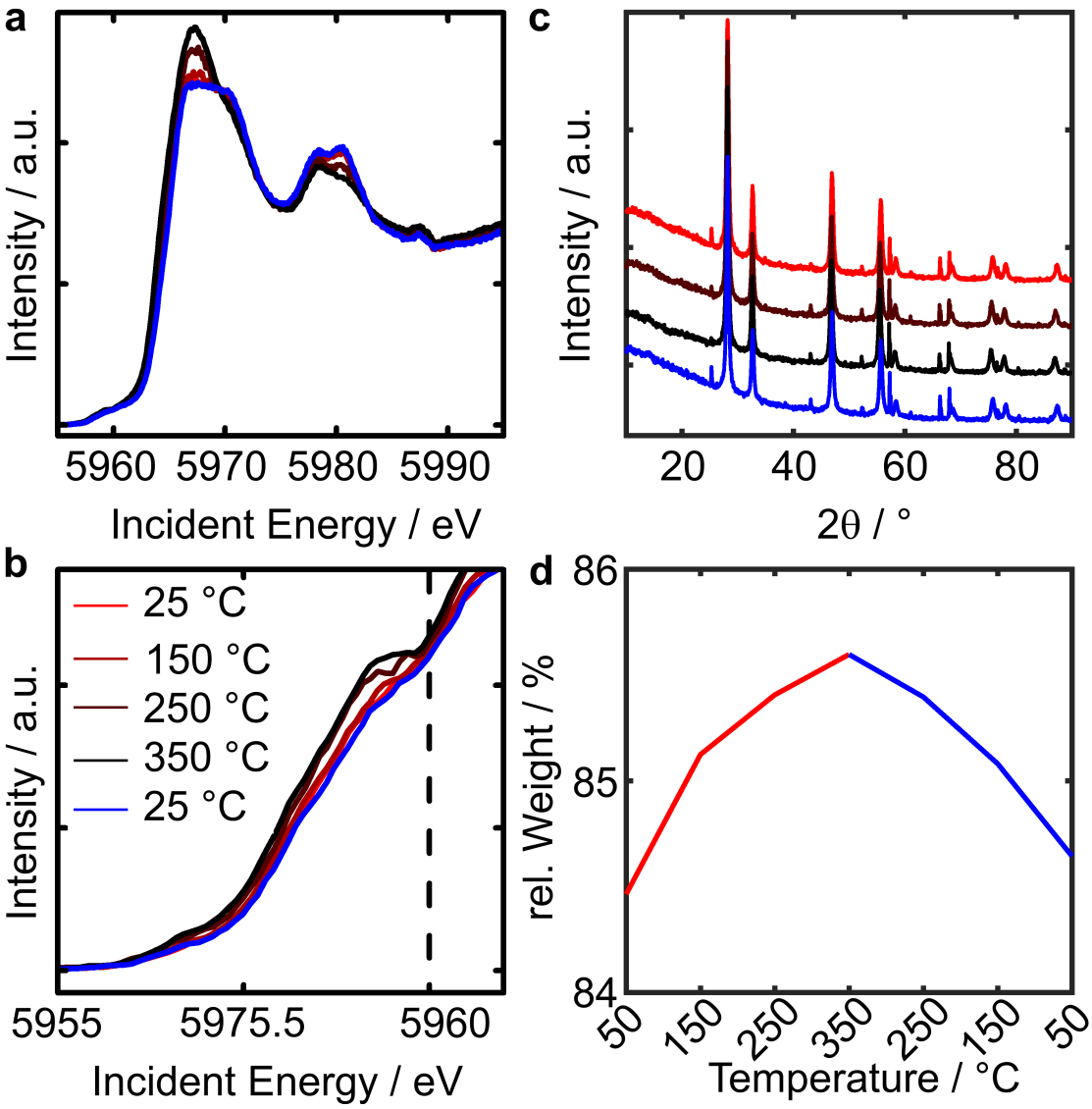

Figure 3.8: **a, b**. The HERFD-XANES spectra and the pre-edge region measured upon heating up to 350 °C and cooling to RT. The changes are fully reversible during heating (red) and cooling (blue). **c, d**. The PXRD pattern and changes in relative weight determined by TGA during heating up to 350 °C and cooling to RT. The phase of Pr_6O_{11} is stable in this temperature range and the spectroscopic changes are not related to phase and structural transformation.

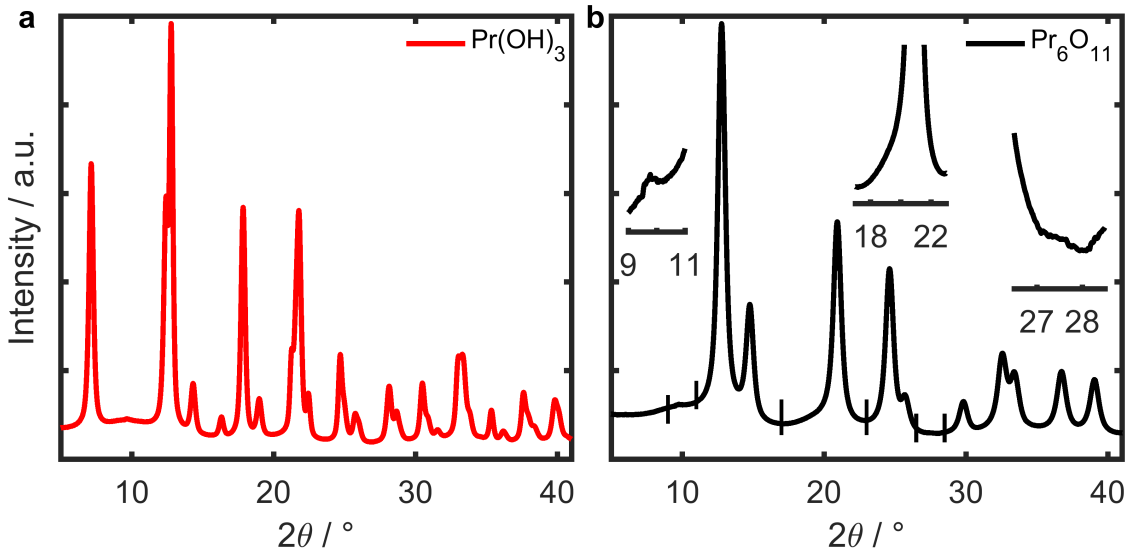

Figure 3.9: Synchrotron high-resolution PXRD pattern of **a** $Pr(OH)_3$ and **b** Pr_6O_{11}, obtained through heating $Pr(OH)_3$ to 500 °C for two hours. The insets in (**b**) magnify some features (9-11° and 26-29°) and an asymmetry (17-23°) in order to distinguish between the monoclinic Pr_6O_{11} and the cubic PrO_2, both of which have a fluorite structure either with all oxygen sites occupied (PrO_2) or not (Pr_6O_{11}). The highlighted features can only be explained with a monoclinic unit cell and a symmetry loss.

Bibliography

[1] B. J. Kim, H. Ohsumi, T. Komesu, S. Sakai, T. Morita, H. Takagi, and T. Arima. *Science* (2009), **323**, 1329 – 1332.

[2] K. M. Lancaster, M. Roemelt, P. Ettenhuber, Y. Hu, M. W. Ribbe, F. Neese, U. Bergmann, and S. DeBeer. *Science* (2011), **334**, 974 – 977.

[3] A. Boubnov, H. W. P. Carvalho, D. E. Doronkin, T. Güter, E. Gallo, A. J. Atkins, C. R. Jacob, and J.-D. Grunwaldt. *J. Am. Chem. Soc.* (2014), **136**, 13006–13015.

[4] K. A. Lomachenko, E. Borfecchia, C. Negri, G. Berlier, C. Lamberti, P. Beato, H. Falsig, and S. Bordiga. *J. Am. Chem. Soc.* (2016), **138**, 12025 – 12028.

[5] J.-D. Cafun, K. O. Kvashnina, E. Casals, V. F. Puntes, and P. Glatzel. *ACS Nano* (2013), **7**, 10726–10732.

[6] O. Hirsch, K. O. Kvashnina, L. Luo, M. J. Süess, P. Glatzel, and D. Koziej. *Proc. Natl. Acad. Sci.* (2015), **112**, 15803–15808.

[7] H. Zheng, J. B. Rivest, T. A. Miller, B. Sadtler, A. Lindenberg, M. F. Toney, L.-W. Wang, C. Kisielowski, and A. P. Alivisatos. *Science* (2011), **333**, 206 – 209.

[8] B. Radisavljevic and A. Kis. *Nat. Mater.* (2013), **12**, 815 – 820.

[9] G. Fiori, F. Bonaccorso, G. Iannaccone, T. Palacios, D. Neumaier, A. Seabaugh, S. K. Banerjee, and L. Colombo. *Nat. Nano.* (2014), **9**, 768–779.

[10] A. D. Franklin. *Science* (2015), **349**.

[11] G. J. Snyder and E. S. Toberer. *Nat. Mater.* (2008), **7**, 105 – 114.

[12] G. V. S. Rao, S. Ramdas, P. N. Mehrotra, and C. N. R. Rao. *J. Solid State Chem.* (1970), **2**, 377–384.

[13] L. Petit, A. Svane, Z. Szotek, and W. M. Temmerman. *Phys. Rev. B* (2005), **72**, 205118.

[14] M. O. Krause and J. H. Oliver. *J. Phys. Chem. Ref. Data* (1979), **8**, 329–338.

[15] S. Tanaka, H. Ogasawara, K. Okada, and A. Kotani. *J. Phys. Soc. Jpn.* (1995), **64**, 2225–2232.

[16] H. Ogasawara, A. Kotani, R. Potze, G. A. Sawatzky, and B. T. Thole. *Phys. Rev. B* (1991), **44**, 5465–5469.

[17] H. Ogasawara, A. Kotani, and B. T. Thole. *Phys. Rev. B* (1994), **50**, 12332–12341.

[18] H. Yamaoka, H. Sugiyama, Y. Kubozono, A. Kotani, R. Nouchi, A. M. Vlaicu, H. Oohashi, T. Tochio, Y. Ito, and H. Yoshikawa. *Phys. Rev. B* (2009), **80**, 205403.

[19] A. Kotani, K. O. Kvashnina, S. M. Butorin, and P. Glatzel. *Eur. Phys. J. B* (2012), **85**, 1–13.

[20] R. C. Karnatak, J. M. Esteva, H. Dexpert, M. Gasgnier, P. E. Caro, and L. Albert. *Phys. Rev. B* (1987), **36**, 1745–1749.

[21] H. Dexpert, R. C. Karnatak, J. M. Esteva, J. P. Connerade, M. Gasgnier, P. E. Caro, and L. Albert. *Phys. Rev. B* (1987), **36**, 1750–1753.

[22] A. Bianconi, A. Kotani, K. Okada, R. Giorgi, A. Gargano, A. Marcelli, and T. Miyahara. *Phys. Rev. B* (1988), **38**, 3433–3437.

[23] A. Bianconi, A. Marcelli, H. Dexpert, R. Karnatak, A. Kotani, T. Jo, and J. Petiau. *Phys. Rev. B* (1987), **35**, 806–812.

[24] H. Yamaoka, H. Oohashi, I. Jarrige, T. Terashima, Y. Zou, H. Mizota, S. Sakakura, T. Tochio, Y. Ito, E. Y. Sherman, and A. Kotani. *Phys. Rev. B* (2008), **77**, 045135.

[25] F. Tran, J. Schweifer, P. Blaha, K. Schwarz, and P. Novák. *Phys. Rev. B* (2008), **77**, 085123.

[26] K. O. Kvashnina, S. M. Butorin, and P. Glatzel. *J. Anal. At. Spectrom.* (2011), **26**, 1265–1272.

[27] O. Durmeyer, E. Beaurepaire, J. P. Kappler, B. Ch, and F. Baudelet. *J. Phys.: Condens. Matter* (2010), **22**, 125504.

[28] C. Brouder, D. Cabaret, A. Juhin, and P. Sainctavit. *Phys. Rev. B* (2010), **81**, 115125.

[29] R. D. Cowan. *The Theory of Atomic Structure and Spectra*. Los Alamos Series in Basic and Applied Sciences. University of California Press, Berkeley, California (1981).

[30] P. H. Butler. *Point Group Symmetry and Applications - Methods and Tables*. Plenum Press, New York (1981).

[31] A. Kotani and S. Shin. *Rev. Mod. Phys.* (2001), **73**, 203–246.

[32] M. Wojdyr. *J. Appl. Crystallogr.* (2010), **43**, 1126–1128.

[33] M. Bär, S. Nishiwaki, L. Weinhardt, S. Pookpanratana, O. Fuchs, M. Blum, W. Yang, J. D. Denlinger, W. N. Shafarman, and C. Heske. *Appl. Phys. Lett.* (2008), **93**, 244103.

[34] J. W. Chiou, H. M. Tsai, C. W. Pao, F. Z. Chien, W. F. Pong, C. W. Chen, M.-H. Tsai, J. J. Wu, C. H. Ko, H. H. Chiang, H.-J. Lin, J. F. Lee, and J.-H. Guo. *J. Appl. Phys.* (2008), **104**, 013709.

[35] J. Szlachetko and J. Sa. *CrystEngComm* (2013), **15**, 2583–2587.

[36] B. L. Treu, W. G. Fahrenholtz, and M. J. O'Keefe. *Inorg. Mater.* (2011), **47**, 974–978.

4 First Direct Evidence for Hybridization of f-Electrons

The content of this chapter is to be submitted in December 2016 authored by Ofer Hirsch, Kristina O. Kvashnina, Christoph Willa, and Dorota Koziej as corresponding author.

4.1 Abstract

Until now the lanthanides pre-edge structure at the L_3-absorption edge was used as a fingerprint for the number of f-electrons and thus the valence state. In this letter, we observe a new, unique f-electron behavior for Pr ions incorporated in a La matrix. We believe that the Pr $4f$ electrons form a band with the O $2p$ states and subsequently delocalize. This results in a single pre-edge peak, characteristic for a $4f^0$ configuration. Our observations are unprecedented in lanthanide physics and chemistry and we believe they will stimulate new experiments and correction in the known theories of f-electron systems.

4.2 Introduction

The recent developments in lanthanide (Ln) chemistry result in new materials relevant for applications in different fields of materials sciences such as electromechanical materials, [1] luminescent centers, [2] superconductors, [3] catalysts, [4, 5] and gas sensors. [6] Most of the properties are caused by the partially filled $4f$ orbitals, which are still poorly understood. Particularly, the chemical reactivity, [4] the magnetic properties, [7, 8] and the nature of the bonds, which can be covalent or ionic, have great impact on the materials performance. Currently, the f-electrons of the trivalent lanthanide ions are understood as localized, purely atomic states with no participation in hybridization, whereas the tetravalent ions show some delocalization of the f-states. Recent experiments showed hybridization between the f- and ligand orbitals and suggested the existence of non-ionic f-electron compounds. [9–13] In this chapter we observe for the first time a f-electron delocalization of trivalent Pr embedded in a $La(OH)_3$ matrix. Generally, doping of the host Ln materials leads to changed properties, particularly praseodymium doping shows interesting effects, such as unexpected magnetism in CeO_2 and quenching of superconductivity in $Y_{1-x}Pr_xBa_2Cu_3O_7$. [3, 8] Unlike the majority of lanthanides, Pr occurs not only as tri- but also as tetravalent ion, which results in a mixed valence oxide with high conductivity at room temperature. [14]

Nowadays we can *in-situ* study the chemistry of the f-block elements utilizing state-of-the-art emission spectrometers, which were not routinely available 15 years ago. [15] Historically, X-ray absorption (XAS) and X-ray photoemission (XPS) spectroscopy is a straightforward method to probe f-electrons of lanthanide and actinide (Ac) compounds. The XAS and XPS experiments are carried out at the M- or N-edges, where an incident X-ray photon excites a $3d$ or $4d$ electron into empty f-states, respectively. [16–19] Two new synchrotron-based techniques, high energy resolution fluorescence detection (HERFD) X-ray absorption spectroscopy and resonant inelastic X-ray scattering (RIXS), can now provide unprecedented detailed information on processes such as the electron-electron interactions, [20] hybridization between molecular orbitals, [21] the nature of the lanthanides chemical bonding, [9] and the occupation and the degree of the f-electron localization. [4] At the Ln L_3 edge, the f-electrons are probed via a quadrupole transition from an occupied $2p$ core state to empty $4f$ states utilizing hard, bulk sensitive incident X-rays. These transitions are considerably weaker than the dipole ($2p \rightarrow 5d$) white line transitions, [22] which are probed simultaneously. The emission spectrometer increases the measured energy resolution to the range of 1 eV and minimizes the background scattering, which enables the detection of weak Ln quadrupole excitations. The pre-edge features in the XAS spectrum reflect the local coordination and electronic structure. Atomic multiplet theory is an excellent tool to describe the electronic levels and line strengths of localized atomic states based on Coulomb and exchange interactions. [23–26] With this approach applied to the Ln pre-edge transitions participating in the L_3-edge RIXS process ($2p \rightarrow 4f$ absorption, $3d/4d \rightarrow 2p$ emission) an excellent agreement between the theory and experiment is found for most of investigated materials. [22, 27, 28]

Here, we study $Pr_xLa_{1-x}(OH)_3$ with easily adjustable composition of x from 0 to 1 as a model f-electron compound. To independently probe the electronic structure of Pr and La in the $Pr_xLa_{1-x}(OH)_3$ we measure HERFD-XAS spectra at Pr and La L_3 edges. Interestingly, for low Pr concentration we measure a single pre-edge peak, characteristic for a $4f^0$ configuration and not $4f^2$. Unlike commonly accepted, we suggest that the Pr $4f$ electrons, when incorporated in the $La(OH)_3$ matrix form a band with the O $2p$ states and subsequently delocalize.

4.3 Results

We synthesize $La(OH)_3$ and $Pr(OH)_3$ with a non-aqueous synthesis route from the corresponding isopropoxide in acetophenone. [6] We obtain 8 nm sized nanoparticles, which crystallize in hexagonal symmetry. Both systems occur in the same space group ($P6_3/m$) and are fully mixable. We synthesize the solid solution of $Pr_xLa_{1-x}(OH)_3$, where the Pr amount x varies from 0, 0.01, 0.05, 0.1, to 1. We show the full incorporation of Pr into the La host matrix with high-resolution powder X-ray diffraction (PXRD) measured at the Swiss-Norwegian Beamline BM01A at the European Synchrotron Radiation Facility (ESRF) at an energy of 17 780.61 eV corresponding to a wavelength of 0.697 30 Å. The patterns were measured in a capillary

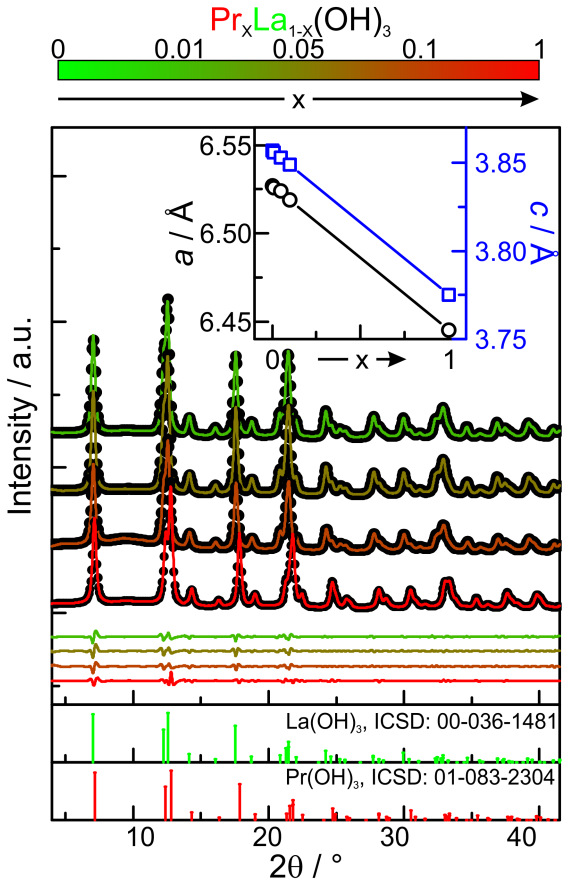

Figure 4.1: HR-PXRD patterns of the solid solution $Pr_xLa_{1-x}(OH)_3$ with $x = 0.01$, 0.05, 0.1 and 1. The data points are shown as black dots and the Rietveld-refined PXRD pattern as solid lines. The difference between fit and data is shown on the lower part with the respective color code. The inset shows the gradual change of the lattice parameter a and c. The patterns are indexed with $La(OH)_3$ and $Pr(OH)_3$ reference patterns shown at the bottom of the graph.

and recorded with a 2D Dectris Pilatus2M detector and are shown in Fig. 4.1. The red diffractogram of $Pr(OH)_3$ is fully indexed with the reference pattern for hexagonal $Pr(OH)_3$ (ICSD: 01-083-2304), whereas the $La(OH)_3$ peaks appear at lower angles (ICSD: 00-036-1481) due to the larger unit cell of this compound. With the increase of Pr concentration in the $La(OH)_3$ we observe a gradual peaks shift towards higher angles, but no peak splitting, which indicates formation of a solid solution. The refined unit cell parameters show a linear shrinkage of the lattice constants a and c with increasing concentration of Pr in La-matrix, shown in the inset of Fig. 4.1, without traces of secondary phases. The concentration of Pr in the lattice calculated based on the changes of the lattice constant agrees very well with the intended Pr concentration as shown in Table 4.1. ATR-IR measurements on the pure compounds and the $Pr_{0.1}La_{0.9}(OH)_3$ support the formation of the solid solutions as Fig. 4.4, SI shows. The band at 650 cm^{-1} arises from Ln-OH bending mode and shifts to higher wavenumbers with the incorporation of the heavier Pr

ions. [29]

Table 4.1: Refined lattice parameters from HR-PXRD and estimated doping concentration for the different samples.

Sample	a / Å	c / Å	estimated doping level
$Pr_{0.01}La_{0.99}(OH)_3$	6.526	3.856	0.012
$Pr_{0.05}La_{0.95}(OH)_3$	6.524	3.853	0.043
$Pr_{0.1}La_{0.9}(OH)_3$	6.519	3.849	0.098
$Pr(OH)_3$	6.445	3.775	1

Pr^{3+} has a $4f^2$ configuration while La^{3+} has an empty $4f$ shell thus, the successful incorporation of Pr into a La-matrix allows us to systematically study the electronic interplay between the Pr and the La-matrix. We utilize HERFD-XAS spectroscopy to independently probe the electronic structure of Pr and La ions in the $Pr_xLa_{1-x}(OH)_3$. For Pr, the most intense emission line $L\alpha_1$ ($3d \rightarrow 2p$) has an energy of 5035 eV and overlaps with the La $L\beta_1$ line at 5038 eV, which results in increase of the background intensity. Thus, here we tune the spectrometer to the maximum of the Pr $L\beta_2$ ($4d \rightarrow 2p$) emission line at 5849 eV that allows us to measure exclusively the $4f$-states of Pr ions. In the HERFD-XAS spectra the main edge provides the average valence state of Ln ion, whereas the interactions of central Ln ion with neighboring atoms in $Ln(OH)_3$ lattice determine the shape and intensity of post-edge features and can be well reproduced with FEFF calculations. [6] The main edge and post-edge features measured at La- and Pr-edges remain unchanged, independent of the concentration of Pr as shown in Fig. 4.2(a-b), respectively. The position of the main edge for the pure compounds is exactly the same as for the mixed Pr/La compound measured at both edges. Therefore, we conclude that Pr and La are trivalent, which further supports the PXRD data pointing at Pr substitution of La site. The f-electrons show strong multiplet effects in X-ray absorption spectroscopy, which dominate and determine the shape and intensity of the pre-edge. For a $4f^0$ ground state configuration only a single peak appears due to one electron in the $3d^9 4f^1$ HERFD-XAS final state. [22] At the La pre edge measured with $2p \rightarrow 4f$ absorption excitation and $L\alpha_1$ ($3d \rightarrow 2p$) emission relaxation process we observe such a single resonance, regardless of the Pr concentration as shown in Fig. 4.2(c). However, at the Pr-edge we observe major discrepancies between the pre-edge features of $Pr(OH)_3$ and $Pr_xLa_{1-x}(OH)_3$. The pre-edge of $Pr(OH)_3$ exhibits four distinct features on the basis of the multiplet splitting of the $4d^9 4f^3$ final state, shown in Fig. 4.2(d). The four features are at the energies 5957.0, 5958.2, 5959.3, and 5960.7 eV. For low concentrated Pr in the matrix the pre-edge structure changes drastically. With only 1 at % of Pr in $La(OH)_3$ we observe one single, large feature at 5957.9 eV with a small shoulder at 5960.7 eV. The other features observed in pure $Pr(OH)_3$ are not present or overshadowed by the main peak. With higher Pr concentrations we observe a decrease of relative intensity of this main feature and an increase of intensity of the four known features of pure $Pr(OH)_3$. This behavior of

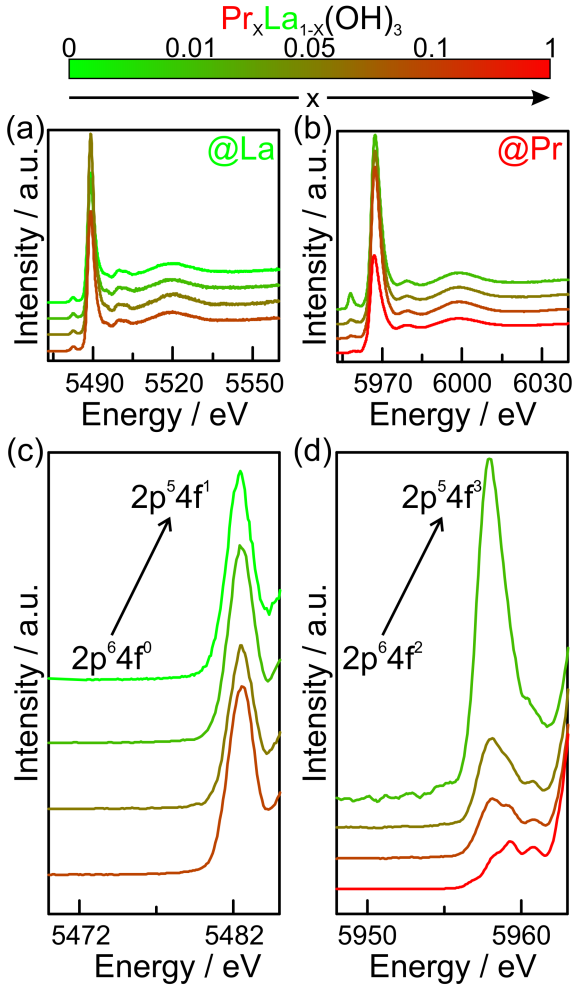

Figure 4.2: Comparison of HERFD-XAS spectra of the solid solution of $Pr_xLa_{1-x}(OH)_3$ with $x = 0$, 0.01, 0.05, 0.1 and 1. The spectra measured at the La-edge show no dependency of the main edge (a) and pre-edge (c) features upon variation of the Pr concentration. The single pre-edge resonance shows the $4f^0$ ground state configuration of La. At the Pr-edge, the main edge features (b) are similar for the different Pr concentrations owing to a similar coordination, whereas the pre-edge structure (d) shows strong changes with different Pr level, ranging from a single feature for 1 at% doping to four features in the pure $Pr(OH)_3$. The assumed pre-edge absorption process is highlighted in (c, d) for La^{3+} and Pr^{3+}.

the pre-edge shape of f-electron systems of the lanthanides and actinides compounds is unexpected and was never observed before.

Even more striking is that the shape of the Pr pre-edge peak of $Pr_{0.01}La_{0.99}(OH)_3$ and the La pre-edge peak look identical, suggesting a similar f-electron configuration. The pre-edge region of Ln HERFD-XAS spectra resolves very well the f-electron configuration and thus reflects also the valence state of the absorbing atoms. [22] Particularly, the single peak excitations in the pre-edge can only appear in case of the f^0 ground state configuration, which is the case for La^{3+} but never

for Pr^{4+} and Pr^{3+}. Though, for Pr to appear in a $4f^0$ ground state configuration it should be in a valence of +5, which was recently reported to be possible for gas phase compounds. [30] However, the main edge position of the Pr L_3 edge lies at the characteristic 3+ energy position and thus the changes of the pre-edge behavior of Pr in $La(OH)_3$ cannot be accounted for by changes of the valence state.

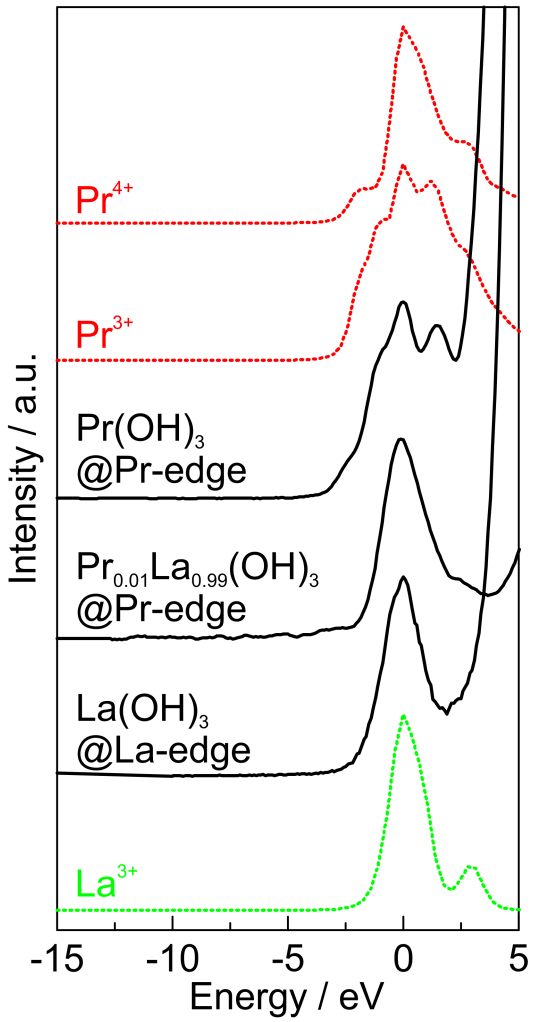

Figure 4.3: Comparison of the pre-edge structures of $La(OH)_3$ measured at the La edge, 1 at % Pr:$La(OH)_3$ and $Pr(OH)_3$ measured at the Pr edge (solid lines). The dotted lines are diagonal cuts in the RIXS maps obtained by atomic multiplet calculations of the corresponding photon-in/photon-out process (Fig. 4.5, SI). Those cuts correspond to the HERFD-XAS process and are taken at the maxima of the features in the maps. The Pr^{3+} and La^{3+} calculations fully reproduce the $Pr(OH)_3$ and $La(OH)_3$ pre-edge structures, respectively. The pre-edge features of the 1 at % Pr:$La(OH)_3$ exhibits a $4f^0$ configuration.

The similarities between the Pr and La pre-edge peak in $Pr_{0.01}La_{0.99}(OH)_3$ are not only in the single resonance but also in the width and shape of this feature.

Normalizing the respective pre-edge resonance to its maximum and shifting said maximum to an arbitrary energy of zero, we see that the pre-edges are nearly identical, shown as solid lines in Fig. 4.3. The comparison of the normalized and shifted HERFD-XAS spectra showsS the difference in energy separation between the white line maximum and the pre-edge maximum, which is 9.2 eV and 6.6 eV for the Pr and La edge, respectively. Generally, the energy difference between the pre-edge and the white line maximum is directly related to the valence shell electron density and the higher this density is, the lower the pre-edge peak will appear due to stronger Coulomb interactions between the d core-hole and the $4f^{n+1}$-states rather than the $5d^1$ state. [31]

From pre edge studies on transition metal oxides the sensitivity of the pre-edge shape and intensity to the crystal field is known, and was recently observed for the first time on the f-states of Th. [9] The splitting is usually not accounted for in the $2p \rightarrow 4f$ transitions of Ln compounds, since the crystal field acting on the f-electrons is in the order of 100 meV and thus smaller than the experimental resolution. The La-O distance in $La(OH)_3$ is 2.588 Å, while the Pr-O distance is only 2.540 Å in $Pr(OH)_3$, thus the small changes in the Pr-O distance can energetically favor certain f-orbitals and the resulting pre-edge shape changes accordingly. In Nd-doped $La(OH)_3$ we do not observe these tendencies at the pre-edge, as shown in Fig. 4.6 SI, even though the Nd-O distance is also extended from 2.524 Å to the aforementioned 2.588 Å. Thus we exclude a crystal field effect and the changes are rather connected to the nature of Pr as an ion and its ability to form Pr $4f$-O $2p$ hybridization. Interestingly though, with higher Pr concentration in the sample this effect at the pre-edge vanishes and the pre-edge structure exhibits the atomic f-electron configuration, identifiable by the four features. This is accompanied by a steady shrinkage of the unit cell with higher Pr concentration, as the Rietveld analysis of the PXRD pattern in Fig. 4.1 reveals. While the crystal field does not cause the observed delocalization, we identify the average Pr-O bond distance as part of the reason of this pre-edge behavior.

So far, only indirect measurements on actinocenes, Ln-oxides, and Ln-chlorides at the ligand K-edge pointed out a possible covalence and delocalization of the $4f$ and $5f$ states. [10–13, 32] Here, the most crucial observation of the single resonance at the Pr L_3 edge directly shows a La-like $4f$-electron configuration on the Pr ions and results in a $4f^0$ ground state and therefore in a delocalization of those electrons. The comparison of the experimental data with atomic multiplet calculation [23, 33] for Pr^{3+} ($4f^2$), Pr^{4+} ($4f^1$), and La^{3+} ($4f^0$) further emphasizes that we observe a La pre-edge like excitation while measuring directly at the Pr L_3 edge by the HERFD XAS technique as shown in Fig. 4.3 and Fig. 4.5, SI. The single pre-edge feature of the 1 at % Pr:$La(OH)_3$ exhibits the same shape as the calculated $4f^0$ atomic multiplet calculations. In our case, while electrons are missing in the atomic configuration, we still detect Pr in the state +3 and conclude that the ions are well screened with delocalized electrons of the valence band of the compound. The higher electron density screens in the absorption-emission process the created core-hole and shifts the pre-edge peak to lower energies. [31] This explains the different energy separation between the pre-edge and white line maximum. In the Pr-sesquioxide, Pr_2O_3, the

$4f$ and $5d$ states are close in energy leading to an orbital hybridization and easier delocalization, which is not the case for La_2O_3. [13] This observation for Pr supports our hypothesis of delocalization either through hybridization with the O $2p$ ligand orbitals or via a hybridization of the Pr $4f$ with the La/Pr $5d$ band.

Our findings are unique for the f-electron systems. Until now, the pre-edge structure of the Ln and actinide ions is used as an equivalent measure of the formal valence and thus the f-electron configuration. Here we observe an unusual shape of the pre-edge structure and explain it by the hybridization of the molecular orbitals and interaction of the f-electrons with the oxygen neighbors and possibly other Ln atoms in the compound. The alternative explanations as formation of Pr^{5+} or crystal field splitting can either be ruled out or cannot account for the extent of the changes observed in the pre-edge Pr features of $Pr_{0.01}La_{0.99}(OH)_3$ compound.

We believe that our observations will trigger new experiments and help developing a unified theory to truly understand the role of f-electrons of rare-earth and actinide dopants. The principal difficulties for the theoreticians are the multiple interactions involved in the spectroscopic processes, such as hybridization, electron screening, electron-electron and electron-phonon interactions. Most theories sacrifice at least one interaction or parameter in an effort to explain a single experiment, while comparisons between theory and different experimental methods are necessary. On the long term, a single, unified theory might help explaining a recently discovered giant-orbital-paramagnetism induced by a minute amount of extrinsic lanthanide defects. [7, 8]

4.4 Acknowledgement

We thank the Eidgenössische Technische Hochschule Zürich (ETH 2813-1) for financial support and the European Synchrotron Radiation Facility for beamtime allocation at ID26 and Swiss-Norwegian Beamlines BM01A. We thank Dr. Dmitry Chernyshov for the help with the interpretation of high-resolution PXRD data.

4.5 Supporting Information

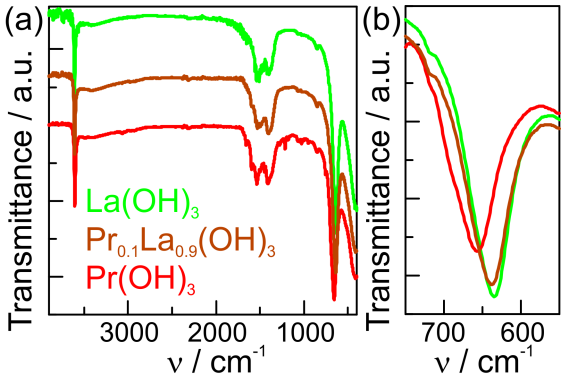

Figure 4.4: ATR-IR spectra of the pure $La(OH)_3$ and $Pr(OH)_3$ and the $Pr_xLa_{1-x}(OH)_3$ with 10 at % Pr in (a) with the RE-O bond vibration magnified in (b). The different masses of La and Pr shift the RE-O bond vibration with the doped sample in the middle.

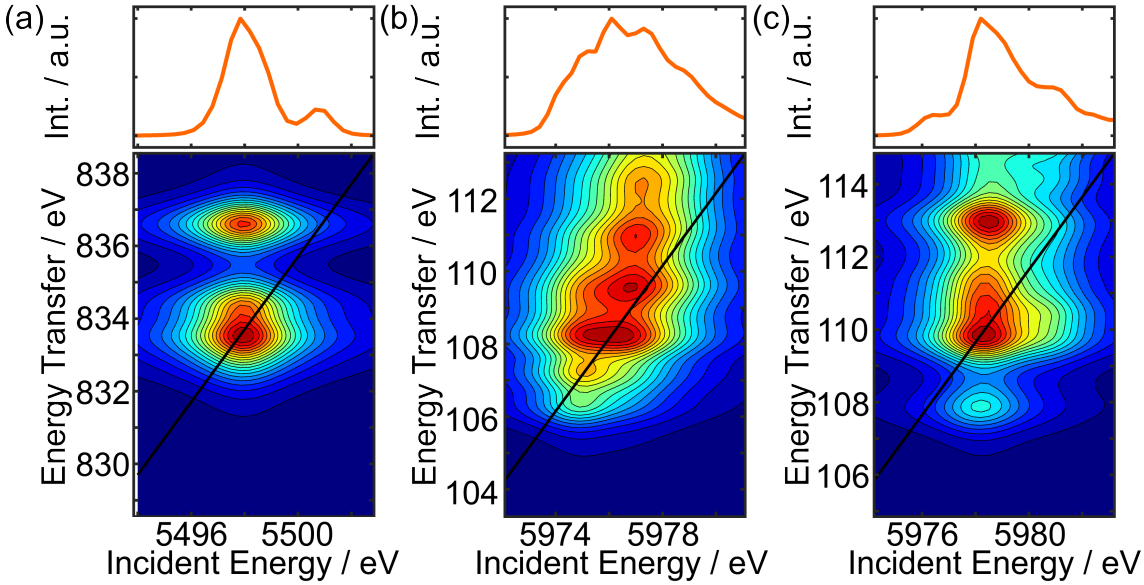

Figure 4.5: Atomic multiplet calculations of the pre-edges of (a) La^{3+}, (b) Pr^{3+}, and (c) Pr^{4+} ions for the whole RIXS process. In all cases, the absorption process is an excitation of a $2p$ core-electron into a $4f$ state. For La the $L\alpha_1$ ($3d \rightarrow 2p$ emission) is implemented, whereas for Pr the $L\beta_2$ ($4d \rightarrow 2p$) emission line is calculated. The diagonal black cut is the HERFD-XAS, which is shown in the top part of each map. The high-energy part of the line scan is overshadowed by the white line in the experimental HERFD-XAS spectra. For La we observe one single feature, whereas the $4f^2$ and $4f^1$ configuration of Pr^{3+} and Pr^{4+}, respectively, show multiple features due to f-f interactions.

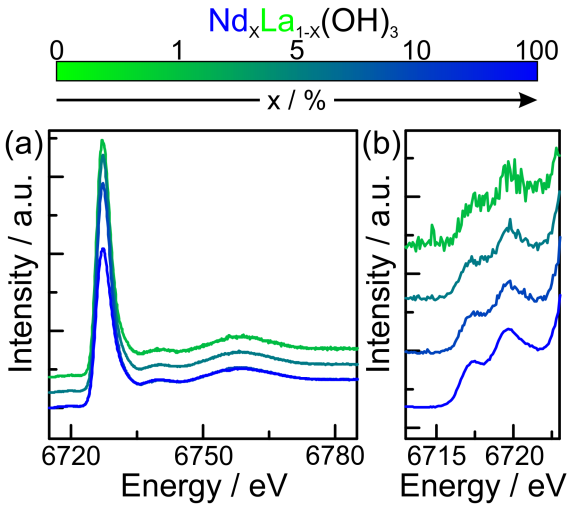

Figure 4.6: (a) The main and (b) pre-edge HERFD-XAS spectra of the solid solution of $Nd_xLa_{1-x}(OH)_3$ with $x = 0.01$, 0.05, 0.1 and 1 measured at the Nd-edge. No dependency of the pre- or main-edge on the dopant concentration is observable. This excludes that the pre-edge effect observed on Pr results from crystal-field effects, but rather lies in the nature of the Pr ion to easily hybridize.

Bibliography

[1] Y. Li, O. Kraynis, J. Kas, T.-C. Weng, D. Sokaras, R. Zacharowicz, I. Lubomirsky, and A. I. Frenkel. *AIP Adv.* (2016), **6**, 055320.

[2] A. Lauria, I. Villa, M. Fasoli, M. Niederberger, and A. Vedda. *ACS Nano* (2013), **7**, 7041–7052.

[3] H. Yamaoka, H. Oohashi, I. Jarrige, T. Terashima, Y. Zou, H. Mizota, S. Sakakura, T. Tochio, Y. Ito, E. Y. Sherman, and A. Kotani. *Phys. Rev. B* (2008), **77**, 045135.

[4] J.-D. Cafun, K. O. Kvashnina, E. Casals, V. F. Puntes, and P. Glatzel. *ACS Nano* (2013), **7**, 10726–10732.

[5] O. V. Safonova, A. A. Guda, C. Paun, N. Smolentsev, P. M. Abdala, G. Smolentsev, M. Nachtegaal, J. Szlachetko, M. A. Soldatov, A. V. Soldatov, and J. A. van Bokhoven. *J. Phys. Chem. C* (2014), **118**, 1974–1982.

[6] O. Hirsch, K. O. Kvashnina, L. Luo, M. J. Süess, P. Glatzel, and D. Koziej. *Proc. Natl. Acad. Sci. U. S. A.* (2015), **112**, 15803–15808.

[7] M. Coey, K. Ackland, M. Venkatesan, and S. Sen. *Nat. Phys.* (2016), **12**, 694 – 699.

[8] N. Paunovic, Z. Dohcevic-Mitrovic, R. Scurtu, S. Askrabic, M. Prekajski, B. Matovic, and Z. V. Popovic. *Nanoscale* (2012), **4**, 5469–5476.

[9] S. M. Butorin, K. O. Kvashnina, J. R. Vegelius, D. Meyer, and D. K. Shuh. *Proc. Natl. Acad. Sci. U. S. A.* (2016), **113**, 8093–8097.

[10] M. W. Löble, J. M. Keith, A. B. Altman, S. C. E. Stieber, E. R. Batista, K. S. Boland, S. D. Conradson, D. L. Clark, J. Lezama Pacheco, S. A. Kozimor, R. L. Martin, S. G. Minasian, A. C. Olson, B. L. Scott, D. K. Shuh, T. Tyliszczak, M. P. Wilkerson, and R. A. Zehnder. *J. Am. Chem. Soc.* (2015), **137**, 2506–2523.

[11] S. G. Minasian, J. M. Keith, E. R. Batista, K. S. Boland, D. L. Clark, S. D. Conradson, S. A. Kozimor, R. L. Martin, D. E. Schwarz, D. K. Shuh, G. L. Wagner, M. P. Wilkerson, L. E. Wolfsberg, and P. Yang. *J. Am. Chem. Soc.* (2012), **134**, 5586 – 5597.

[12] S. G. Minasian, J. M. Keith, E. R. Batista, K. S. Boland, D. L. Clark, S. A. Kozimor, R. L. Martin, D. K. Shuh, and T. Tyliszczak. *Chem. Sci.* (2014), **5**, 351–359.

[13] A. B. Altman, J. I. Pacold, J. Wang, W. W. Lukens, and S. G. Minasian. *Dalton Trans.* (2016), **45**, 9948–9961.

[14] C. Bonnelle and N. Spector. *Rare-Earths and Actinides in High Energy Spectroscopy*. Progress in Theoretical Chemistry and Physics. Springer Netherlands, Dordrecht, Netherlands (2015).

[15] K. Hämäläinen, D. P. Siddons, J. B. Hastings, and L. E. Berman. *Phys. Rev. Lett.* (1991), **67**, 2850–2853.

[16] B. T. Thole, G. van der Laan, J. C. Fuggle, G. A. Sawatzky, R. C. Karnatak, and J. M. Esteva. *Phys. Rev. B* (1985), **32**, 5107–5118.

[17] H. Ogasawara, A. Kotani, and B. T. Thole. *Phys. Rev. B* (1994), **50**, 12332–12341.

[18] H. Ogasawara, A. Kotani, R. Potze, G. A. Sawatzky, and B. T. Thole. *Phys. Rev. B* (1991), **44**, 5465–5469.

[19] A. Bianconi, A. Kotani, K. Okada, R. Giorgi, A. Gargano, A. Marcelli, and T. Miyahara. *Phys. Rev. B* (1988), **38**, 3433–3437.

[20] M. Sikora, A. Juhin, T.-C. Weng, P. Sainctavit, C. Detlefs, F. de Groot, and P. Glatzel. *Phys. Rev. Lett.* (2010), **105**, 037202.

[21] P. Glatzel, A. Mirone, S. G. Eeckhout, M. Sikora, and G. Giuli. *Phys. Rev. B* (2008), **77**, 115133.

[22] K. O. Kvashnina, S. M. Butorin, and P. Glatzel. *J. Anal. At. Spectrom.* (2011), **26**, 1265–1272.

[23] R. D. Cowan. *The Theory of Atomic Structure and Spectra*. Los Alamos Series in Basic and Applied Sciences. University of California Press, Berkeley, California (1981).

[24] A. Kotani and H. Ogasawara. *Phys. B* (1993), **186**, 16–20.

[25] G. van der Laan. *Hitchhiker's Guide to Multiplet Calculations*, pages 143–199. Springer Berlin Heidelberg, Berlin, Heidelberg (2006).

[26] F. de Groot and A. Kotani. *Core Level Spectroscopy of Solids*. Advances in Condensed Matter Science. CRC Press (2008).

[27] K. O. Kvashnina, S. M. Butorin, P. Martin, and P. Glatzel. *Phys. Rev. Lett.* (2013), **111**, 253002.

[28] K. O. Kvashnina, Y. O. Kvashnin, and S. M. Butorin. *J. Electron Spectrosc. Relat. Phenom.* (2014), **194**, 27–36.

[29] Q. Mu and Y. Wang. *J. Alloys Compd.* (2011), **509**, 2060–2065.

[30] Q. Zhang, S.-X. Hu, H. Qu, J. Su, G. Wang, J.-B. Lu, M. Chen, M. Zhou, and J. Li. *Angew. Chem., Int. Ed.* (2016), **55**, 6896–6900.

[31] F. Bartolomé, J. M. Tonnerre, L. Sève, D. Raoux, J. Chaboy, L. M. García, M. Krisch, and C. C. Kao. *J. Magn. Magn. Mater.* (1999), **196**, 779–781.

[32] W. W. Lukens, M. Speldrich, P. Yang, T. J. Duignan, J. Autschbach, and P. Kogerler. *Dalton Trans.* (2016), **45**, 11508–11521.

[33] P. H. Butler. *Point Group Symmetry and Applications - Methods and Tables.* Plenum Press, New York (1981).

5 Conclusion and Outlook

In-situ high-resolution X-ray spectroscopy studies of rare-earth materials are scarce. Thus the major objective of the presented thesis was to investigate fundamental aspects of La- and Pr-based materials and relate the spectroscopic findings to macroscopic properties. La occurs always in a trivalent state and thus the electron valence shell configuration stays unchanged, which makes it a good candidate to study the changes in the local coordination induced by adsorption of gaseous molecules. Pr, unlike most of the lanthanides, occurs not only in tri- but also in tetravalent state, thus forming localized and delocalized f-electrons.

The first example presents a detailed *in-situ* study of $La_2O_2CO_3$ during its chemoresistive response to CO_2. The combination of HERFD XAS and vtc XES shows a charge tranfer between CO_2 and $La_2O_2CO_3$. The changes in the occupied and unoccupied density of states upon interaction with CO_2 reveals an additional oxygen neighbor at a La surface site. The increase of CO_2 concentration in the atmosphere demands new materials for its photo-/electrocatalysis, sensing, and storage. In those applications, the selective interaction of CO_2 and a charge transfer with solids is in the foreground. The presented example showcases how to access the key information.

In the second example, the temperature-induced phase transformation of $Pr(OH)_3$ to Pr_6O_{11} was investigated by PXRD and HERFD XAS. The analysis of the HERFD XAS and RIXS maps of the reference compounds assigns the spectral features to the tri- and tetravalent ions. In Pr_6O_{11}, a temperature dependency of the spectral features was observed and related to a higher occupancy of the O $2p$-Pr $4f$ band. We can correlate the temperature-induced changes of f-electron delocalization with the electrical conductivity. In the future, this concept can be extendend and used as a indirect, contactless probe of delocalized electrons in the conduction band of semiconductors.

The last example focussed on the hybridization between Pr $4f$ and neighboring orbitals. For the first time a drastically changed pre-edge feature in the RE HERFD XAS was measured in 1 at % Pr-doped $La(OH)_3$. The pre-edge of Pr^{3+} with a $4f^2$ configuration shows the same characteristics as the pre-edge of La^{3+} with its $4f^0$ state. The Pr ions in the $La(OH)_3$ form a hybridization with the O $2p$ or La $4f/5d$ states and thus the Pr $4f$ electrons delocalize. This changes the view of the $4f$ electrons, which are generally believed to be highly localized on the atom.

Until now, *in-situ* RE X-ray spectroscopy focussed on localized f-states and changes in the valence and local coordination. This thesis highlights the importance of treating f-electrons not only in a localized but also delocalized approach. Especially for Pr, with its mixed valence, photon-in/photon-out spectroscopy can answer open questions in high-temperature superconductors. [1] Furthermore, novel

magnetic phenomena [2] arise from RE doping into CeO_2, while the participating electronic states are still unknown. The observation and approaches presented in this thesis will trigger new experiments and will, potentially, lead to a development of a unified theory for f-electron physics and chemistry.

Bibliography

[1] H. Yamaoka, H. Oohashi, I. Jarrige, T. Terashima, Y. Zou, H. Mizota, S. Sakakura, T. Tochio, Y. Ito, E. Y. Sherman, and A. Kotani. *Phys. Rev. B* (2008), **77**, 045135.

[2] M. Coey, K. Ackland, M. Venkatesan, and S. Sen. *Nat. Phys.* (2016), **12**, 694 – 699.

6 Beyond High-Resolution X-ray Spectroscopy - Characterization of Nanoparticles with EXAFS

This chapter contains three examples how extended X-ray absorption fine structure (EXAFS) is utilized to gain information about the local structure of nanoparticles. It underlines efforts that were undertaken during the PhD to perform various kinds of spectroscopic investigations. The incorporation of Ni in MoO_2 is adressed in detail in the first part of this chapter. For Co and $ZnFe_2O_4$ only the representitive abstracts are given.

6.1 Aliovalent Ni in MoO_2 Lattice - Probing the Structure and Valence of Ni and Its Implication on the Electrochemical Performance

The content of this chapter was published in Chemistry of Materials 2014, 26, pp 4505 - 4513 by Ofer Hirsch, Guobo Zeng*, Li Luo, Malwina Staniuk, Paula M. Abdala, Wouter van Beek, Felix Rechberger, Martin J. Süess, Markus Niederberger, and Dorota Koziej as corresponding authors. (* equal contribution)*

6.1.1 Abstract

Here, we present a synthesis of MoO_2 nanoparticles doped with 2 at% of Ni in a mixture of acetophenone and benzyl alcohol at 200 °C. Based on *in-situ* X-ray absorption near-edge structure (XANES) and *ex-situ* extended X-ray absorption fine structure (EXAFS) measurements at Ni K-edge and Mo K-edge, we discuss scenarios on how the "doping" reaction, i.e. the incorporation of Ni in the MoO_2, proceeds. We can clearly exclude the formation of NiO or Ni nanoparticles. Moreover, within the resolution of our *in-situ* XANES experiments, we observe that the ternary compound Ni:MoO_2 nucleates directly in the final composition. Although the local structure around the Ni ion adopts the MoO_2 crystal structure pointing at the substitution of tetravalent Mo by Ni, we find that Ni remains divalent. This aliovalent substitution results in the relaxation of the local structure, which is additionally reflected in the slight shrinking of the total volume of the unit cell of Ni:MoO_2. Interestingly, such

a small amount of divalent Ni has a tremendous effect on the performance of the material as anode in Li-ion batteries. The discharge capacity of Ni:MoO_2 based anodes almost doubles from 370 mA h g^{-1} for MoO_2 to 754 mA h g^{-1} for Ni:MoO_2 at 0.1C (1C = 370 mA g^{-1}). Additionally, we observed an atypical increase of capacity for both MoO_2 and Ni:MoO_2 anodes upon cycling with increasing cycling rate.

6.1.2 Introduction

The incorporation of foreign ions in a host lattice is the most powerful approach to tailor the electronic, [1–5] photonic, [6–8] and magnetic [9] properties of materials. In the case of nanoparticles, the presence of even small quantities of foreign ions can additionally influence their crystal structure, stability, size, and morphology. [10–15] Thus, although the impact on the properties is indisputable, the role of dopants is rather manifold than unequivocal. In general, for materials with metallic conductivity, any foreign ion is considered as an additional scattering center for charge carriers, decreasing their mean free path and causing a decrease of the electronic conductivity of the materials. [16] Molybdenum dioxide is one of the few metal oxides intrinsically exhibiting metallic conductivity and a work function between 5 and 6.5 eV. These properties make MoO_2 an attractive material for electrodes in CMOS technology, [17] solid-state fuel cells, [18] and Li-ion batteries. [19–25] But when it comes to real applications, MoO_2 electrodes are rather unstable leading to a short lifetime of the corresponding devices. Doping in general improves their stability but at the same time compromises their electrical conductivity. Additionally, most reported examples include only solid solutions of MoO_2 with tetravalent metal oxides described as $M_xMo_{1-x}O_2$, where M is W, Ti, or Si and x varies between 0.1 and 0.9. [19, 26–29] Example where MoO_2 is doped with minute amounts of aliovalent ions are scarce and not related to their applications as electrodes. [30]
Here, we report a straightforward solution-based route to incorporate 2 at% of divalent Ni into the lattice of MoO_2. The Ni concentration is kept low in order to maintain the metallic conductivity of the MoO_2 nanoparticles. First, we determine the influence of the Ni on the structural properties of the host lattice by refinement of powder X-ray diffraction (PXRD) patterns and fitting of EXAFS data recorded at the Mo K-edge. Second, we elaborate the valance and the position of Ni in the lattice by analysis of XANES and EXAFS data recorded at the Ni K-edge. An obvious technological target is the fabrication of MoO_2 electrodes. For that reason, we utilize Ni:MoO_2 nanoparticles as an anode material for Li-ion batteries and they show significantly improved performance in comparison to MoO_2.

6.1.3 Experimental Section

Chemicals.
Anhydrous benzyl alcohol (≥ 99.8 %), acetophenone (99.0 %), molybdenum (VI) dioxide dichloride, nickel (II) acetate tetrahydrate (99.998 %) were supplied by Sigma Aldrich, nickel (II) oxide by J.T. Baker, ethanol (≥99.8 %) by Fluka and acetone

(≥99.5 %) by Sigma Aldrich. The chemicals were used without further purification.
Synthesis.

(a) MoO_2: Molybdenum (VI) dioxide dichloride (200 mg) was added in an oxygen- and water-free atmosphere to a mixture of anhydrous benzyl alcohol (10 ml) and acetophenone (5 ml). The 15 ml reaction solution was transferred into a 45 ml Teflon liner, sealed in a Paar acid digestion bomb and placed in an oven for 48 hours at 200 °C. After cooling down, the precipitate was centrifuged, washed with acetone and ethanol and the resulting powder was dried in an oven at 60 °C.
(b) Ni:MoO_2: Molybdenum (VI) dioxide dichloride (1710 mg) and nickel acetate tetrahydrate (112.63 mg) were added to a mixture of benzyl alcohol (60 ml) and acetophenone (30 ml). Then 15 ml of the reaction solution was poured into a 50 ml Teflon liner. The synthesis was performed analogously to the MoO_2. The initial concentration of Ni in the reaction solution was 5 at%. The obtained concentration was 1.3 or 1.9 at% of Ni in MoO_2, based on the PXRD refinement and EDX measurements, respectively. For the simplicity, throughout the text we refer to 2 at% Ni concentration.
(c) *In-situ* synthesis of Ni:MoO_2. The synthesis was performed analogously to the aforementioned synthesis, but the reaction was heated in a special cell described elsewhere. [31, 32] The volume of the reaction cell was 1.13 ml. The temperature of the cell was raised to 215 °C and kept at this temperature for 11 hours.
Nanoparticles characterization.
(a) XAS data were recorded at the Swiss-Norwegian Beamline (SNBL) BM01, European Synchrotron Research Facility (ESRF). XAS data of the corresponding powder pellets were measured from 19.900 to 21.000 keV (Mo) and from 8.250 to 8.900 keV (Ni). The measurements at Mo K-edge were done in continuous scanning mode with two ion chambers, one before and one after the sample. The measurements at Ni K-edge were recorded with a Vortex EM fluorescence detector equipped with Xia digital electronics. The reference powders were diluted in cellulose to compensate for self-absorption and pressed into pellets. The step size of the XAS measurement for Mo and Ni was 1 eV and 0.5 eV, respectively.
(b) PXRD patterns from powders in quartz capillaries were recorded at the Swiss-Norwegian Beamline (SNBL), using a wavelength of 0.504 79 Å. A two-dimensional Dexela 2923 CMOS X-ray detector was installed at a distance of 408 mm from the sample, with a 75 µm × 75 µm pixel size. [33] The PXRD data were extracted from the two-dimensional ring patterns by radial integration with Fit2D. *In-situ* PXRD patterns were recorded on the X'Pert Pro (PANalytical B. V., Netherlands) powder diffractometer operating in reflection mode with Cu Kα radiation (45 kV, 40 mA) equipped with Anton Paar heating chamber.
(c) TEM micrographs were recorded with a Philips Tecnai F30 operated at 300 kV. A gatan 1k CCD chip was used for image acquisition via the software Digital MicrographTM.
(d) Energy-Dispersive X-ray Spectroscopy (EDX) was performed on a Hitachi SU-70 scanning electron microscope operated at an acceleration voltage of 30 kV (Schottky type field emission gun) and equipped with an X-Max 80 detector from Oxford Instruments. The quantitative results of EDX analysis measured at three different

locations were averaged over lifetime of 300 s.

***In-situ* methods.**

The *in-situ* XAS data were collected at the SNBL at the ESRF. The beam spot size at the front window of the sample cell containing the reaction solution was ∼5 mm × ∼0.7 mm and the beam passed through the sample over a length of 1 mm. The sample volume was constantly irradiated during the time of reaction. The spectra form the same spot were taken every 24.5 minutes. The data acquisition was identical with the aforementioned XAS measurements.

Data analysis.

(a) The Rietveld refinement was performed using the program GSAS. [34, 35] The shifted Chebyschev function was used to fit the background, and the peak shape function used to fit the patterns was the pseudo-Voigt function. [36] The preferred orientation correction was performed using Spherical Harmonics. [37] The average crystal size was calculated by Scherrer Equation using all peaks, and the doping level was obtained by refining the atomic occupancy.

(b) We performed the EXAFS data reduction using the ATHENA software. [38] For the normalization, we used the pre-edge range from 19.924 to 19.964 keV post-edge from 20.095 to 20.994 keV for the Mo samples. The value of E_0 was set to 20.013 keV for MoO_2 and 20.014 keV for Ni:MoO_2 that is the position of the maximum of the first derivative. For Ni:MoO_2 measured at the Ni-edge the normalization is realized with a pre-edge range from 8.265 to 8.315 keV and with a post-edge range from 8.495 to 8.888 keV. The value E_0 was set to 8.345 keV. The photon energy was converted to photoelectron wavenumbers k. The resulting χ(k)-function was k^3 weighted and the range between 2.3 and 13 $Å^{-1}$ at the Mo-edge and 2.3 and 11 $Å^{-1}$ at the Ni-edge were Fourier transformed using a Hanning window function.

(c) MCR-ALS method. XANES spectra of Mo K-edge were analyzed with the MCR-ALS method. [31, 39, 40] The number of components was chosen on the basis of Singular Value Decomposition (SVD) results (details in supporting information (SI) Figure 6.8). The initial spectra of components were estimated based on SIMPLISMA method [41–43] with the noise level of 2 %. The ALS algorithm with following constraints was applied: (1) non-negativity of spectra and concentrations, (2) unimodality of concentrations, (3) convergence criterion: 0.1. Further details are given in SI.

Carbon coating and electrochemical measurements.

30 wt% of glucose monohydrate (puriss) was dissolved in deionized H_2O and 70 wt% of MoO_2 was added and homogenously mixed under mechanical stirring for 3 minutes. 0.1 ml of the as-prepared suspension was then transferred onto a petri dish-like titanium current collector with diameter of 13 mm and depth of 1 mm. The suspension was dried out in a vacuum oven at 60 °C and a thin film was directly formed on the current collector. It was calcined in a tube furnace at 650 °C in N_2 for 6 hours with ramping rate of 3 °C min^{-1}, resulting in black thin films with overall mass load of $\sim$ 2.5 mg cm^{-2}. To ensure that the crystal structure and size of nanoparticles did not change during carbon coating we measured *in-situ* PXRD shown in SI Figure 6.9. The films on the current collectors were directly used as electrodes without any additional additives, later assembled into Swagelok-type cells in an argon-filled

glovebox (H_2O & $O_2 < 0.1$ ppm). Lithium metal (99.9 %, Alfa-Aesar) served as both reference and counter electrode. A fiber-glass separator was soaked with electrolyte (1 M $LiPF_6$ in 1:1 wt% ethylene carbonate /dimethyl carbonate, Novolyte). All electrochemical measurements were performed using a Biologic instrument (VMP3) at room temperature. The electrodes were cycled between 0.01 and 3 V vs Li/Li^+ under varying specific current rates. After the galvanostatic cycling, a potentiostatic limitation was added until the specific current reached 0.05C. 1C was defined as 300 mA/g through the text.

6.1.4 Results and Discussion

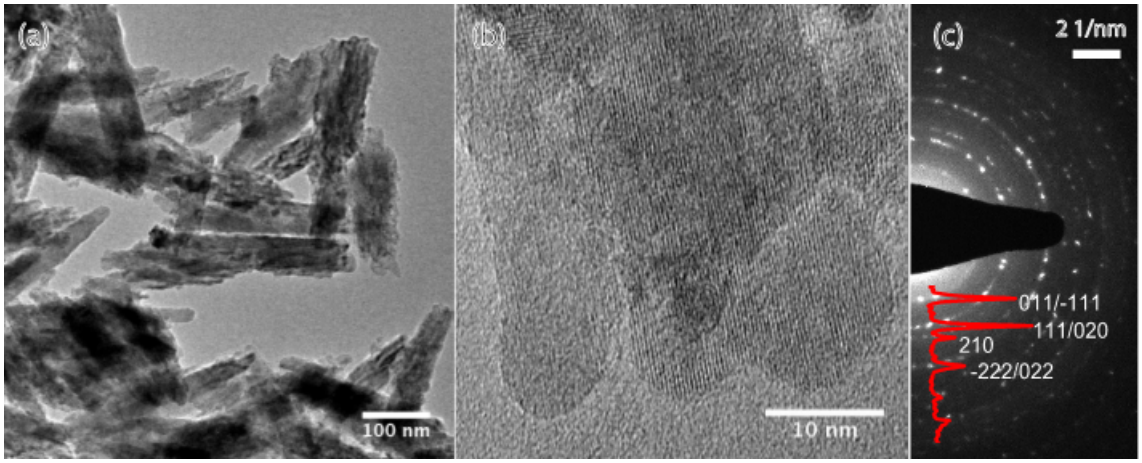

Figure 6.1: (a) , (b) HRTEM images and (c) SAED pattern of Ni:MoO_2 nanoparticles.

The Ni:MoO_2 nanoparticles adopt a rod-like shape as shown in Figure 6.1(a). Closer inspection in the High Resolution–Transmission Electron Microscopy (HR-TEM) image and selected area electron diffraction (SAED) pattern reveal their polycrystalline character and lack of preferential growth direction as shown in Figure 6.1(b-c). In fact the elongated structures are assemblies of nanoparticles between 10 and 20 nm similar to previously reported MoO_2. [20] Therefore we assume the doping does not significantly influence the morphology of nanoparticles. In addition, the EDX analysis [44] reveals that 1.9 ± 0.5 at% of Ni is incorporated in the molybdenum dioxide matrix as shown in SI Table 6.3.

Structure of the MoO_2 host lattice

The PXRD patterns of MoO_2 and Ni doped MoO_2 reveal that both samples exhibit the disordered rutile structure (monoclinic, space group $P2_1/c$) without detectable impurities. The PXRD patterns were further analyzed by the Rietveld method. The lattice parameters, average crystal size, doping level and Rietveld agreement factors for both samples are summarized in Table 6.1, and the fits of the profiles to the experimental data are shown in SI Figure 6.10. The detailed structure of Ni:MoO_2 is quite similar to that of MoO_2, i.e. the b, and the c lattice constants are slightly

smaller, whereas a slightly increases, and the average crystal size changes from 16.7 nm to 16.0 nm. Refinement of the atomic occupancy of Ni reveals that the doping level is 1.3 ± 0.8 at%, which is within the accuracy of the refinement method, and is comparable to the EDX result. Thus, we can conclude that the doping of nickel only slightly influences the crystal structure of MoO_2 host.

Table 6.1: Refinement Parameters, Lattice Parameters, Atomic Parameters and Crystal Size of MoO_2 and Ni:MoO_2

sample ID	lattice param. / Å	avg. crysal size / nm	doping level / at%	refinement param.
MoO_2		16.7		
	$a = 5.6251(1)$			$R_{wp} = 0.68$
	$b = 4.8628(1)$			
	$c = 5.6039(2)$			$\chi^2 = 8.85$
	$\beta = 120.714(2)$			
	$V = 131.813(2)$			
Ni:MoO_2		16.0	1.3(8)	
	$a = 5.6371(1)$			$R_{wp} = 0.68$
	$b = 4.8522(1)$			
	$c = 5.5982(1)$			$\chi^2 = 10.91$
	$\beta = 120.725(1)$			
	$V = 131.629(2)$			

This result is further supported by direct comparison of EXAFS spectra of MoO_2 and Ni:MoO_2 recorded at Mo K-edge as shown in Figure 6.2. The k^3 weighted Fourier Transform (FT) of the EXAFS spectra reveal that the main characteristics of Mo-O stay the same. The most remarkable change induced by Ni doping is the overall reduction of peak intensities, which implies an increasing disorder. [45] To obtain quantitative information on the local structure, we fit FT of the EXAFS function in the range of 1.083 to 2.881 Å using Artemis software. [46] Structural parameters obtained from the fit are given in SI in Table 6.4 and fitted FT spectra are shown as dashed lines in Figure 6.2. The lattice parameters refined from PXRD data of MoO_2 nanoparticles are used as the input parameters for the EXAFS fits of MoO_2 and Ni:MoO_2. The distances fitted with EXAFS are in good agreement with the refined PXRD data, within the error bars. For the Ni:MoO_2 the fitted bond length (R) values are slightly higher than for MoO_2, but also within the error bars almost no changes in the distance is observable. Moreover, the Debye-Waller (σ^2) factors for Ni:MoO_2 are higher than for MoO_2, which is in line with the aforementioned results of Rietveld refinement of PXRD and further confirms that Ni doping induces only slight disorder of the host MoO_2 lattice.

Structure and valence of Ni dopant

We investigate the valence of the nickel incorporated in the molybdenum dioxide

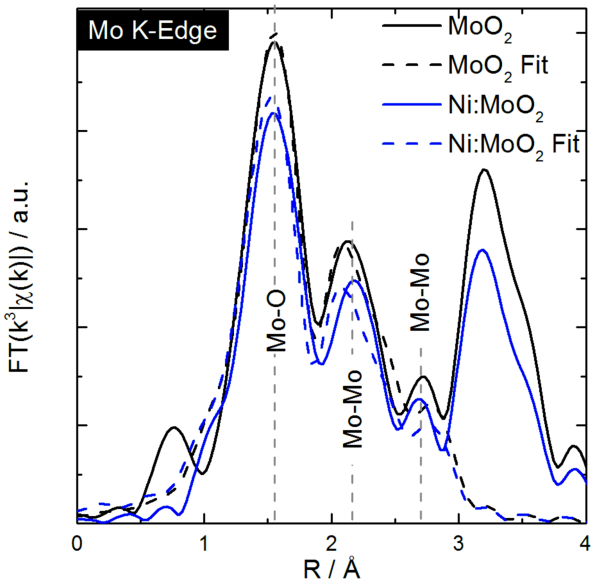

Figure 6.2: k^3 weighted FT of MoO_2 (black) and Ni:MoO_2 (blue) measured at the Mo K-edge plotted in the range $R = 0-4$ Å. The solid lines represent the measured data, and the dotted lines represent the corresponding fit results. Additionally, the first shells features are marked.

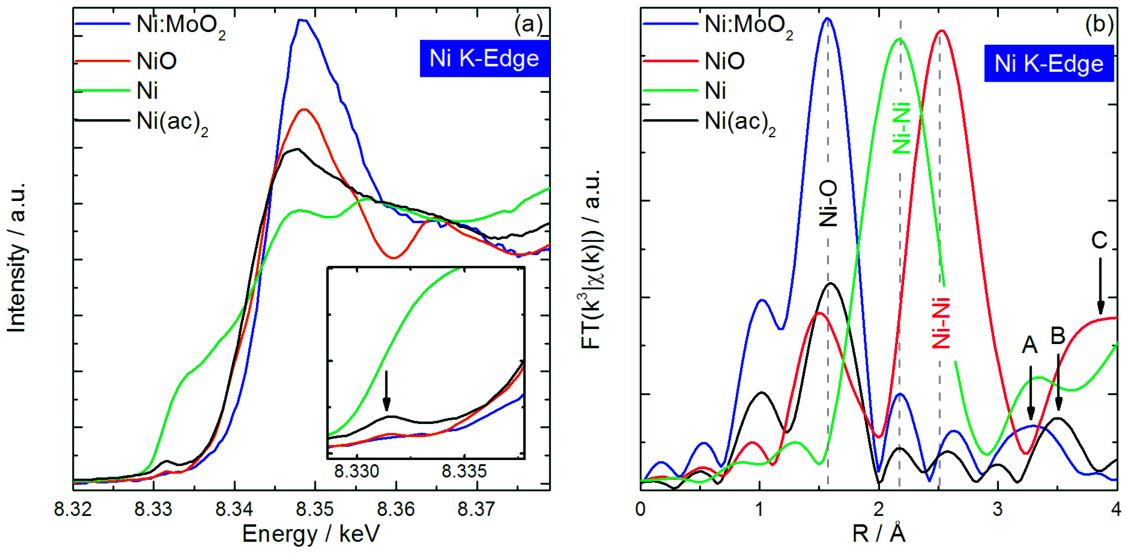

Figure 6.3: (a) XANES spectra at Ni K-edge and (b) corresponding k^3 weighted FT of EXAFS spectra of Ni:MoO_2 (blue curve), NiO (red curve), Ni-foil (green curve), and $Ni(ac)_2{\cdot}4\,H_2O$(black curve). In the inset, the arrow points at the pre-edge feature. The first-shell bonds and characteristic features of different compound (A, B, C) are indicated.

lattice by analyzing the XANES spectra recorded at the Ni K-edge of Ni:MoO_2

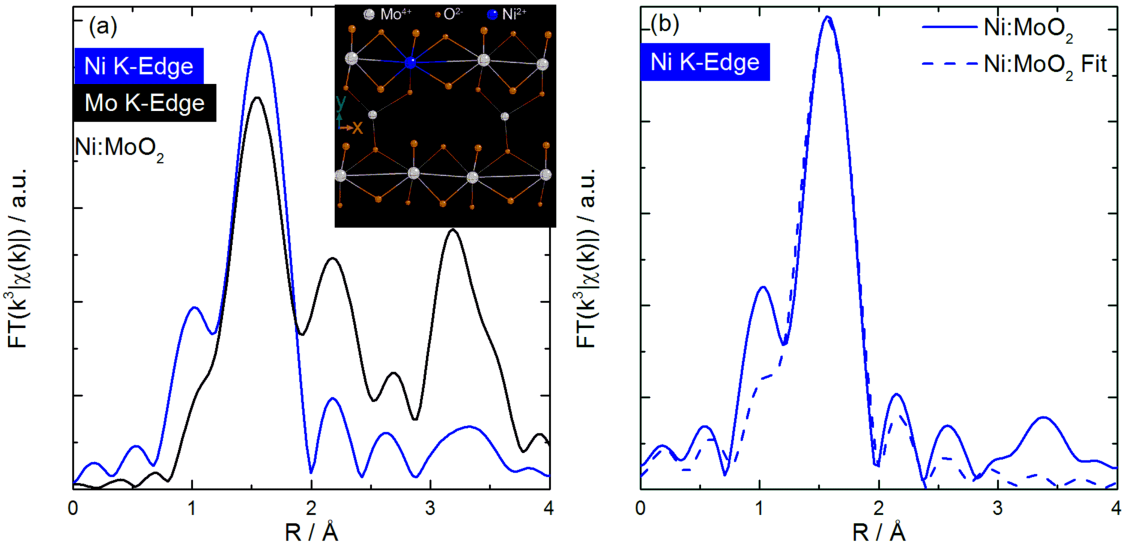

Figure 6.4: (a) FT k^3 weighted EXAFS spectra: Ni:MoO_2 measured at the Ni K-edge (blue curve) and at the Mo K-edge (black curve). (inset) Crystal structure of MoO_2 showing adjacent unit cells along the c axis, in which Ni ion (blue) substitute a Mo ion (gray). (b) k^3 weighted FT of EXAFS spectrum of Ni:MoO_2 (solid curve) measured on the Ni K-edge and its corresponding fit (dashed curve).

nanoparticles and reference compounds: nickel oxide (NiO), nickel (Ni) and nickel acetate ($Ni(ac)_2$) shown in Figure 6.3(a). Ni^0, Ni^{2+} and Ni^{3+} exhibit the absorption edge at 8.333 keV, 8.345 keV and 8.348 keV, respectively. [47–49] The position of the absorption K-edge in Ni:MoO_2 at 8.345 keV is identical to the position of the absorption edge of nickel(II) oxide (8.345 keV) [47] and slightly higher than of nickel(II) acetate (8.343 keV) suggesting that the nickel ion remains in the divalent oxidation state after incorporation into the molybdenum dioxide lattice. However, we cannot fully exclude traces of Ni^{3+}.
The Ni:MoO_2 absorption edge shifts of about 0.1 eV and 1.7 eV in respect to NiO and $Ni(ac)_2$. It is likely caused by different ligands bonding to Ni and different coordination numbers of Ni in these compounds. [50] These differences are clearly visible in the corresponding k^3-weighted Fourier Transform of the EXAFS spectra in Figure 6.3(b). For NiO, $Ni(ac)_2$ and Ni:MoO_2 we can determine a nickel-oxygen distance in the first shell at 1.50, 1.59 and 1.56 Å, respectively. [51] Additionally, for NiO we observe a strong Ni-Ni peak in the second coordination shell at 2.52 Å and for the metallic nickel the Ni-Ni distance in the first coordination shell is 2.18 Å. It is evident that Ni:MoO_2 neither resembles the cubic structure of NiO nor of Ni. However, the Ni:MoO_2 pattern shows many similarities with $Ni(ac)_2$ pattern and only the inspection of the features at radial distances higher than 3 Å allows to differentiate between them. The differences are denoted in Figure 6.3(b) by A and B. The aforementioned results suggest that divalent Ni is incorporated into the molybdenum dioxide host lattice. To address the position of Ni in the MoO_2 lattice we utilize the ATOMS and Artemis software. [52] In the unit cell of monoclinic

MoO_2 three different sites, one Mo-site and two O-sites, are present. We calculate the scattering paths for Ni in MoO_2 on those different positions and compare them with measured data. This analysis implies that nickel substitutes molybdenum in the lattice.
Furthermore, we fit the FT of the EXAFS spectrum recorded at Ni K-edge with a similar model used for the determination of the local structure around Mo ion from FT of the EXAFS spectrum recorded at Mo K-edge (see discussion above). We include in the fit only the oxygen shell since the presence of higher Ni-metal shells result in very large errors, due to the low intensity of higher shell signal. This implies a local disorder around the Ni ions in the Ni-metal shells. Nevertheless, the FTs of Ni:MoO_2 at the Ni K-edge and MoO_2 at Mo K-edge show good resemblance and therefore confirm the substitution of Mo with Ni in the lattice as shown in Figure 6.4(a). To this end, we assume that the 2 at% Ni are evenly dispersed in the MoO_2 matrix and thus, in the direct vicinity of one Ni ion there are no other Ni ions. The results of the fit point to an increase in the distances of the nearest neighbors of nickel in comparison to molybdenum as shown in Figure 6.4 and SI Table 6.4. The metal ion – oxygen bond is 1.990 and 1.983 Å for Mo^{4+} ion in MoO_2 and Ni:MoO_2 and 2.012 Å for Ni^{2+} in Ni:MoO_2. This change is possibly induced by increasing ionic radius of the metal in a six-fold coordination from 0.79 for Mo^{4+} to 0.83 Å for Ni^{2+}. The reported values for Ni-O distance of tetra-, tri- and divalent Ni ions are 1.88, 1.91 and 2.06 Å, respectively and are pointing towards divalent Ni. [53] However, due to the fit errors we cannot exclude the presence of traces of Ni^{3+} ions. Furthermore, the Debye-Waller factor of Ni in Ni:MoO_2 is higher than of Mo in Ni:MoO_2, which reflects an increase in local disorder. [46]
However, in order to rationalize the shrinkage of the overall volume of the unit cell of Ni:MoO_2 recovered by Rietveld refinement local structure relaxations must be involved. In a disordered rutile structure of MoO_2, each tetravalent Mo ion is surrounded octahedrally by six O ions. When one divalent Ni ion substitutes one Mo ion, we assume nearby the Ni ion there are two Mo^{5+} ions, or one Mo^{6+} ion or oxygen vacancies exist to compensate the charges. Therefore, despite that the ionic radius of Ni^{2+} is larger than that of Mo^{4+} the overall volume of the unit cell for Ni:MoO_2 slightly decreases. [54] An alternative explanation for the observed shrinking of the lattice parameter is the presence of six-fold coordinated, trivalent Ni ions, which have a smaller ionic radius (0.7 - 0.74 Å) than the host Mo^{4+} ions.

Doping mechanism

There are several scenarios for doping or formation of ternary and quaternary compounds in non-aqueous solution. For example, in supercritical conditions $LiFePO_4$ nanoparticles nucleate directly from the solution, [55,56] whereas in the microwave-assisted reaction, lithium phosphate particles and amorphous spherical nanoparticles nucleate first and then undergo a solid–solid reaction to $LiFePO_4$. [57] Thus, to pin down on the time scale the incorporation of Ni into the MoO_2 lattice we alternatively measure EXAFS spectra at Ni and Mo K-edges during the reaction. The spectra recorded *in-situ* at Ni K-edge are significantly noisier than the spectra of reference powders as shown in SI in Figure 6.11. Therefore, it is not possible to

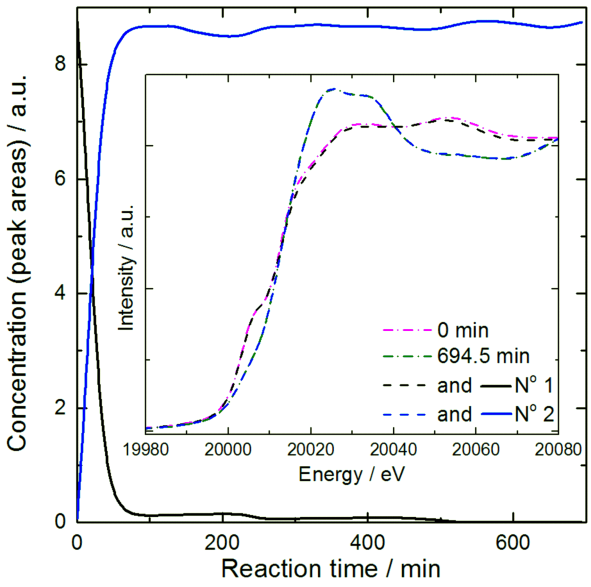

Figure 6.5: Interdependence between two components recovered by MCR-ALS from XAS data recorded *in-situ* at Mo K-edge. Inset shows XAS spectra taken at room temperature at thebeginning (0 min, MoO_2Cl_2, pink curve) and at the end (694.5 min, MoO_2, green curve) of the reaction. Spectra of individual components recovered by MCR-ALS analysis (black and blue curves) are almost identical with MoO_2Cl_2 and MoO_2.

track the changes related to the variation of Ni-O bond. Nevertheless, we observe no changes of the edge and thus conclude that Ni stays divalent during the course of the synthesis. Furthermore, we investigate the Mo K-edge spectra and observe, similar to the synthesis of MoO_2, the disappearance of the pre-edge feature. This indicates the reduction of Mo^{6+} to Mo^{4+} as shown in SI Figure 6.12. We analyze the Mo XANES spectra with Multivariate Curve Resolution (MCR-ALS) by fitting them with two components as shown in Figure 6.5 and in SI Figure 6.8 and 6.12 and Table 6.2. Since two components are sufficient to fit the data we hypothesize that Ni:MoO_2 directly nucleates in the final composition. Here, component 1 represents the dissolved MoO_2Cl_2 precursor, whereas component 2 is steadily forming right at the beginning of the synthesis and represents the final compound. After 82 minutes the entire component 1 converts to component 2. No further component, even after 10 hours is observed, which excludes the successive incorporation of Ni into the MoO_2 lattice. Thus, within the temporal resolution of our *in-situ* X-ray Absorption Spectroscopy (XAS) experiments, we can conclude that the final ternary compound Ni:MoO_2 (component 2) nucleates directly from the solution, similar to the nucleation of $LiFePO_4$ in supercritical conditions. [55, 56]

Electrochemical cycling (EC)

To explore the potential of Ni:MoO_2 as anode material for lithium-ion batteries we measure cyclic voltammetry (CV) and galvanostatic cycling with potential limitation

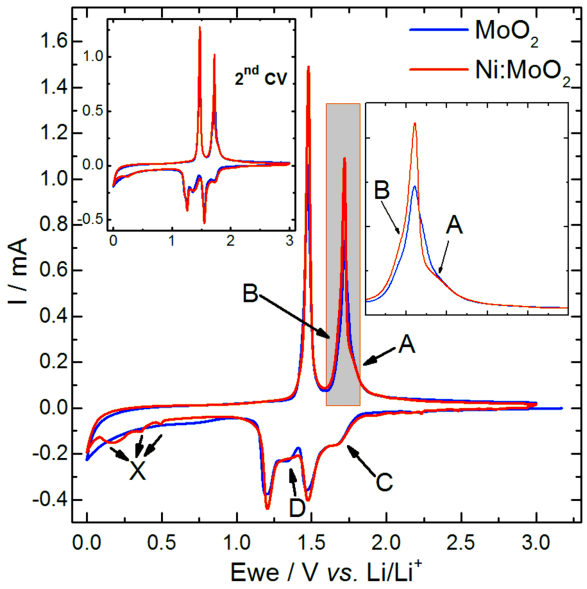

Figure 6.6: First and second cyclic voltammograms of MoO_2 and Ni:MoO_2 at a scan rate of $0.1\,mV\,s^{-1}$ in the voltage range $0.01 - 3\,V$.

(GCPL) at different current rates. We compare the CV curve of the Ni:MoO_2 electrode cycled at a scan rate of $0.1\,mV\,s^{-1}$ with the CV curve of MoO_2 in Figure 6.6. The CV profile of Ni:MoO_2 is basically like that of MoO_2, i.e., both anodes show the appearance of the redox pairs ascribed to the monoclinic–orthorhombic–monoclinic phase transitions of MoO_2 The pronounced reduction peaks in the first CV curves of both MoO_2- and Ni:MoO_2-based anodes suggest that the nanoparticles maintain their high crystallinity after the carbon coating process. This is further confirmed by *in-situ* PXRD, which indicates no changes of phase or crystallinity up to a temperature of 700 °C in inert atmosphere as shown in Figure 6.9 in SI. According to the second CV cycle at $0.1\,mV\,s^{-1}$, both MoO_2 and Ni:MoO_2 display highly reversible cycling behavior, even at scan rates up to $25\,mV\,s^{-1}$ as shown in Figure 6.13. From the CV profiles, we conclude that there is no observable difference in charging/discharging mechanism of MoO_2 and Ni:MoO_2. For further discussion on the CV profiles please refer to SI and references. [22, 23, 58–61] Surprisingly, the GCPL curves of MoO_2 and Ni:MoO_2–based anodes strongly differ as shown in Figure 6.7. In the following, we elucidate the details of GCPL at different current rates with a potentiostatic step until the specific current reaches 0.05C. For MoO_2–based anode, the first cycle at 0.1C displays two short discharge plateaus at 1.57 and 1.29 V, approximately, with a final specific discharge of 370 mAh/g; on charge two plateaus at about 1.69 and 1.40 V appear with a total capacity of 190 mAh/g. Thus, the batteries initial Coulombic efficiency is 51.5 %, which is ascribed to the irreversible generation of solid electrolyte interphase (SEI) on the electrode surface as shown in Figure 6.7(c). On the second discharge, MoO_2-based anode shows almost the same plateaus but with much less capacity of 229 mAh/g. The second charging curve resembles the first one but with slightly higher capacity of 198 mAh/g. Overall, the

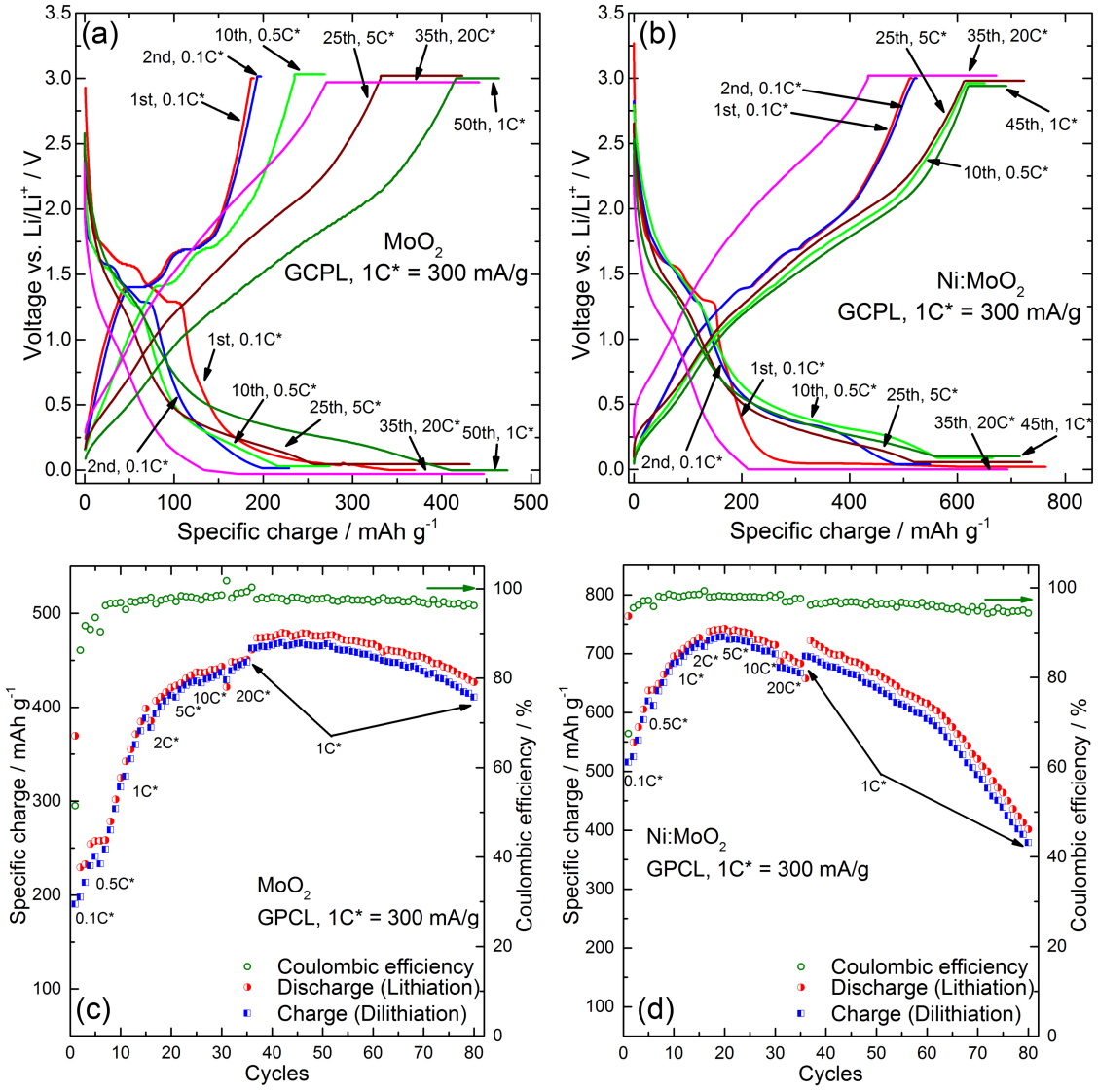

Figure 6.7: GCPL curves of MoO_2 (a) and Ni:MoO_2 (b) at current rates up to 20 C, with a potentiostatic step until the specific current reached 0.05 C*, where 1 C* = 300 mA g^{-1}. We added * to point out the potentiostatic step. (Note: the potentiostatic steps were manually shifted to avoid overlap among different lines). Specific charge, discharge and Coulombic efficiency for MoO_2 (c) and Ni:MoO_2 (d).

Coulombic efficiency is enhanced to 86.3 %. After 5 cycles at 0.1C, the current is increased to 0.5C. The plateaus are shorter than those at 0.1C, but the anode delivers even higher discharge and charge capacities of 258 and 249 mAh/g, respectively that brings the Coulombic efficiency to 96.7 %. The MoO_2-based anode is further cycled at 1C, 2C and 5C for 5 times each. At 5C, its phase-transition plateaus almost disappear. Surprisingly, the anode uptakes and removes more lithium ions with dis /charge capacity of 425/419 mAh/g, respectively. At 20C, galvanostatic dis /charge capacity is much lower; however, with the potentiostatic charging, it still

can be fully discharged (448 mAh/g) or charged (443 mAh/g). After these increasing current rates, MoO_2 was cycled back at 1C. In comparison to initial cycle at lower current rates, the plateaus totally vanish. The capacity of MoO_2-based anode first gradually increases and after dozens of cycles slightly decreases.
For the Ni:MoO_2–based anodes the first cycle of the GCPL curves at 0.1C shows identical discharge and charge plateaus like for MoO_2–based anodes as shown in Figure 6.7(a-b). At the same time, the capacity of Ni:MoO_2 in comparison with MoO_2 is roughly doubled as shown in Figure 6.7(c-d). For discharge, the capacity increases from 370 for MoO_2 to 764 mAh/g for Ni:MoO_2 and for charge from 290 for MoO_2 to 515 mAh/g for Ni:MoO_2. This gives an initial Coulombic efficiency of 67.4 % for Ni:MoO_2, which is almost 15 % higher than that of MoO_2. After initial cycles, the SEI stabilizes, thus the Coulombic efficiency is promoted to ∼96 % from 2nd cycles. It is evident that the EC behavior of Ni:MoO_2 is qualitatively similar to MoO_2, but quantitatively it offers much higher specific charge for each cycle. At 0.5C, Ni:MoO_2 displays reversible lithium storage capacities of 648 mAh/g and 636 mAh/g for discharge and charge, respectively. At 5C, even higher reversible capacities are achieved for discharge and charge, 740 mAh/g and 725 mAh/g, respectively. After about 30 cycles, it still presents 698 mAh/g for lithium uptake and 676 mAh/g for lithium removal at 20C. Ni:MoO_2 is able to deliver higher capacities, but it slowly degrades to reach after in total 80 cycles the capacity of MoO_2.
Interesting, we observe for MoO_2 and Ni:MoO_2 based anodes an atypical increase of the capacity upon initial increase of charging rate and cycling. A similar activation phenomenon has been observed before for the nanostructured MoO_2. [58, 59] The mechanism was assigned to gradual pulverization of nanoparticles, followed by a partial lose of the crystallinity or even transformation to an amorphous-like structure. However, loosing of crystallinity of MoO_2 nanoparticles was also reported to be responsible for the opposite effect, namely for the capacity fading upon cycling. ([20] and references therein) An alternative explanation for the activation upon cycling is storage of Li via interfacial charging. [62] In summary, a generally valid mechanism for the activation phenomenon does not exist so far. In our case, this phenomenon is observed for both MoO_2 and Ni:MoO_2 based anodes, which rule out the role of Ni. We also presume the activation phenomenon is rather independent on the structural changes of nanoparticles but rather related to the applied cycling procedure. This hypothesis can be only adequately validated by *in-situ* studies during cycling.

Discussion on the role of Ni in electrochemical cycling
Although studying the exact role of Ni in MoO_2 on the EC performance exceeds the scope of this paper, we can draw two plausible scenarios. The reason for the improved EC properties of Ni:MoO_2 may originate either from structural or electronic modification of the MoO_2 lattice, or from the combination thereof.
In general, the difference of the work function of an anode (Φ_a) and a cathode (Φ_c) determines the open circuit voltage (V_{OC}) and thereby the maximum power output of the batteries. So far, it has been shown that coating with conductive carbon or doping with SiO_2 may induce significant changes of the work function of MoO_2. [29, 63] Here, we measure V_{OC} of 3.21 and 3.27 V for MoO_2- and Ni:MoO_2-

based anode, respectively. Assuming the work function of the cathode equals 2.4 eV eV, [64] which is the theoretical value for the work function of Li, we determine the work function of MoO_2 and Ni:MoO_2 to be 5.61 and 5.68 eV, respectively. Taking into account that the thermal energy (kT) at room temperature is of the same order, 0.03 eV, as the work function difference, 0.06 eV, we assume that the work function of Ni:MoO_2 does not significantly change with respect to MoO_2. Therefore, we have to consider another justification for the enhanced EC properties.
An alternative, and more plausible explanation of the role of Ni on the EC properties of Ni:MoO_2-based anode gives a structural model. To estimate the impact of structural modification, we first provide a description of the lithiation process. Upon lithiation, MoO_2 first undergoes one-electron addition-type reaction:

$$MoO_2 + xLi^+ + xe^- \longrightarrow Li_xMoO_2, \tag{6.1}$$

in which x is close to one and the theoretical capacity is ∼209 mAh/g. This initial reaction is followed by three-electron conversion-type reaction:

$$Li_xMoO_2 + yLi^+ + ye^- \longrightarrow 2\,Li_2O + Mo, \tag{6.2}$$

in which $x + y = 4$. Together with for the four-electron reaction, the theoretical capacity is calculated as 806 mAh/g. However, the latter conversion stage requires a heterogeneous charge transfer at the interfaces, Li^+ and O^{2-} diffusion in solid state, and Mo–O bond cleavage. [65] To overcome the energy barrier for the processes described in Eq. (6.2) a certain activation energy is needed. MoO_2 is typically thermo-electrochemically activated at 85 °C. However, also reduced sizes of particles and additional structural defects are known for facilitating the conversion-type reaction. For example, Ku et al showed that the onset temperature for the thermo-electrochemical activation decreases from 85 °C to 55 °C due to enlargement of surface area and introduction of defect sites by ball milling. [65]
In the case of Ni:MoO_2, we observe that the substitution of tetravalent Mo by divalent Ni leads to local lattice modification. Therefore, it is plausible that the lattice modification induced by Ni promotes the lithium mobility and enhances the kinetics of the conversion reaction. Accordingly, anodes based on Ni:MoO_2 nanoparticles provide much higher initial capacities than those based on MoO_2.

6.1.5 Conclusions

Here, we present a straightforward doping route for the incorporation of divalent Ni in the lattice of metallic MoO_2. Careful X-ray diffraction and absorption studies reveal the valence, position and concentration of Ni in the MoO_2 lattice. Despite of the divalent state of Ni substituting tetravalent Mo, we observed only slight shrinkage of the host lattice. Additionally, we indirectly determine that the work function of Ni:MoO_2 does not significantly differ from MoO_2. However, to further elucidate the influence of Ni on the electronic structure of MoO_2 and dedicated experiments, for example High Energy Resolution Fluorescence Detection (HERFD) XAS and X-ray

emission spectroscopy (XES), are needed. [66] Clearly, for a technological application of MoO_2-based anodes, many issues remain to be solved. However, our results indicate that doping is a simple tool to significantly improve the EC properties. Moreover, it can be expected that in the future possible applications of Ni:MoO_2 can be extended to other types of electrodes.

6.1.6 Acknowledgements

This work was supported by the Swiss National Science Foundation (SNSF) (Nos. 200021_124632 and 200021_1373637) and ETH Zurich (No. ETH-2813-1). We thank the Scientific Center for Optical and Electron Microscopy SCOPEM for access to the electron microscope facility and European Research Synchrotron Facility in France for beam-time allocation.

6.1.7 Supporting Information

MCR-ALS analysis

The description of MCR-ALS method can be found elsewhere. [31, 39, 40] The following values were calculated by MCR-ALS algorithm: lack of fit (Eq. 6.3), the variance explained (Eq. 6.4) and the standard deviations of residuals in respect to the experimental data (Eq. 6.5) are shown in Table 6.2.

$$lof[\%] = 100\sqrt{\frac{\sum_{i,j} e_{i,j}^2}{\sum_{i,j} d_{i,j}^2}}, \tag{6.3}$$

$$R^2 = \frac{\sum_{i,j} d_{i,j}^2 - \sum_{i,j} e_{i,j}^2}{\sum_{i,j} d_{i,j}^2}, \tag{6.4}$$

$$\sigma = \sqrt{\frac{\sum_{i,j} e_{i,j}^2}{n_{rows} n_{columns}}}, \tag{6.5}$$

where d_{ij} is an element of the input data matrix D, e_{ij} is the related residual obtained from the difference between the input element and the MCR-ALS optimization results, n_{rows} and $n_{columns}$ are the number of rows and columns in the D matrix. MCR-ALS method calculates two different lack of fit values, that differing on the definition of the input data matrix D. Either the raw experimental data matrix or the PCA reproduced data matrix with the same constrains are used.

Table 6.2: The parameters obtained from the MCR-ALS analysis of the *in-situ* XANES data.

lof_{ALS}	0.7979 %
lof_{PCA}	0.307 53 %
R^2	99.9936
σ	0.0062392

Determination of the number of components.

We choose the number of components on the basis of SVD as shown in Figure 6.8. We plot eigenvectors representation of the first three components. The third component, due to its irregular fashion of the third eigenvector representation, is assumed to be noise. Therefore, we choose two components as sufficient to explain enough variance in the data.

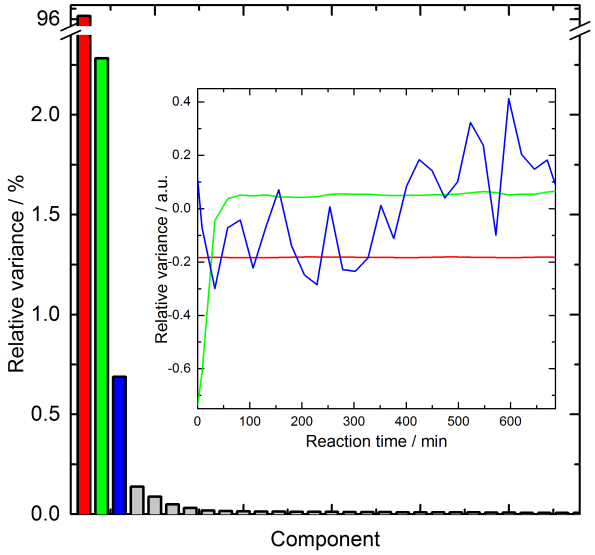

Figure 6.8: Visualization of the SVD of the *in-situ* spectra recorded at the Mo K - edge. Colors: red, green and blue represents the values related to first, second and third component. a) Eigenvalues in a relative variance plot. The first two eigenvalue accounts for 98.77 % of the variance (first eigenvalue: 96.49 %, second singular value: 2.28 %). Inset: the eigenvectors representation of the first, second and third component.

EDX Data

Table 6.3: EDX statistics on Ni:MoO_2 samples

Spectrum	At % Ni	At % Mo
1	1.8	98.2
2	2.2	97.8
3	1.9	98.1
4	1.9	98.1
5	2.0	98.0
	1.9 ± 0.5	98.1 ± 0.5

In-situ XRD measurements during carbon coating

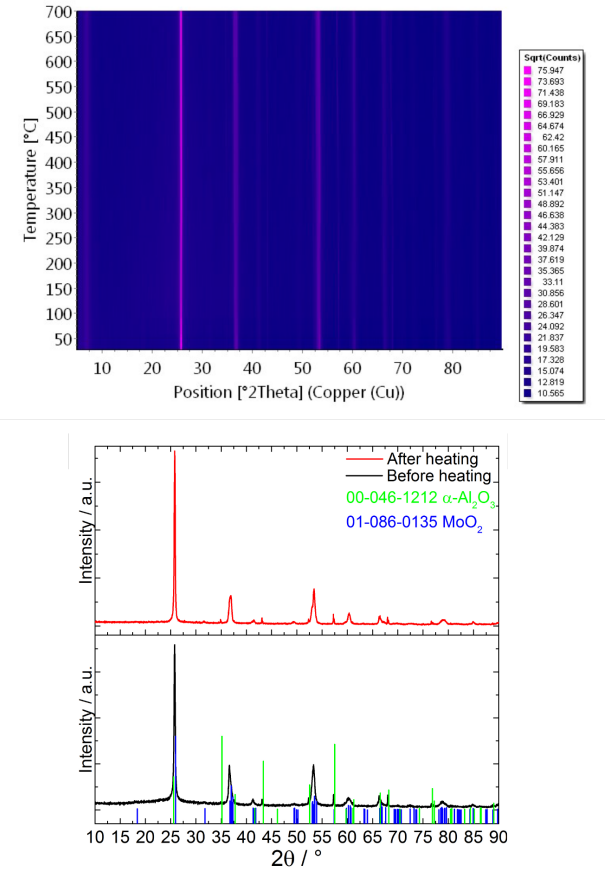

Figure 6.9: (top) Temperature map of diffraction patterns taken *in-situ* during carbon coating of Ni:MoO_2 nanoparticles under N_2. (bottom) PXRD pattern of MoO_2 before (red) and after (black) carbon coating and reference patterns of MoO_2 (blue) and alumina substrate (green). No new diffraction peaks are visible even at 700 °C. Thus, we conclude that neither phase transition of monoclinic MoO_2 nor separations of nickel phase are observed.

Rietveld refinement

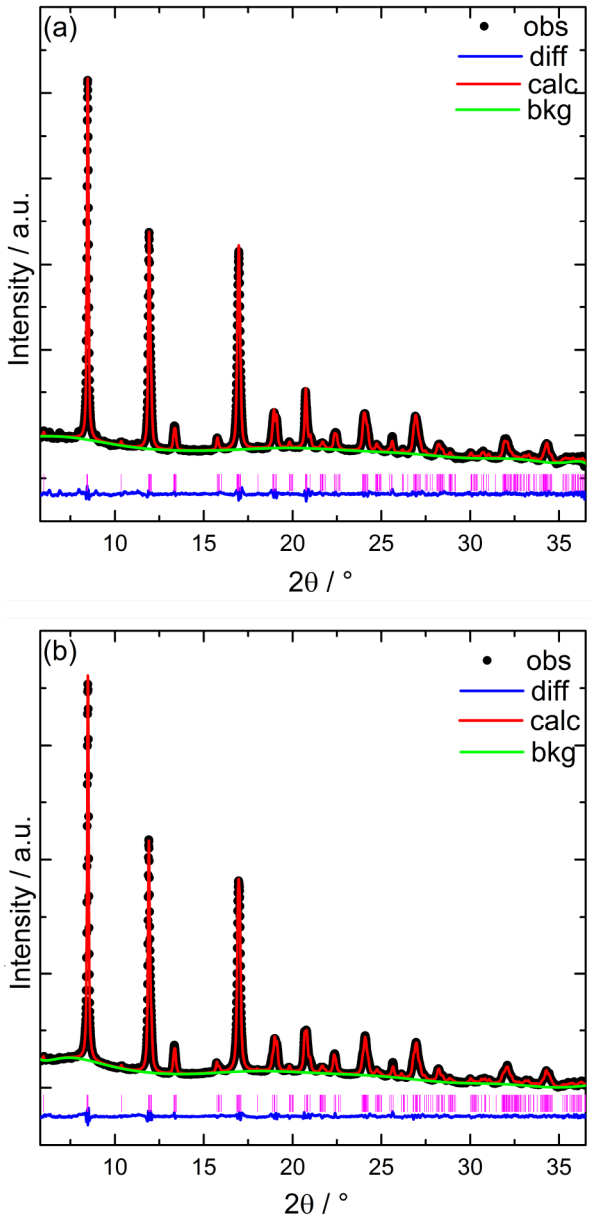

Figure 6.10: XRD data measured using a wavelength of 0.5054 Å and Rietveld refined data for (a) MoO_2 and (b) Ni:MoO_2 .

EXAFS fit

The amplitude factor S_0^2 is fitted for MoO_2 and also used for Ni:MoO_2 at Mo K-edge. On the Ni K-edge the amplitude factor of NiO is fitted and used for Ni:MoO_2. R stands for the fitted bond length and R_0 for the theoretical one calculated from the Rietveld refined data for pure MoO_2. The energy shift is E_0 and fitted for all three compounds seperately. N is the coordination number and fixed during the fit and σ^2 is the Debye-Waller factor. The Mo-shell cannot be fitted adequately in Ni:MoO_2 at the Ni $K-$edge and is therefore left out of the fit. The reason lies in the high disorder in the Mo atoms around each Ni atom.

Table 6.4: EXAFS fitted parameter for MoO_2 and Ni:MoO_2 measured at Mo and Ni K-edges

Sample ID	Atom	N	σ^2 / Å^2	R / Å	R_0 / Å
MoO_2 at the Mo K-edge	O11	4	0.0018 ± 0.0004	1.990 ± 0.012	1.983
$S_0^2 = 0.778 \pm 0.161$	O12	2	0.0018 ± 0.0004	2.078 ± 0.012	2.071
$E_0 = 0.962 \pm 1.402$	Mo11	1	0.0016 ± 0.0004	2.539 ± 0.015	2.518
$R = 0.011$	Mo12	1	0.0042 ± 0.0015	3.162 ± 0.019	3.118
Ni:MoO_2 at the Mo K-edge	O11	4	0.0026 ± 0.0006	1.983 ± 0.018	1.983
$S_0^2 = 0.778 \pm 0.161$	O12	2	0.0026 ± 0.0006	2.072 ± 0.018	2.071
$E_0 = -2.100 \pm 2.066$	Mo11	1	0.0024 ± 0.0006	2.542 ± 0.022	2.518
$R = 0.033$	Mo12	1	0.0054 ± 0.0026	3.157 ± 0.028	3.118
Ni:MoO_2 at the Ni K-edge	O11	4	0.0035 ± 0.0120	2.012 ± 0.178	1.983
$S_0^2 = 0.901 \pm 0.096$	O12	2	0.0035 ± 0.0120	2.101 ± 0.186	2.071
$E_0 = -0.998 \pm 29.647$	Mo11	1	–	–	2.518
$R = 0.012$	Mo12	1	–	–	3.118

X-ray absorption data

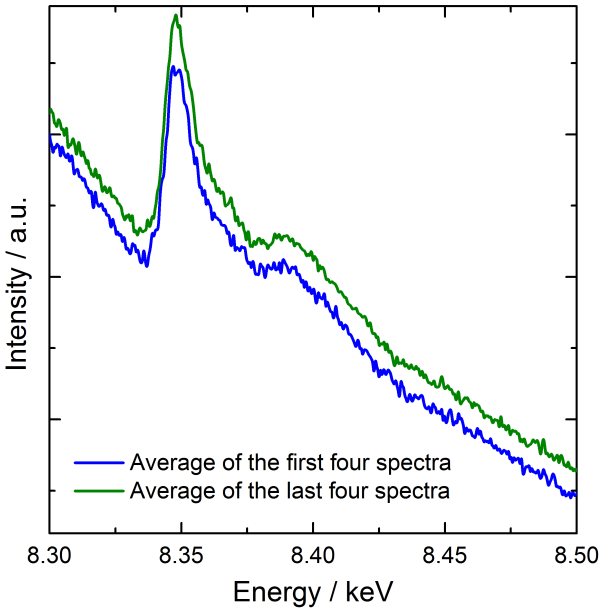

Figure 6.11: Spectra recorded *in-situ* at Ni K-edge at the beginning (blue curve) and the end of the reaction (green curve). The molar concentration of Ni in the solution was low (0.0050 M) and thus the single spectra are rather noisy. Here an average spectrum out of 4 is shown.

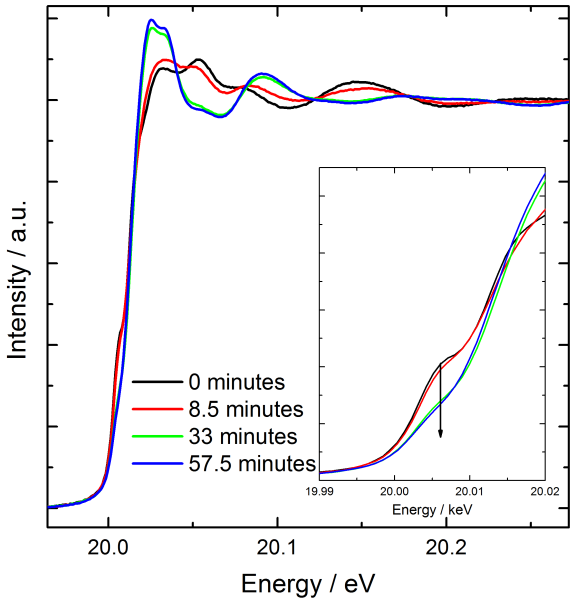

Figure 6.12: XAS spectra recorded at Mo K-edge during first 74 minutes of reaction at 215 °C.

Supplementary discussion on CV profile (Figure 6.6 and 6.7 in the main text and 6.13)

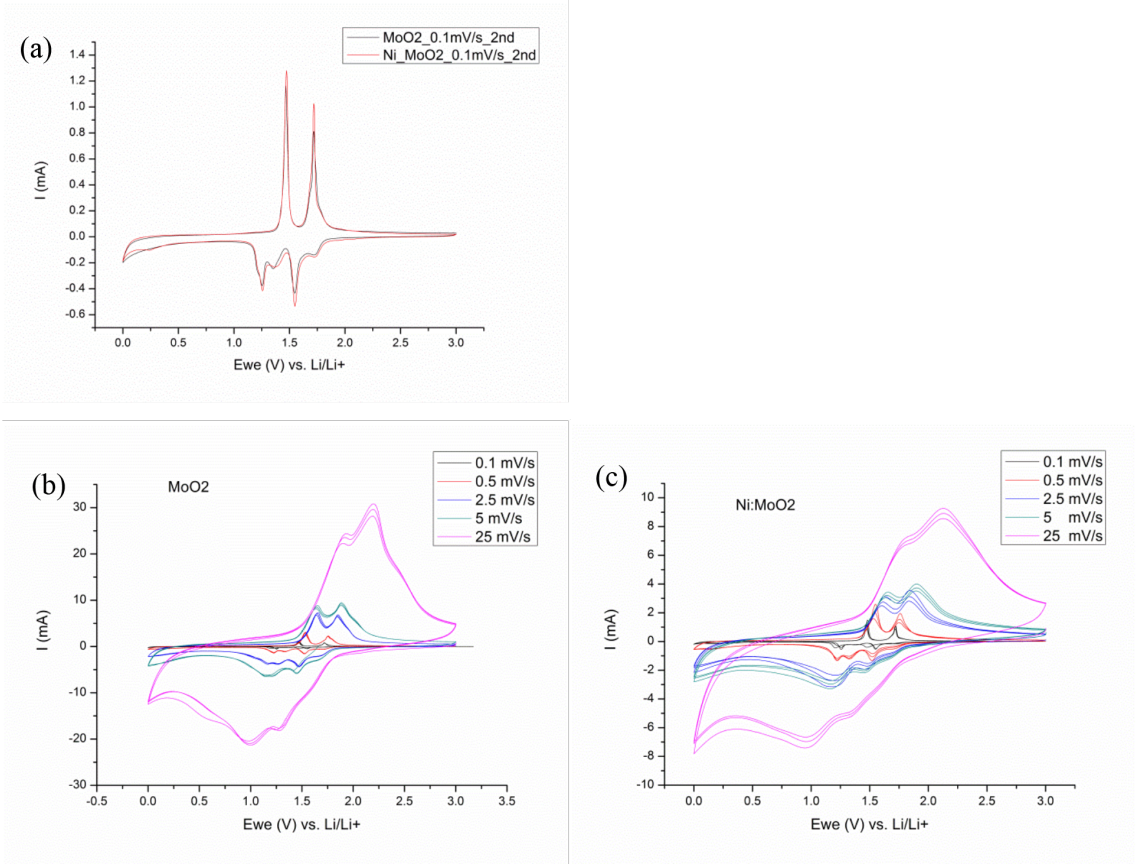

Figure 6.13: The second cyclic voltammograms of MoO_2 and Ni:MoO_2 at a scan rate of $0.1\,mV\,s^{-1}$ in the voltage range of 0.01 V to 3 V (a). Cyclic voltammograms of MoO_2 (b) and Ni:MoO_2 (c) at scan rates up to $25\,mV\,s^{-1}$ in the voltage range of 0.01 V to 3 V.

The CV profile of Ni:MoO_2 is basically alike that of MoO_2, besides additional, tiny bumps at potential range below 0.6 V marked with arrows Figure 6.6 and 6.13. These bumps almost vanish in the following cycles suggesting the formation of the solid electrolyte interphase (SEI). MoO_2 in general show initially weak redox peaks. Here, carbon-coated MoO_2 starting from the first CV curve shows two pronounced reduction peaks (lithiation) at 1.48 V and 1.20 V. [22, 23, 58–60] Correspondingly on the oxidation part (delithiation), two significant peaks appear at 1.72 V and 1.47 V, respectively. On the second scan at $0.1\,mV\,s^{-1}$, the redox peaks slightly shifted to 1.55/1.26 V and 1.72/1.57 V respectively. The appearance of redox pairs can be ascribed to the monoclinic–orthorhombic–monoclinic phase transitions as suggested by Dahn and McKinnon. [61]
For the Ni:MoO_2 nanocrystals, there are no additional redox peaks in comparison with pristine MoO_2 after the first CV cycle, it further proves there is no phase

separation upon Ni-doping. Besides, two small shoulders located at 1.68/1.33 V on lithiation and 1.68/1.78 V on delithiation are sometimes observed, as marked C, D, B and A in Figure 6.6 in the main text. [23, 65] However, so far no explanation on their origin is available. After the second CV cycle at 0.1 mV s^{-1}, both MoO_2 and Ni:MoO_2 display highly reversible cycling behavior, even at scan rate up to 25 mV s^{-1} shown in SI, Figure 6.13a-c. This excellent reversibility can be assigned to the high crystallinity of MoO_2 after carbon coating. We conclude that from CV profile there is no observable difference in charging/discharging mechanism.

Bibliography

[1] B. O. Skadtchenko, M. Trudeau, C. W. Kwon, B. Dunn, and D. Antonelli. *Chem. Mater.* (2004), **16**, 2886–2894.

[2] R. L. Brutchey, G. S. Cheng, Q. Gu, and D. E. Morse. *Adv. Mater.* (2008), **20**, 1029–1033.

[3] Y. D. Wang, T. Brezesinski, M. Antonietti, and B. Smarsly. *ACS Nano* (2009), **3**, 1373–1378.

[4] L. Luo, D. Bozyigit, V. Wood, and M. Niederberger. *Chem. Mater.* (2013), **25**, 4901–4907.

[5] B. R. Matis, J. S. Burgess, F. A. Bulat, A. L. Friedman, B. H. Houston, and J. W. Baldwin. *ACS Nano* (2012), **6**, 17–22.

[6] S. C. Erwin, L. J. Zu, M. I. Haftel, A. L. Efros, T. A. Kennedy, and D. J. Norris. *Nature* (2005), **436**, 91–94.

[7] A. Sahu, M. S. Kang, A. Kompch, C. Notthoff, A. W. Wills, D. Deng, M. Winterer, C. D. Frisbie, and D. J. Norris. *Nano Lett.* (2012), **12**, 2587–2594.

[8] B. Ehrler, K. P. Musselman, M. L. Böhm, F. S. F. Morgenstern, Y. Vaynzof, B. J. Walker, J. L. MacManus-Driscoll, and N. C. Greenham. *ACS Nano* (2013), **7**, 4210–4220.

[9] P. Gopal and N. A. Spaldin. *Phys. Rev. B* (2006), **74**, 094418.

[10] I. Bilecka, L. Luo, I. Djerdj, M. D. Rossell, M. Jagodič, Z. Jagličič, Y. Masubuchi, S. Kikkawa, and M. Niederberger. *J. Phys. Chem. C* (2011), **115**, 1484–1495.

[11] G. Clavel, M. G. Willinger, D. Zitoun, and N. Pinna. *Adv. Funct. Mater.* (2007), **17**, 3159–3169.

[12] N. Lock, E. M. L. Jensen, J. L. Mi, A. Mamakhel, K. Noren, Q. B. Meng, and B. B. Iversen. *Dalton Trans.* (2013), **42**, 9555–9564.

[13] D. G. Stroppa, L. A. Montoro, A. Campello, L. Gracia, A. Beltran, J. Andres, E. R. Leite, and A. J. Ramirez. *Phys. Chem. Chem. Phys.* (2014), **16**, 1089–1094.

[14] J. R. Scheffe, R. Jacot, G. R. Patzke, and A. Steinfeld. *J. Phys. Chem. C* (2013), **117**, 24104–24114.

[15] A. Lauria, I. Villa, M. Fasoli, M. Niederberger, and A. Vedda. *ACS Nano* (2013), **7**, 7041–7052.

[16] J. F. Shackelford. *Introduction to Materials Science for Engineers*, pages 559 – 561. Prentice Hall, Upper Saddle River, New Jersey, 5 edition (2000).

[17] P. Ranade, Y.-C. Yeo, Q. Lu, H. Takeuchi, T.-J. King, and C. Hu. *MRS Proceedings* (2000), **611**, C3.2.1.

[18] M. Iwase, T. Kanazawa, and T. Mori. *Solid State Ionics* (1981), **2**, 331–336.

[19] Y. G. Liang, S. J. Yang, Z. H. Yi, X. F. Lei, J. T. Sun, and Y. H. Zhou. *Mater. Sci. Eng., B* (2005), **121**, 152–155.

[20] D. Koziej, M. D. Rossell, B. Ludi, A. Hintennach, P. Novak, J. D. Grunwaldt, and M. Niederberger. *Small* (2011), **7**, 377–387.

[21] B. Liu, X. Y. Zhao, Y. Tian, D. Zhao, C. W. Hu, and M. H. Cao. *Phys. Chem. Chem. Phys.* (2013), **15**, 8831–8837.

[22] Y. Sun, X. Hu, W. Luo, and Y. Huang. *J. Mater. Chem.* (2012), **22**, 425–431.

[23] Y. M. Sun, X. L. Hu, J. C. Yu, Q. Li, W. Luo, L. X. Yuan, W. X. Zhang, and Y. H. Huang. *Energy Environ. Sci.* (2011), **4**, 2870–2877.

[24] L. Zhou, H. B. Wu, Z. Y. Wang, and X. W. Lou. *ACS Appl. Mater. Interfaces* (2011), **3**, 4853–4857.

[25] Y. Zhou, I. Lee, C. W. Lee, H. S. Park, H. Son, and S. Yoon. *Bull. Korean Chem. Soc.* (2014), **35**, 257–260.

[26] X. P. Fang, B. K. Guo, Y. F. Shi, B. Li, C. X. Hua, C. H. Yao, Y. C. Zhang, Y. S. Hu, Z. X. Wang, G. D. Stucky, and L. Q. Chen. *Nanoscale* (2012), **4**, 1541–1544.

[27] K. T. Jacob, C. Shekhar, and Y. Waseda. *J. Am. Chem. Soc.* (2008), **91**, 563–568.

[28] L. Ben-Dor and Y. Shimony. *Mater. Res. Bull.* (1974), **9**, 837–844.

[29] B. Akkisetty, M. Deepa, and T. Narasinga Rao. *ACS Appl. Mater. Interfaces* (2013), **5**, 2555–2566.

[30] R. Prakash, R. J. Choudhary, D. M. Phase, and R. Kumar. *Magnetic Materials* (2008), **1003**, 25–27.

[31] M. Staniuk, O. Hirsch, N. Kränzlin, R. Böhlen, W. van Beek, P. M. Abdala, and D. Koziej. *Chem. Mater.* (2014), **26**, 2086 – 2094.

[32] J. D. Grunwaldt, M. Ramin, M. Rohr, A. Michailovski, G. R. Patzke, and A. Baiker. *Rev. Sci. Instrum.* (2005), **76**, 054104.

[33] P. M. Abdala, H. Mauroy, and W. van Beek. *J. Appl. Cryst.* (2014), **47**, 449–457.

[34] A. C. Larson and R. B. Von Dreele. *Los Alamos Natl. Lab. Report LAUR 86-748* (1994).

[35] B. H. Toby. *J. Appl. Crystallogr.* (2001), **34**, 210–213.

[36] R. A. Young. *The Rietveld Method*. Oxford University Press (1993).

[37] R. B. Von Dreele. *J. Appl. Crystallogr.* (1997), **30**, 517–525.

[38] B. Ravel and M. Newville. *J. Synchrotron Radiat.* (2005), **12**, 537–541.

[39] R. Tauler. *Chemom. Intell. Lab. Syst.* (1995), **30**, 133–146.

[40] J. Jaumot, R. Gargallo, A. de Juan, and R. Tauler. *Chemom. Intell. Lab. Syst.* (2005), **76**, 101–110.

[41] W. Windig and J. Guilment. *Anal. Chem.* (1991), **63**, 1425–1432.

[42] W. Windig, C. E. Heckler, F. A. Agblevor, and R. J. Evans. *Chemom. Intell. Lab. Syst.* (1992), **14**, 195–207.

[43] W. Windig and D. A. Stephenson. *Anal. Chem.* (1992), **64**, 2735–2742.

[44] P. Kuisma-Kursula. *X-Ray Spectrom.* (2000), **29**, 111–118.

[45] B. K. Teo. pages 91–94. Inorganic Chemistry Concepts. Springer Berlin Heidelberg, Berlin Heidelberg (1986).

[46] L. Mino, D. Gianolio, F. Bardelli, C. Prestipino, E. S. Kumar, F. Bellarmine, M. Ramanjaneyulu, C. Lamberti, and M. S. R. Rao. *J. Phys.: Condens. Matter* (2013), **25**, 385402.

[47] R. J. Woolley, B. N. Illy, M. P. Ryan, and S. J. Skinner. *J. Mater. Chem.* (2011), **21**, 18592–18596.

[48] M. Medarde, C. Dallera, M. Grioni, B. Delley, F. Vernay, J. Mesot, M. Sikora, J. A. Alonso, and M. J. Martínez-Lope. *Phys. Rev. B* (2009), **80**, 245105.

[49] A. Rougier, C. Delmas, and A. V. Chadwick. *Solid State Commun.* (1995), **94**, 123–127.

[50] A. J. Atkins, M. Bauer, and C. R. Jacob. *Phys. Chem. Chem. Phys.* (2013), **15**, 8095–8105.

[51] K.-W. Nam, W.-S. Yoon, and K.-B. Kim. *Electrochim. Acta* (2002), **47**, 3201–3209.

[52] B. Ravel. *J. Synchrotron Radiat.* (2001), **8**, 314–316.

[53] O. Niehaus, U. C. Rodewald, P. M. Abdala, R. S. Touzani, B. P. T. Fokwa, and O. Janka. *Inorg. Chem.* (2014), **53**, 2471–2480.

[54] R. Shannon. *Acta Crystallogr., Sect. A* (1976), **32**, 751–767.

[55] K. M. O. Jensen, M. Christensen, H. P. Gunnlaugsson, N. Lock, E. D. Bojesen, T. Proffen, and B. B. Iversen. *Chem. Mater.* (2013), **25**, 2282–2290.

[56] K. Jensen, M. Christensen, C. Tyrsted, and B. B. Iversen. *J. Appl. Crystallogr.* (2011), **44**, 287–294.

[57] D. Carriazo, M. D. Rossell, G. B. Zeng, I. Bilecka, R. Erni, and M. Niederberger. *Small* (2012), **8**, 2231–2238.

[58] L. C. Yang, Q. S. Gao, Y. H. Zhang, Y. Tang, and Y. P. Wu. *Electrochem. Commun.* (2008), **10**, 118–122.

[59] Y. Shi, B. Guo, S. A. Corr, Q. Shi, Y.-S. Hu, K. R. Heier, L. Chen, R. Seshadri, and G. D. Stucky. *Nano Lett.* (2009), **9**, 4215–4220.

[60] Z. Wang, J. S. Chen, T. Zhu, S. Madhavi, and X. W. Lou. *Chem. Commun.* (2010), **46**, 6906–6908.

[61] J. R. Dahn and W. R. McKinnon. *Solid State Ionics* (1987), **23**, 1–7.

[62] J. Jamnik and J. Maier. *Phys. Chem. Chem. Phys.* (2003), **5**, 5215–5220.

[63] Y. Liang, C. Tracy, E. Weisbrod, P. Fejes, and N. D. Theodore. *Appl. Phys. Lett.* (2006), **88**, 081901.

[64] P. A. Anderson. *Phys. Rev.* (1949), **75**, 1205–1207.

[65] J. H. Ku, Y. S. Jung, K. T. Lee, C. H. Kim, and S. M. Oh. *J. Electrochem. Soc.* (2009), **156**, A688–A693.

[66] O. V. Safonova, A. A. Guda, C. Paun, N. Smolentsev, P. M. Abdala, G. Smolentsev, M. Nachtegaal, J. Szlachetko, M. A. Soldatov, A. V. Soldatov, and J. A. van Bokhoven. *J. Phys. Chem. C* (2014), **118**, 1974–1982.

6.2 Puzzling Mechanism behind a Simple Synthesis of Cobalt and Cobalt Oxide Nanoparticles: In Situ Synchrotron X-ray Absorption and Diffraction Studies

The content of this chapter summarizes briefly the results on nucleation and growth of cobalt and cobalt oxide nanoparticles and was published in Chemistry of Materials, ***2014****, 26, pp 2086 - 2094, by Malwina Staniuk*, Ofer Hirsch*, Niklaus Kränzlin*, Rahel Böhlen, Wouter van Beek, Paula M. Abdala, and Dorota Koziej as a corresponding author. (* equal contribution)*

Here, we show a simple approach to synthesize cobalt and cobalt oxide nanoparticles in an organic solvent. We find that the cubic Co_3O_4 nanoparticles can be easily obtained, even at temperatures as low as 80 °C. Moreover, exactly the same reaction at 180 °C leads to metallic Co nanoparticles. Thus, in addition to the synthetic efforts, we study the mechanism of occurrence of oxidation and reduction of a Co^{2+} precursor in benzyl alcohol. Remarkably, the in situ X-ray absorption and diffraction measurements of the synthesis at 140 °C reveal that oxidation of Co^{2+} to $Co^{3+/2+}$ and reduction of Co^{2+} to Co^0 reactions take place simultaneously. It is followed by a rapid formation of Co_3O_4 nanoparticles and its consecutive solid-state reduction to CoO. In parallel, metallic Co nanoparticles begin to grow. In addition, Multicomponent Curve Resolution–Alternating Least Squares (MCR-ALS) analysis of X-ray absorption spectroscopy (XAS) data efficiently reveals the nontrivial interdependence between four different reactions. Our strategy to control reduction and oxidation of Co-based nanoparticles as they grow opens up an elegant pathway for the one-pot-synthesis of the hybrid materials for energy-related applications.

6.3 EXAFS Investigation of the Inversion in Zinc-Ferrite Nanoparticles

The content of this chapter briefly summarizes the formation mechanism of $ZnFe_2O_4$ nanoparticles and the manuscript is about to be submitted with Malwina Staniuk, Christoph Willa, Ofer Hirsch, Alla Sologubenko, Wouter van Beek, and Dorota Koziej as corresponding author

Here, we *in situ* investigate the synthesis mechanism and the kinetics of $ZnFe_2O_4$ formation in benzyl alcohol from zinc(II) acetate ($Zn(ac)_2$) and iron(III) acetylacetonate ($Fe(acac)_3$) and compare the results with the formation of ZnO and Fe_3O_4 from the same precursors. Even though the kinetic characteristics of the individual metal precursors are different, the mixed metal compound can be obtained in a one pot synthesis without any additional phases in the final product. To get a better understanding of the mechanism of $ZnFe_2O_4$ nanoparticles formation we follow the reaction by *in situ* powder X-ray Diffraction (PXRD) and X-ray absorption spectroscopy (XAS). We apply Multivariate Curve Resolution – Alternating Least Squares (MCR-ALS) method to the time resolved XAS data in order to recover spectra and concentration profiles of all species present during the synthesis. We perform complementary time-resolved ex situ analyses, such as Small Angle X-ray Scattering (SAXS), and High Resolution Transmission Electron Microscopy employed in a scanning mode (HR STEM). The HR STEM was accompanied by Energy Dispersive X-ray spectroscopy (EDX) studies of the particles to verify our results of the in situ studies. We observe formation of a zinc-rich intermediate phase, which forms as a result of higher reactivity of $Zn(ac)_2$ in benzyl alcohol in comparison with $Fe(acac)_3$. The flexible structure of nanoscale spinel ferrite, in regard to chemical composition, contains an excess of Zn^{2+} ions from the already reacted Zn(II) precursor, providing sufficient time for the Fe(III) precursor to react. Fast incorporation of nonstoichiometric amount of Zn results in zinc atoms occupying both tetrahedral and octahedral voids in the spinel structure. These findings contribute to building knowledge about the formation of multi-metal compounds in liquid media. The flexibility of nanoscale structures to be stable within a broad compositional range represents a unique advantage for the synthesis of complex nanoparticles in one pot.

List of Figures

List of Tables

List of Abbreviations

ATR-IR	Attenuated Total Reflection Infrared Spectroscopy
EDX	Energy Dispersive X-ray Spectroscopy
EXAFS	Extended X-ray Absorption Fine Structure
HERFD XAS	High-Energy Resolution Fluorescence detected XAS
HR-PXRD	High-Resolution PXRD
HR-TEM	High-Resolution Transmission Electron Microscopy
Ln	Lanthanide Elements
PXRD	Powder X-ray Diffraction
RE	Rare-Earth Elements
RIXS	Resonant Inelastic X-ray Scattering
SEM	Scanning Electron Microscopy
TFY	Total Fluorescence Yield
TGA	Thermogravimetric Analysis
vtc XES	Valence-to-Core XES
XES	X-ray Emission Spectroscopy
XANES	X-ray Absorption Near Edge Structure
XAS	X-ray Absorption Spectroscopy

Declaration

The research presented in this thesis is a result of collaborations with other Multifunctional Materials group members and scientiest from different institutes.

In chapter 2 the structure solution of monoclinic $La_2O_2CO_3$ was carried out by Dr. Li Luo, a former PhD student of the Multifunctional Materials group. Dr. Martin J. Süess, a former group member as well, performed the TEM measurements and evaluations. Dr. Kristina Kvashnina and Dr. Pieter Glatzel are scientists at the European Synchrotron Radiation Facility (ESRF) at ID26. They carried out the experiments, helped with the FEFF calculations, and participated in the scientific discussions.

Dr. Kristina Kvashnina acted as a beam line scientist in chapter 3 and introduced and helped me with the atomic multiplet calculations. Christoph Willa, a PhD student in the Multifunctional Materials group performed TGA measurements.

In chapter 4 Dr. Kristina Kvashnina was the beamline scientist and were involved in the analysis and interpretation of the data. Christoph Willa performed the refinement of the PXRD data.

Chapter 6 was a combiend work of several people. Dr. Guobo Zeng, a PostDoc and former PhD student of the Multifunctional Materials group, perfomed all the battery related experiments, such as assembly and capacity measurements, as well as the discussion on the results. Dr. Li Lu did the Rietveld refinement, Dr. Martin J. Süess the TEM analysis, and Felix Rechberger, another PhD student in the group, the SEM-EDX analysis. Dr. Malwina Staniuk, a former PhD student in our group, performed the MCR-ALS analysis of the nanoparticles formation data. Dr. Paula M. Abdala and Dr. Wouter van Beek are scientists at the Swiss-Norwegian beamline (SNBL) at the ESRF and were the beamline scientists for those experiments. Additionally, they helped with all questions to EXAFS.

Dr. Dorota Koziej is a group leader in the Multifunctional Materials group and supervisor of this thesis.

Professor Markus Niederberger is the head of the Multifunctional Materials group.

Acknowledgements

Many people contributed in one way or the other to this thesis and I would like to thank them. A special thanks goes to the following people:

Dr. Dorota Koziej. Thank you for giving me the opportunity to do my PhD in your group under your supervision. I appreciate your support and guidance throughout my time at the ETH. I enjoyed the scientific freedom that brought me deeper into the lanthanides and the possibilities to learn and apply different calculational methods. Lastly, the time you spent with the preperation of scientific reports was a great help and I learnt a lot.

Professor Markus Niederberger. Thank you, Markus, for letting me stay in your group as a PhD student. The diversity of topics and the great atmosphere within the group makes your group a very nice working place.

The members of the examining comitee, Prof. Jan-Dierk Grunwaldt, Prof. Marcin Sikora, and Prof. Manfred Fiebig for their interest in this work.

Kristina Kvashnina. I would like to thank Kristina for supervising me during six weeks at the ESRF in Grenoble. For all the help with FEFF and the atomic multiplets and for the support during the evaluation and calculations.

Gisela Angst. Gisi, vielen Dank für die vielen Gespräche in der Küche oder in deinem Büro. Du ermöglichst uns Doktoranden, uns mehr auf die Forschung als auf die Organisation derer zu konzentrieren. Andererseits natürlich vielen Dank für die grünen Ernährungstipps, die ich, ich gestehe, seltenst berücksichtigt habe. Für Reisetipps, die ich jetzt nach dem Doktorat beherzigen werde, und dafür, dass dein Name selten Programm ist, zumindest mir gegenüber.

The students Fabian Gygax and Yasemin Yurtsever. Thank you for your help in the lab and input for this thesis.

The beam-teams. Malwina without her help and expertise the *in-situ* experiments at SNBL would have been not successfull. Christoph Findler and Murielle Schreck for the help at SNBL. Christoph Willa, Niklaus Kränzlin, and Philipp Jäker for the help at ID26. The beamline scientists Wouter van Beek, Paula Abdala, and Pieter Glatzel.

Mulitfunctional Materials. I would like to thank all current and former group

members for the working atmosphere, the help, and scientific and non-scientific discussions. Felix, Mattia, and Nik deserve a special thanks. The coffee breaks in the morning and afternoon, and the time outside of the lab were always a nice change to science.

Meine Familie. Meine Eltern und meine Schwester mit ihrer Familie waren während diesen vier Jahren in Zürich aber auch schon im Studium eine konstante Unterstützung. Besonders die Aufforderung das Bekannte zu verlassen und etwas Neues zu probieren, halfen sehr.

Johanna Sadik. Danke für die Unterstützung während der Doktorarbeit. Du hast mich motiviert und mir auch in stressigen Zeiten geholfen, mich zu konzentrieren. Ich bin glücklich mit dir zu sein und freue mich auf die Zukunft.

C U R R I C U L U M V I T A E

Team oriented, analytical

Personal Information

Ofer Hirsch

Brunnwiesenstrasse 42, 8049 Zurich

ofer.hirsch@gmail.com

mobile: +41 78 623 53 65

office: +41 44 633 76 79

17.05.1987 in Frankfurt am Main

German citizenship, unmarried

Education

Since 1.11.2012	**PhD Candidate** Multifunctional Materials Departement of Materials Science ETH Zurich
	Scientific internship at ID26, ESRF (09 – 10/2013) Learned the FEFF9.0 code
10/2006 – 05/2012	**Study of Materials Science** Technische Universität Darmstadt
	Diplom examination (15.05.2012) Diplom-Ingenieur Overall assessment: good
	Thesis (11/2011 – 05/2012) Materials Modelling Screening of fields in ferroelectric perovskites Assessment: very good
	Preliminary Diploma (10/2008) Overall assessment: good
1997 – 2006	Lessing-Gymnasium, Frankfurt am Main Abitur, Final Grade: 1.7

Work Experience

Since 11/2012	**ETH Zurich, Multifunctional Materials** PhD Candidate Title: In-situ hard X-ray spectroscopy of rare-earth compounds Supervised one Master students project Teaching assistant for chemical lab for first year students
04/2010 – 07/2011	**Umicore AG & Co KG** World leader in exhaust catalyst **Student employee** Numerical Simulations of Exhaust Catalysts **Internship** University of Alberta in Edmonton, Canada Numerical Simulations of Exhaust Catalysts
05/2008 – 10/2011	**Technische Universität Darmstadt** Materials Science **Student assistant** Sonderforschungsbereich 595 Theoretical investigation of aging in Ferroelectrics **Student assistant** Nonmetallic-Inorganic Materials Synthesis, characterization, and data analysis on lead-free, ferroelectric ceramics

Computer Literacy

Programming	Matlab, Basics in Pyhton and Fortran
Office Programs	Origin MS Office LaTeX

Linguistic Proficiency

German	Mother tongue
English	Fluent

Talks and Poster Contributions at International Conferences

Talks	**VUVX2016, Zurich, Switzerland:** The reactivity of $La_2O_2CO_3$ towards CO_2 investigated with in situ HERFD XAS and valence-to-core XES **E-MRS Spring Meeting 2016, Lille, France:** In-situ HERFD XAS and vtc XES study on the reactivity of $Ln_2O_2CO_3$ towards CO_2 **XAFS16, Karlsruhe, Germany:** Atomic and electronic structure of $La_2O_2CO_3$ on the basis of X-ray absorption and emission spectroscopy and the reactivity of $La_2O_2CO_3$ films towards CO_2
Poster	**XAFS16, Karlsruhe, Germany:** The role of Ni in the MoO_2 lattice – The valence and neighborhood of the Ni dopant in monoclinic MoO_2 **MRS Spring Meeting 2014, San Francisco, USA:** In-situ X-ray absorption and emission spectroscopy study of the interaction between CO_2 and lanthanum-oxycarbonate nanoparticles

List of Scientific Publications

Submitted and prepared manuscripts:
O. Hirsch, K. O. Kvashnina, Christoph Willa, and D. Koziej
First direct evidence for hybridization of f-electrons
O. Hirsch, K. O. Kvashnina, Christoph Willa, and D. Koziej
HERFD–XANES spectroscopy as a probe of electron conductivity – a showcase for temperature-induced delocalization of f-electrons

O. Hirsch, K. O. Kvashnina, L. Luo, M. J. Süess, P. Glatzel, and D. Koziej
High-energy resolution X-ray absorption and emission spectroscopy reveals insight into unique selectivity of La-based nanoparticles for CO_2
Proceedings of the National Academy of Sciences, *112*, 15803 (2015)

O. Hirsch, G. Zeng, L. Luo, M. Staniuk, P. M. Abdala, W. van Beek, F. Rechberger, M. J. Süess, M. Niederberger, and D. Koziej
Aliovalent Ni in MoO_2 Lattice- Probing the Structure and Valence of Ni and Its Implication on the Electrochemical Performance
Chemistry of Materials, *26*, 4505 (2014)

Malwina Staniuk, Ofer Hirsch, Niklaus Kränzlin, Rahel Böhlen, Wouter van Beek, Paula M. Abdala, and Dorota Koziej
Puzzling Mechanism behind a Simple Synthesis of Cobalt and Cobalt Oxide Nanoparticles: In Situ Synchrotron X-ray Absorption and Diffraction Studies
Chemistry of Materials, *26*, 2086 (2014)

Malwina Staniuk, Daniel Zindel, Wouter van Beek, Ofer Hirsch, Niklaus Kränzlin, Markus Niederberger, and Dorota Koziej
Matching the organic and inorganic counterparts during nucleation and growth of copper-based nanoparticles - in situ spectroscopic studies
CrystEngComm, *17*, 6962 (2015)

Zurich, April 26, 2017